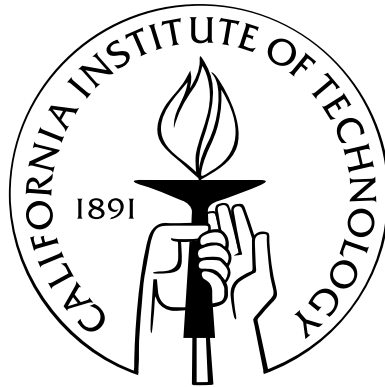


Structure and evolution of martensitic phase boundaries

Thesis by
Patrick Werner Dondl

In Partial Fulfillment of the Requirements
for the Degree of
Doctor of Philosophy



California Institute of Technology
Pasadena, California

2007
(Defended May 17, 2007)

For Dvina

Acknowledgements

I thank my advisor, Kaushik Bhattacharya, for his exceptionally great support and the trust that he has shown over the years. His insightful comments and the many enlightening discussions made working here a joyful and rewarding experience. I thank Chris Larsen, Johannes Zimmer, Peter Schröder, Michael Ortiz, Fehmi Cirak, Eitan Grinspun, Tom Hou, Houman Owhadi, Ching-Ping Shen, and many others for their help and Alex Kelly for reading the manuscript. I am very grateful to the friends I have found at Caltech—in the lab, at Caltech Rugby, and at many other places—I could not have done it without their support. None of this, of course, would have been possible without my parents, Barbara and Siegfried. Thank you!

Financial support was provided by the California Institute of Technology and the National Science Foundation (Grant Number DMS-0311788).

Abstract

This work examines two major aspects of martensitic phase boundaries. The first part studies numerically the deformation of thin films of shape memory alloys by using subdivision surfaces for discretization. These films have gained interest for their possible use as actuators in micro-scale electro-mechanical systems, specifically in a pyramid-shaped configuration. The study of such configurations requires adequate resolution of the regions of high strain gradient that emerge from the interplay of the multi-well strain energy and the penalization of the strain gradient through a surface energy term. This surface energy term also requires the spatial numerical discretization to be of higher regularity, i.e., it needs to be continuously differentiable. This excludes the use of a piecewise linear approximation. It is shown in this thesis that subdivision surfaces provide an attractive tool for the numerical examination of thin phase transforming structures. We also provide insight in the properties of such tent-like structures.

The second part of this thesis examines the question of how the rate-independent hysteresis that is observed in martensitic phase transformations can be reconciled with the linear kinetic relation linking the evolution of domains with the thermodynamic driving force on a microscopic scale. A sharp interface model for the evolution of martensitic phase boundaries, including full elasticity, is proposed. The existence of a solution for this coupled problem of a free discontinuity evolution to an elliptic equation is proved. Numerical studies using this model show the pinning of a phase boundary by precipitates of non-transforming material. This pinning is the first step in a stick-slip behavior and therefore a rate-independent hysteresis.

In an approximate model, the existence of a critical pinning force as well as the existence of solutions traveling with an average velocity are proved rigorously. For this shallow phase boundary approximation, the depinning behavior is studied numerically. We find a universal power-law linking the driving force to the average velocity of the interface. For a smooth local force due to an inhomogeneous but periodic environment we find a critical exponent of $1/2$.

Contents

Acknowledgements	iv
Abstract	v
List of Figures	viii
List of Tables	x
1 Introduction	1
1.1 The shape memory effect	1
1.2 Application of the shape memory effect for actuation	5
1.3 Hysteresis and pinning	6
2 Background	9
2.1 Models for shape memory alloys and martensitic phase transformations	9
2.2 Computational analysis of the martensitic phase transformation	11
2.3 Hysteresis, pinning, and depinning behavior	11
3 Modeling and numerical analysis of thin films of martensitic materials	13
3.1 Introduction	13
3.2 The model of thin films	15
3.3 Numerical method	19
3.4 Loop subdivision basis functions	21
3.5 Simulations	24
3.5.1 Regular tent	25
3.5.2 Convergence	28
3.5.3 Physical size of the domain	28
3.5.4 Crystallographic orientation	30
3.5.5 Rectangular domain	32
3.6 The regular tent revisited	32

3.7	Conclusions	36
4	A sharp interface model for the evolution of martensitic phase boundaries	37
4.1	Introduction to the model	37
4.2	Statement and analysis of the model	41
4.2.1	The model	41
4.2.2	Local estimates on the elastic energy	42
4.2.3	The implicit time discretization	45
4.2.4	Compactness of the time-discrete solution	46
4.2.5	Approximation of the original free discontinuity problem in the uniformly smooth case	52
4.3	Numerical estimate of the critical depinning force	54
4.4	Conclusions	56
5	Evolution in the shallow phase boundary approximation	57
5.1	Derivation of the approximate model	57
5.2	Stick-slip behavior	61
5.3	Numerical examination of the depinning transition	67
5.3.1	The numerical method	68
5.3.2	Simulations	68
5.4	Conclusions	72
6	Final remarks and future directions	73
A	Derivation of the thin film model	75
B	Notational conventions	77
B.1	Basics	77
B.2	Functional analysis	77
B.3	Elasticity	78
	Bibliography	79

List of Figures

1.1	Illustration of the shape memory effect	2
1.2	Change in lattice parameter in the martensitic phase transformation	2
1.3	Transformation from cubic to tetragonal crystal structure	3
1.4	Crystallographic background of the shape memory effect	4
1.5	Transformation of an indented tent shape to a flat configuration	5
1.6	Schematic of a micro-scale pump	6
1.7	Rate-independent hysteresis loops	7
1.8	Depinning behavior, as calculated from the one-dimensional model in [13]	7
3.1	Deformation of a reference configuration Ω at a certain time t	15
3.2	Contour plot of the energy landscape in the C_{11} - C_{22} plane	16
3.3	Mapping of unit triangle to deformed and undeformed configuration	19
3.4	Piecewise linear basis function and smooth spline basis function	22
3.5	A triangulation with the support of the basis functions	22
3.6	The base mesh with 4096 triangles	24
3.7	Time dependency of the energy in the system	25
3.8	Shape of the fully relaxed regular tent	26
3.9	Energy and strain variables of the regular tent	27
3.10	Cross section of tents formed with different numbers of elements in the base mesh	28
3.11	Influence of the physical size of the domain	29
3.12	Tents with rotated crystallographic axis	30
3.13	Detailed view of the 15 degree rotated tent	31
3.14	Tent shapes formed on a rectangular domain	33
4.1	Domain occupied by a phase transforming elastic body	41
4.2	Density estimate illustration 1	48
4.3	Density estimate illustration 2	49
4.4	Illustration of Lemma 4.2.7	50
4.5	Initial configuration of the transformation strain	54

4.6	Evolution of the average height of the interfaces for different external loads	55
4.7	The stuck phase boundary	55
5.1	Phase boundary on a strip domain	58
5.2	Experiment 1, the general depinning behavior	69
5.3	The local pinning forces used in Experiment 2	70
5.4	The depinning behavior for different sizes of pinning sites	71
5.5	Experiment 3, varying the stiffness of the interface	71

List of Tables

3.1	Comparison of base meshes of different resolution	29
3.2	Average energy density comparison for different domain sizes	29
3.3	Comparison of the energies of the tents with various amounts of rotation	31
5.1	Parameters used for the numerical examination of the depinning transition	67
5.2	Dependence of the critical applied force on the size of the pinning sites	68

Chapter 1

Introduction

1.1 The shape memory effect

The shape memory effect that occurs in some metallic alloys has been studied extensively by engineers, physicists, and mathematicians since its discovery in the 1960s. After undergoing an apparently plastic deformation at low temperature, these alloys return to their original shape when heated above a certain critical temperature, as illustrated in Figure 1.1. Thus, they seem to ‘remember’ their previous configuration. Another interesting phenomenon that occurs in such materials is superelasticity, where reversible deformations up to about six per cent can be achieved. Additionally, the stress there remains nearly constant over large portions of the deformation. The most commonly used shape memory alloy is Nitinol, which consists of an almost one-to-one atomic mixture of nickel and titanium. Other metallic alloys that exhibit the shape memory effect include copper-aluminum-nickel and copper-zinc-aluminum. Detailed descriptions of the phenomena and their applications may be found in [36, 60].

The peculiar behavior that these materials exhibit stems from an underlying phase transition—the martensitic phase transformation—in the metallic alloy. This phase transformation is characterized by a diffusionless transition from a solid high-temperature phase to a solid low-temperature phase. The high-temperature phase is called ‘austenite,’ the low-temperature phase is called ‘martensite.’

The change in lattice parameter when crossing the critical temperature is abrupt, however, the transition temperature from martensite to austenite is higher than the transition temperature from austenite to martensite. This phenomenon of hysteresis is depicted in Figure 1.2. Even though the difference in lattice parameters are quite high—approximately ten per cent in Nitinol—this first-order phase transformation is not diffusive, i.e., all atoms remain in the same position with respect to the lattice surrounding them.

There is a reduction in symmetry during the transformation and the crystallographic point group of the low-temperature phase is a strict subgroup of that of the high-temperature phase.

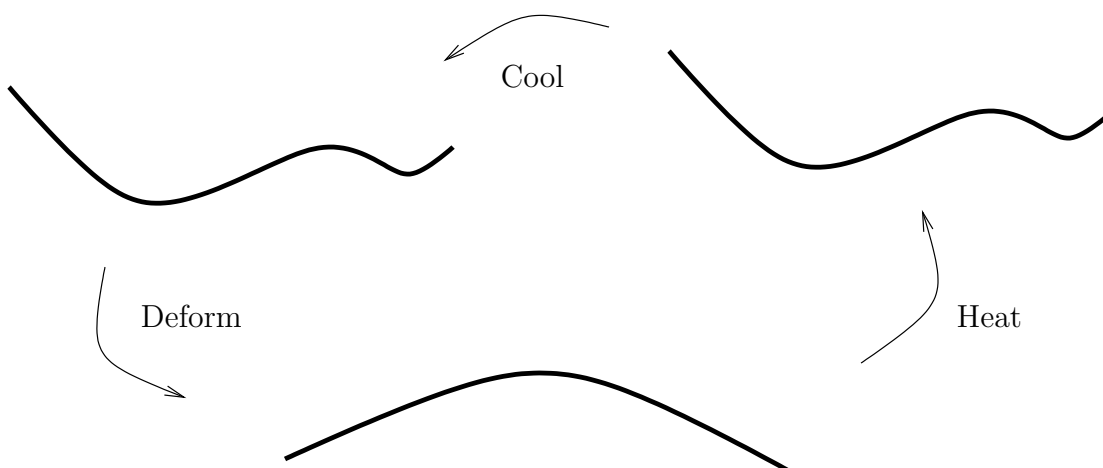


Figure 1.1: The shape memory effect. A piece of wire is deformed at low temperature and remains in that state until heating above a certain critical temperature when it returns to the original shape. Subsequent cooling does not alter the macroscopic shape further and the cycle can begin anew.

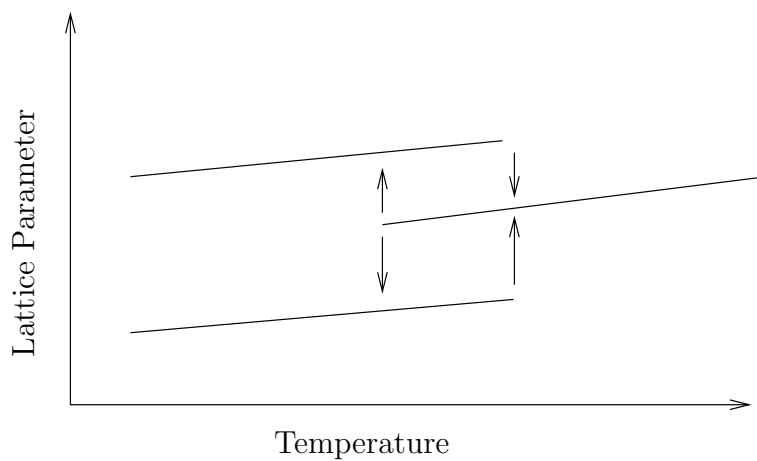


Figure 1.2: Change in lattice parameter in the martensitic phase transformation

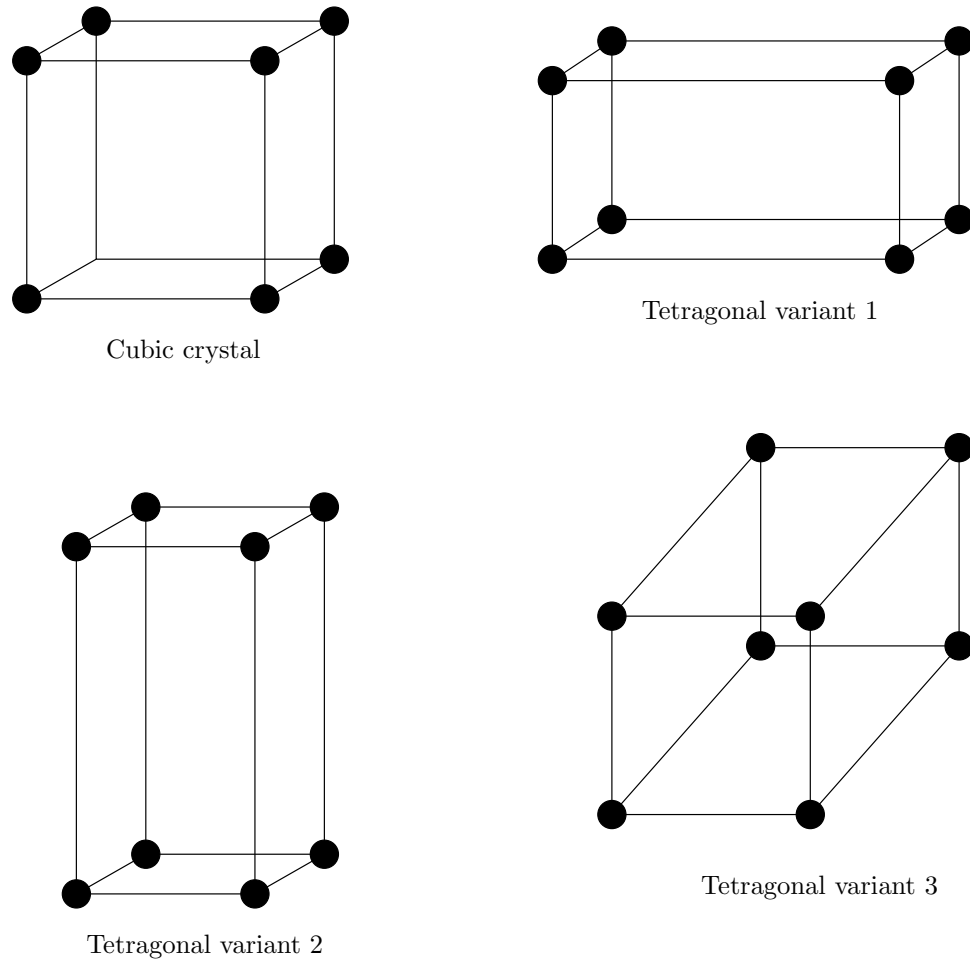


Figure 1.3: Transformation from cubic to tetragonal crystal structure. Since it is impossible to distinguish the cubic crystallographic axis, i.e., the crystal is invariant under the respective rotations that map one onto the other, the three shown tetragonal variants must be energetically equivalent.

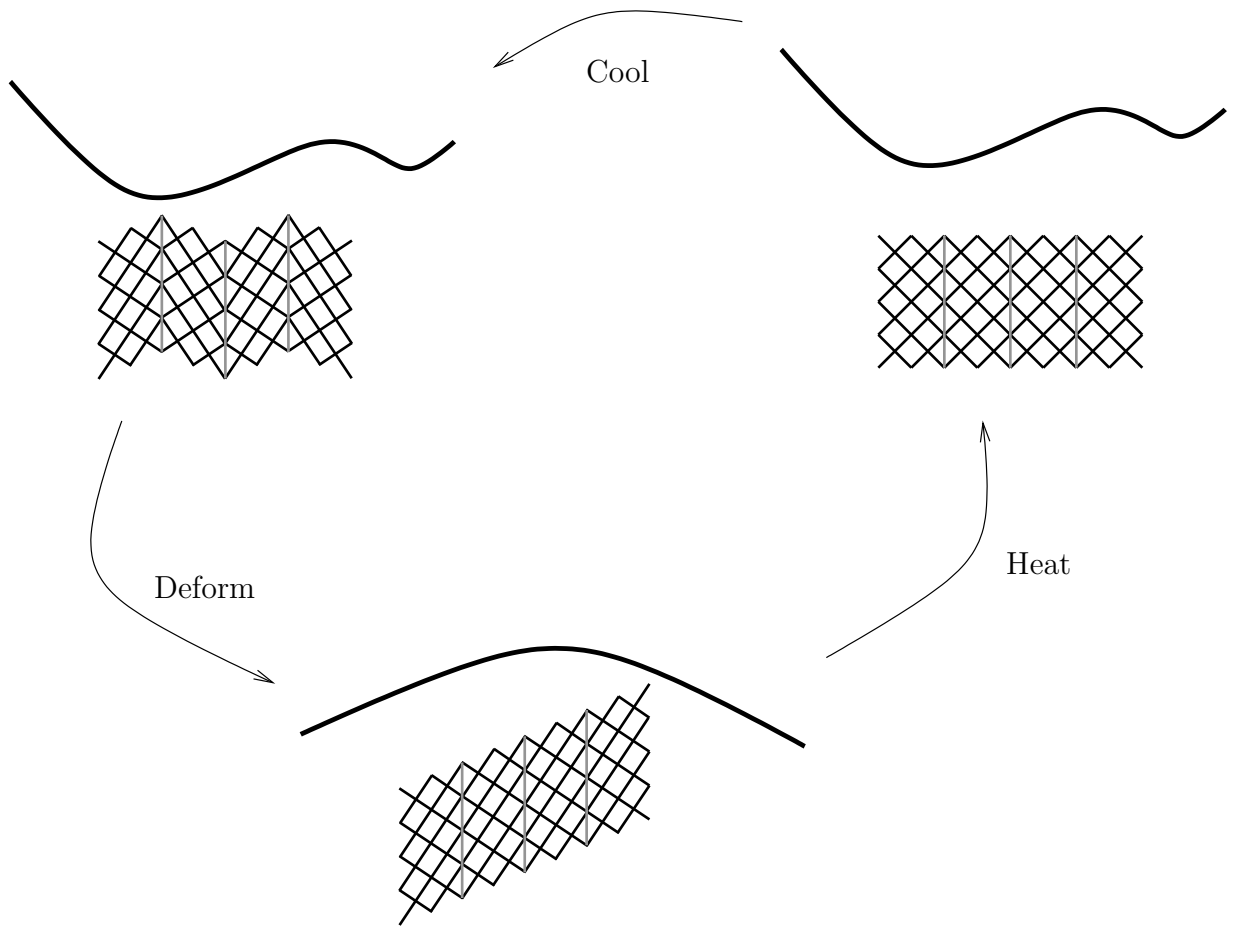


Figure 1.4: Crystallographic background of the shape memory effect. The stress-induced deformation effects a change in volume fraction of the martensite variants, so that heating reverses the macroscopic shape change. Subsequent cooling results again in a self-accomodating microstructure of martensite variants. (Crystallographic illustration courtesy of K. Bhattacharya [14], used with permission.)

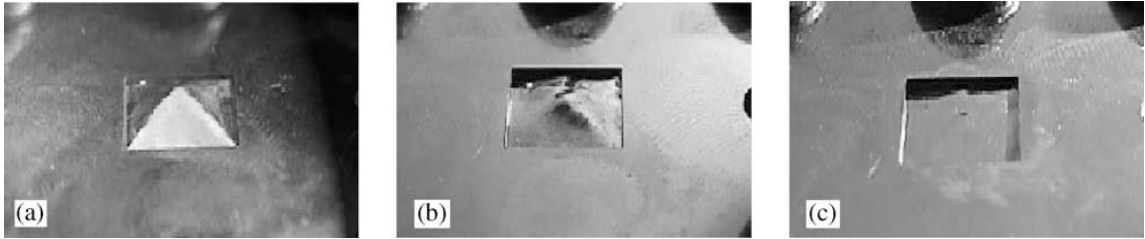


Figure 1.5: Transformation of an indented tent shape to a flat configuration. (a) 10°C , (b) 70° , (c) 90° . (Picture courtesy of J. Cui and R. D. James [26], used with permission.)

Assume, for simplicity, that the austenite is cubic and the low-temperature phase is of tetragonal symmetry, as depicted in Figure 1.3. The cubic crystal is invariant under rotations that map one crystallographic axis onto another. Since these rotations, if executed before the transition to the tetragonal symmetry takes place, lead to three differently aligned tetragonal variants of the crystal, these variants necessarily have to be energetically equivalent. For Nitinol, the high-temperature phase is cubic and the low-temperature phase is monoclinic, which leads to 12 variants.

The mechanism through which this phase transformation causes the macroscopic shape memory effect is illustrated in Figure 1.4, again with the cubic-tetragonal example. At first, consider the crystal at high temperature in the cubic phase in an undeformed reference configuration. Cooling the alloy below the critical temperature makes it energetically favorable to change the crystal symmetry to one of the martensite variants. It is by no means necessary that the whole crystal changes to one single variant. Quite the opposite is true. The crystal forms a microstructure (a fine-scale mixture) of layered martensite variants in order to retain its the macroscopic shape. This is called self-accomodation. Applying an external force on the crystal in this state does not effect a real plastic deformation. Instead the deformation can be accommodated by changing the volume fraction of the different variants by propagating the variant boundaries between them. This is energetically much easier than reversible elastic deformation (since no additional elastic energy needs to be stored—the different variants have the same energy) or plastic deformation. Now, however, if the material is heated, it returns to its original macroscopic shape, since the cubic crystal structure is uniformly restored, independent of the microstructure of martensite variants. Subsequent cooling leads again to the self-accomodating microstructure.

1.2 Application of the shape memory effect for actuation

A particularly intriguing way to exploit the shape memory effect is to use it for the purpose of mechanical actuation on a micro-scale. The direct coupling of macroscopic deformation and crystal structure leads to the fact that shape memory alloys exhibit by far the greatest work output of all systems that can be used as actuators on such a small size [50]. It is therefore an active area of

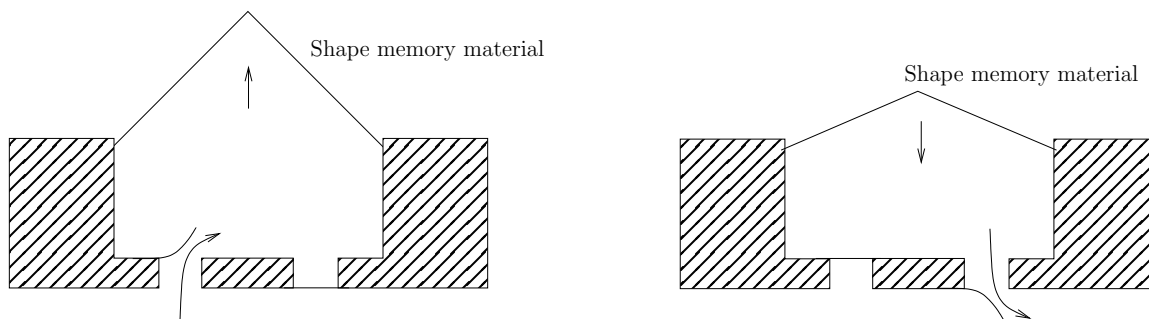


Figure 1.6: Example of a possible application of shape memory materials: Schematic of a micro-scale pump

research to replace the common electrostatic actuators on micro electro-mechanical systems (MEMS) with such phase transforming materials. MEMS integrate sensors, electronic circuits, and actuation on a single chip, usually silicon based.

One could imagine growing a shape memory material single crystal on top of a silicon substrate and subsequently etching away a square portion of the substrate underneath, leaving a free-standing film of martensitic alloy that is attached on all four sides. If the etching is properly lattice matched, the thin film of phase transforming material should transition between a stable tent-like shape and a flat configuration [15]. The transformation of a thin film of copper-aluminum-nickel from an indented tent shape to the flat configuration induced through heating has been achieved [26], as shown in Figure 1.5. Such a device could, for example, be used to build a micro-scale pump (see Figure 1.6) or valve.

Chapter 3 of this thesis examines numerically and analytically the possible phase boundaries that can lead to such tent shapes. Particular care has been taken to accurately resolve the sharp changes in gradients that occur in the Ginzburg-Landau model to describe the martensitic phase transformation. It was also necessary to use a discretization that makes no *a priori* assumptions on the resulting tent-shape, since the effects of non-exact lattice matching and different aspect ratios of the free-standing part of the film were examined.

1.3 Hysteresis and pinning

There is a significant hysteresis in the martensitic phase transformation (see, for example [62]). As already noted, the transformation temperature depends on the direction of the transformation. This is not the only occurrence of hysteresis. One also observes hysteresis in superelasticity: The transformation begins at higher stress than the reverse transformation. Figure 1.7 shows another instance from the work of Abeyaratne, Chu, and James [1]. They apply a biaxial dead load on a single crystal CuAlNi specimen at fixed temperature below the critical transformation temperature.

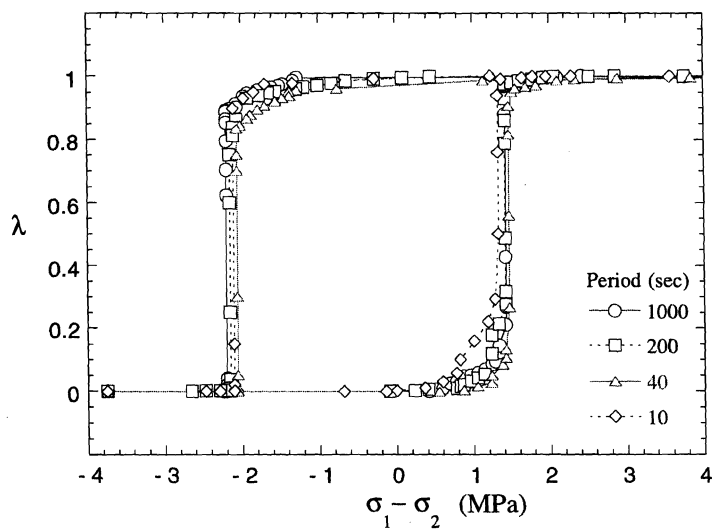


Figure 1.7: Rate-independent hysteresis loops in the plasticity-like regime of the shape memory effect. Shown is the volume fraction of one certain variant of martensite under time-dependent loading. Renormalizing time, the image shows clearly that the size of the hysteresis loop does not depend on the rate. (Image courtesy of Abeyaratne, Chu, and James [1], used with permission.)

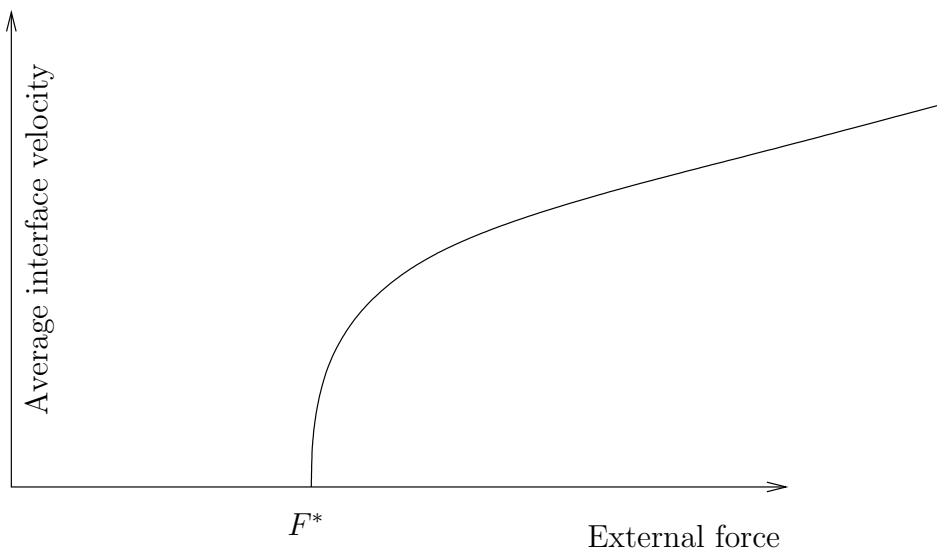


Figure 1.8: Depinning behavior as calculated from the one-dimensional model in [13]. The interface is stuck up to a critical force F^* , above which it breaks free and scales with a certain critical behavior. For large F , the average velocity is linear in the applied force.

The loading is performed in such a way that at any time at most two of the possible martensite variants were present in the specimen. The evolution of the microstructure formed by these two variants was carefully observed during the loading process. As displayed in Figure 1.7 from there, the shape memory alloy exhibits a clear stress versus volume fraction hysteresis loop.

Notice that this behavior is rate-independent, i.e., the area under the hysteresis loop does not depend on the rate of loading and does not vanish even if the experiment is performed very slowly. Specifically, the transformation begins only when the applied stress exceeds a critical value and goes to completion without requiring any increased stress. In other words, the rate of transformation is essentially independent of the applied stress as long as it is above a critical value. Commonly, hysteresis is included in the modeling assumptions for shape memory alloys [7, 59, 16, 21].

This observed behavior is different from the suggestion of microscopic theory. These theories yield that the rate of transformation is linear in the applied stress [63, 3]. But why is the phase boundary then stuck for small applied forces? A one-dimensional calculation, as found in [1, 13] illustrates how a local wiggly potential can pin a phase boundary and lead from a linear kinetic relation to a stick-slip behavior. Assume a bar with a 1-periodic local driving force $\varphi(x)$ (smooth and with non-degenerate global maximum and minimum), and assume that the velocity of the interface is given as $v = \varphi + F$, where F is the constant external applied force. The amount of time it takes for the interface to travel one period can now easily be calculated to be

$$T = \int_0^1 \frac{dg}{F + \varphi}, \quad (1.1)$$

if $F > -\min \varphi$ or $F < -\max \varphi$. Otherwise (i.e., if $-\min \varphi < F < -\max \varphi$), the time will be infinite. The average velocity $\bar{v} = \frac{1}{T}$ of the interface now exhibits a behavior of the form seen in Figure 1.8. In Chapters 4 and 5, this thesis examines how such behavior translates to models in higher space-dimensions, both in the fully nonlinear nonlocal case of elasticity and in an approximation for shallow phase boundaries.

Chapter 2

Background

2.1 Models for shape memory alloys and martensitic phase transformations

A survey of mathematical models for shape memory alloys can be found in [73] or [67], structured by the length scale that the model examines. Macro-scale thermodynamic models, in which the variables are the volume fraction of the martensite and austenite phases, include early one-dimensional approaches [6]. A recent multi-dimensional approach to thermodynamic modeling of the martensitic phase transformation, taking into account some of the features of the microstructure of martensite, can be found in [68]. These models are useful in predicting macroscopic properties of shape memory alloys in numerical simulations. However, detailed mathematical analysis in the sense of existence or uniqueness of solutions is largely unavailable for these models.

Models describing the microstructure in a probabilistic sense resolve the problem on an intermediate scale. The non-convex energies used to model phase transformations lead—without additional regularization—to non-attainment of solution in a classical or even the weak sense. Probability measures, especially Young measures as limits to minimizing sequences of solutions, are used, for example, in [44, 56] to relax the notion of a solution further and make the problem mathematically accessible. These (Gradient-)Young measures contain information about the probability of finding a certain deformation(-gradient) at each point. A recent proof of existence for Young measure valued solutions for a simplified thermo-elastic model for shape memory alloys in multiple space dimensions without any regularization can be found in [65].

Landau-Ginzburg models for phase transforming materials combine multi-well strain energies with a regularizing strain gradient term. Such a Landau-Ginzburg potential, depending on the first and second derivatives of the displacement u and of the temperature θ , can, for example, be of the form

$$\Phi(u_x, u_{xx}, \theta) = \Phi_0(\theta) + \alpha\theta\Phi_1(u_x) + \Phi_2(u_x) + \frac{\gamma}{2}u_{xx}^2. \quad (2.1)$$

defining the stress σ as

$$\sigma(u_x, \theta) = \frac{\partial \Phi(u_x, u_{xx}, \theta)}{\partial u_x}, \quad (2.2)$$

leading to an equation of motion of the form

$$\rho u_{tt} = (\sigma(u_x, \theta))_x - \gamma u_{xxxx} + f, \quad (2.3)$$

$$-\theta \Phi_0''(\theta) \theta_t = \kappa \theta_{xx} + \theta \sigma_\theta(u_x) u_{xt} + g, \quad (2.4)$$

with material constants κ , ρ , γ , and α . These models go back to the work of Falk [35] for shape memory alloys and are based on the ideas by Ginzburg and Landau to describe superconductivity. For a one-dimensional model of such kind, existence and uniqueness have been shown in [69].

The same kind of multi-well energy functionals can be used without the regularizing strain-gradient term (i.e., $\gamma = 0$), but with the introduction of a dissipation term instead. Using the material parameter β for the viscosity, such a system of equations can have the form

$$\rho u_{tt} = (\sigma(u_x, \theta) + \beta u_{xt})_x + f, \quad (2.5)$$

$$-\theta \Phi_0''(\theta) \theta_t = \kappa \theta_{xx} + \theta \sigma_\theta(u_x) u_{xt} + \beta u_{xt}^2 + g. \quad (2.6)$$

Existence and uniqueness for this system have been studied, for example, in [20, 27]. In [42], a system with surface energy and dissipation is studied.

The two- and three-dimensional generalization of Falk-type models is non-trivial. Even the construction of suitable multi-dimensional energy landscapes for the involved phase transformations is a matter of current research [30, 75, 72, 34] due to the complex symmetry constraints imposed by the point group of the high temperature phase. A two- or three-dimensional system without surface energy but with dissipation is examined in [74], where existence of a solution is shown. In [29], existence of a solution is shown for an isothermal system with surface energy using semi-group methods. An existence and uniqueness proof for a system with both dissipation and surface energy can be found in [61].

Sharp interface models comprise another approach to describing the martensitic phase transformation. Here, similar to the well-known Stefan problem of solidification, a free boundary describes the evolution of a phase boundary between martensite and austenite or between martensite variants. The monograph by Abeyaratne and Knowles [5] provides an overview of this aspect of the shape memory effect. The present thesis presents a proof of existence for such a free boundary problem in the presence of both a nonlocal stress field and a surface energy term.

2.2 Computational analysis of the martensitic phase transformation

One-dimensional numerical examinations of the systems of differential equations for Landau and Landau-Ginzburg models are presented, for example, in [19]. A simulation in the anti-plane shear setting (displacement $u: \Omega \subset \mathbb{R}^2 \rightarrow \mathbb{R}$) showing formation of microstructure can be found in [71]. There, a finite-difference scheme is used to compute the dynamics of a system with viscosity but without surface energy. A finite difference scheme with viscosity and surface energy is implemented in [64] for the multi-dimensional deformation setting ($u: \Omega \subset \mathbb{R}^n \rightarrow \mathbb{R}^n$). They use a polynomial three-well energy for a system in two space-dimensions. The time development of the formed microstructure is also evaluated. A computational approach using special gradient Young measure solutions is presented in [51], where a rate-independent law is used to model the evolution of microstructure in CuAlNi.

The most common approach for computations in elasticity is the use of finite elements [54]. In [46], this method is used to study a fully three-dimensional system with the Erickson-James energy density [31]. There, viscosity is used to dissipate energy from the system, but no surface energy is considered. This is changed in a later work [47]. In [45], the same approach is applied, but a temperature field is introduced and coupled to the system via a temperature-dependent elastic energy. A problem common to the described finite element simulations is that the regularity of the discretization is not sufficient to fully resolve the surface energy, i.e., the functions used to approximate the elastic displacement are not in the Sobolev space H^2 . This can lead to convergence problems. A simulation using conforming elements, which are finite elements that exhibit the regularity required by the partial differential equation, can be found, for example, in [29]. In Chapter 3 of this thesis, a different approach to finite elements is presented. Here, subdivision surfaces, which can be regarded as generalizations of splines, are used to achieve a conforming finite element discretization. This approach was introduced originally in [23] for the computational analysis of thin shells, where the bending energy term causes similarly elevated requirements on the smoothness of the discretization. The work there has been further extended to nonlinear elasticity [22].

2.3 Hysteresis, pinning, and depinning behavior

The pinning and depinning effects in the non-equilibrium dynamics of phase boundaries and related phenomena have been extensively studied by physicists. An overview in the context of charge-density-waves, interfaces and contact lines can be found in [43]. Generally, one uses an equation of the type

$$g_t(x) = \mathcal{K}g(x) + \varphi(x, g(x)) + F \tag{2.7}$$

to describe the phenomena. Here, \mathcal{K} is a possibly nonlocal operator that penalizes fluctuations in the height of the interface $g(x)$, the local fluctuations in the driving force are modeled by φ , and F is the external driving force. It is well known that the depinning behavior depends sensitively on the specific nature of both \mathcal{K} and φ . Often, renormalization group approaches are used to calculate the critical exponents of depinning [57, 58]; generally, however, they lack mathematical rigor.

For the example of a parabolic equation in a periodic environment,

$$g_t = \Delta g + \varphi + F, \tag{2.8}$$

where $\varphi(x, g)$ is 1-periodic in both variables and smooth, it can be shown [28] that the depinning transition exhibits a power-law behavior with a critical exponent of 1/2. The proof there assumes that there are only a finite number of possible pinned states in each period when the external force is exactly critical. This leads to the effect that for a small additional force the interface spends virtually all its time close to those critical states. Together with the smoothness of the local force this leads to the square root power-law behavior. For the one-dimensional model discussed in [13], the same power law arises through an integral expansion in the case of smooth forcing with distinct maxima and minima. The main difference in behavior from the models commonly analyzed in physics seems to be that their models have an infinite number of critical states at the depinning transition, and therefore lack the clear distinction between regions of high velocity and almost-stuck states that lead to the power law proved in [28].

In [24, 25], the effects of a pinning potential on the evolution of a phase boundary are considered with and without surface energy using homogenization techniques for Hamilton-Jacobi Equations. For both regimes an effective behavior can be derived, explicitly in the case of zero surface energy and for the limit of large surface energy.

The homogenization of a gradient flow of the volume fraction of a certain martensite variant in the presence of a wiggly energy is derived in [1]. The resulting stick-slip behavior is then compared to experiments on single crystals of CuAlNi.

In the present work first a sharp interface model for the evolution of a phase boundary in the presence of precipitates is developed in Chapter 4. The existence of a solution is proved. This model includes the full elastic nonlocal effects and is used to estimate the critical depinning force numerically. In Chapter 5, a linearization of the full model is used to study the depinning behavior both analytically and numerically.

Chapter 3

Modeling and numerical analysis of thin films of martensitic materials

This chapter studies numerically the deformation of thin films made of materials undergoing martensitic phase transformations by using subdivision surfaces. These thin films have received interest as potential microactuators, and specifically a tent-like configuration has recently been proposed. In order to model martensitic materials we use a multi-well strain energy combined with an interfacial energy penalizing strain gradients. The study of such configurations requires adequate resolution of inhomogeneous in-plane stretch, out-of-plane deformation, and transition regions across which the deformation gradient changes sharply. This chapter demonstrates that subdivision surfaces provide an attractive tool in the numerical study of such configurations, and also provides insights into the tent-like deformations.

The chapter is organized as follows. The introduction provides some background on the use of active materials as actuators in micro-scale systems, as well as the difficulties involved in numerically studying thin films of shape memory alloys. In Section 3.2, the continuum model and the relevant energy terms are introduced. The details of the finite element simulation are described in Section 3.3, followed by a short review in Section 3.4 of the subdivision surface method proposed in [23]. Section 3.5 contains the simulation results. Section 3.6 verifies our computational results with some analytical calculations. Some discussion of these results and an outlook to further improvements on this method are given in Section 3.7.

3.1 Introduction

Thin films of shape memory alloys have received attention as potential microactuators since the recognition that they possess the largest work per unit volume among possible actuator systems [50]. This is because the martensitic phase transformation, a solid-to-solid phase transformation responsible for the shape memory effect, provides a direct link between the macroscopic deformation and

microscopic changes in the crystalline unit cell. This advantage is maximized by using single-crystal thin films where the geometry of the structure is carefully chosen to be consistent with the inherent crystallography of the material. This, however, requires careful analysis of the deformation and this in turn requires a numerical method that is capable of resolving inhomogeneous in-plane stretch, out-of-plane deformation, and transition regions across which the deformation gradient changes sharply. Such an analysis is the goal of the paper.

The martensitic phase transformation is a diffusionless process where, at a certain temperature θ_c , the preferred crystallographic configuration of the material changes. Typically, the high-temperature phase, the austenite, has greater symmetry than the low-temperature phase, the martensite, and therefore the martensite has a number of symmetry-related variants. Consequently, the energy density of the material has a multi-well structure, with each well associated with a different phase/variant. The different phases may co-exist in a configuration, and one also has an interfacial energy which is often modeled as a quadratic penalization of the strain gradient, as mentioned in Section 2.1.

This raises the numerical difficulty, common to many other structural and materials problems, of accurately evaluating energies which depend on the first as well as second derivatives of the deformation. Numerical evaluation of such energies requires a discretization which is continuous in the deformation as well as in its first derivative. Consequently one can not use simple linear elements, and higher-order polynomials bring their own problems. Cirak and Ortiz [22] addressed this by adapting subdivision surfaces, which were introduced and widely used in computer graphics (see for example, [76]), as elements to study finite deformation of thin-shells. We further develop this approach, and demonstrate how subdivision surfaces can be used for the study of martensitic thin films. While the idea remains mostly the same, our approach differs in that the multi-well nature of the energy requires great care in order to resolve structures like the tip or the edges of the tent. Also, in our model, the bending energy term does not play a role, however, a somewhat similar interfacial energy term is introduced.

Our starting point is the theory of martensitic thin films proposed by Bhattacharya and James [15]. We use our computational method to explore in detail a tent-like deformation that has potential application as an actuator. The idea is to deposit a single crystal thin film of a martensitic material on a (silicon) substrate in such a manner that it is approximately lattice-matched to the austenite. Then, a small square region of the film is released by back-etching to give a free-standing membrane which is bonded on all sides. The free-standing region is in the austenite state when hot but transforms to the martensite on cooling. Further, if the crystallography of the material satisfies some special conditions, and if the orientation of the released region matches specific crystallographic directions of the material, then the films pop up like a tent in the martensitic state. Therefore we have a configuration that switches between a flat and a tent-like shape when subjected to temperature

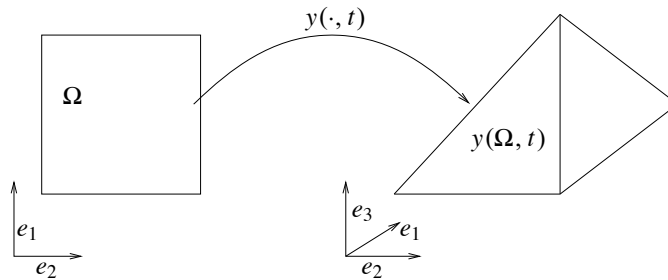


Figure 3.1: Deformation of a reference configuration Ω at a certain time t

cycling.

A detailed understanding of the exact nature of the deformation is the first motivation of our study. While the overall shape and structure conforms to the simplified analysis of Bhattacharya and James [15], we find an unexpected breaking of the symmetry at the tip. Studying the effects of misalignment is the second aim of our work, since it is difficult in practice to align the released region exactly with the crystallography of the material. We find that the overall structure remains stable for small deviations but it begins to deviate substantially beyond 10 degrees of misalignment. Finally, since the released area may not be a square, we study a rectangular region as an example.

Belik and Luskin [12] also studied tent-like deformation using a finite element method. However, their model of interfacial energy replaces higher-order derivatives with a term that lives on the element edges. Consequently, their energy depends critically on the triangulation and they arranged their triangulation in a way such that the expected phase/variant boundaries lie on such edges. Unfortunately such an approach requires an accurate *a priori* knowledge of the phase/variant boundaries and this is not possible in situations like those described above.

3.2 The model of thin films

Our model is an adaptation of a model of thin films proposed by Bhattacharya and James [15]. We provide further details of this model and our adaptation in Appendix A.

Consider a thin film occupying a flat reference configuration $\Omega \subset \mathbb{R}^2$ and undergoing a time-dependent deformation $y: \Omega \times \mathbb{R}^+ \rightarrow \mathbb{R}^3$ as depicted in Figure 3.1. We assume that $y(x, t)$ is injective and orientation preserving in the plane for all times. Furthermore, assume that $y(x, t)$ is sufficiently smooth to compute the deformation gradient $F(t) = \nabla y(t)$ and the second derivatives almost everywhere.

The dynamics of the film are governed by an energy consisting of the kinetic energy E_{kin} , a multi-well strain energy E_{strain} , and the interfacial or exchange energy $E_{\text{interfacial}}$, modeled using a higher (or strain) gradient. In non-dimensional quantities, these energies can be written as follows.

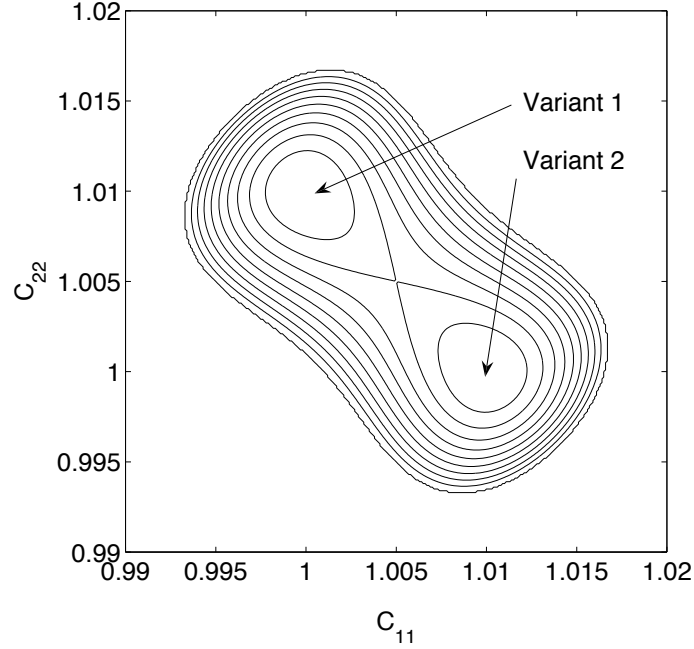


Figure 3.2: Contour plot of the energy landscape in the C_{11} - C_{22} plane. The parameters are the same as for the simulations, except for a , which is set to 0.01 to enable easy viewing.

Kinetic energy. The kinetic energy is given by

$$E_{\text{kin}} = \int_{\Omega} \frac{1}{2} |y_t|^2 dx. \quad (3.1)$$

Strain energy. The strain energy of the crystal is given as the integral of the strain energy density W ,

$$E_{\text{strain}} = \int_{\Omega} W(F(x)) dx. \quad (3.2)$$

To model the phase transition of the shape-memory material, one can use a strain energy density with multiple minima at the preferred positions in the strain space. Frame indifference requires the energy to be a function of the right Cauchy-Green strain tensor $C = F^T F$ alone. In our case, we consider a cubic-tetragonal phase transition and thus assume W to be of the form

$$\begin{aligned} W(F) = W(C_{ij}) &= a \cdot (C_{11} + C_{22} - 2 - \xi^2)^2 + \\ & b \cdot \Phi(C_{11} - C_{22}) \left((C_{11} - C_{22})^2 - \xi^4 \right)^2 + c \cdot C_{12}^2 \end{aligned} \quad (3.3)$$

with positive coefficients a , b , and c . This is a Landau-type energy density.

The function Φ augments the energy barrier in the nonconvex term of the strain energy and is given by

$$\Phi(q) = 1 + \eta \cdot e^{\frac{-q^2}{\kappa \xi^2}}, \quad (3.4)$$

with two parameters η and κ . The energy density has its minima on the set

$$O(2,3)U_1 \cup O(2,3)U_2 \quad (3.5)$$

where

$$U_1 = \begin{pmatrix} \sqrt{1+\xi^2} & 0 \\ 0 & 1 \end{pmatrix} \text{ and } U_2 = \begin{pmatrix} 1 & 0 \\ 0 & \sqrt{1+\xi^2} \end{pmatrix} \quad (3.6)$$

are the transformation stretches of the two variants of martensite, and $O(2,3) = \{A \in \text{Mat}(3,2) : A^T A = \text{Id}_{2 \times 2}\}$. Notice that one variant represents stretching in the x_1 -direction while the other represents stretching in the x_2 -direction. The contour plot of the energy is shown in Figure 3.2. For a detailed discussion on the problematic of constructing strain energy functions for martensitic phase transformations and the possible necessity of augmenting energy barriers of polynomial energies see [30].

For later use, we also consider the following. We will be interested in situations where the crystallographic axes do not coincide with the coordinate axes. In such situations, we will take the energy density to be of the form

$$W(R^T C(x) R) \quad (3.7)$$

where $R \in SO(2)$ is the rotation matrix that takes the crystallographic axes to the coordinate axes.

Interfacial Energy. The interfacial energy penalizes changes in the gradient and introduces an inherent length scale in the system. The interfacial energy used is given by

$$E_{\text{interfacial}} = \int_{\Omega} \frac{1}{2} |\Delta y|^2 \, dx. \quad (3.8)$$

Two comments are in order. First, this energy is apparently different from the commonly used form

$$\int_{\Omega} \frac{1}{2} |\nabla^2 y|^2 \, dx \quad (3.9)$$

where $\nabla^2 y$ denotes the third order tensor of second derivatives of y . However, these two terms differ only by a null-Lagrangian (i.e., terms which can be written exclusively in terms of boundary values). Therefore both energies yield the same governing equation. Further, since we use only the clamped boundary condition, the boundary term is in fact zero so that both forms agree. Second, observe that this energy also penalizes bending. In fact, $|\Delta y_3|^2 = |y_{3,11} + y_{3,22}|^2$ is the energy of bending for small deflections. However, in this paper, we shall think of this energy as arising due to interfacial energy.

Using these energies, we derive the non-dimensionalized dynamic equations using the principle

of stationary action:

$$\delta S = 0 \quad (3.10)$$

where S is the action integral given by

$$S = \int_{t_0}^{t_1} \mathcal{L} dt \quad (3.11)$$

with Lagrangian

$$\mathcal{L} = E_{\text{kin}} - E_{\text{strain}} - E_{\text{interfacial}}. \quad (3.12)$$

Substituting the expressions for the energy into the action integral yields

$$\begin{aligned} 0 &= \delta S \\ &= \delta \int_{t_0}^{t_1} \int_{\Omega} \frac{1}{2} |y_t(x, t)|^2 - W(F(x, t)) - \frac{1}{2} |\Delta y(x, t)|^2 dx dt \\ &= \int_{t_0}^{t_1} \int_{\Omega} y_{tt}(x, t) \cdot \delta y(x, t) - \frac{\partial W(x, t)}{\partial F} \cdot \nabla \delta y(x, t) dx dt \\ &\quad - \int_{t_0}^{t_1} \int_{\Omega} y_{tt}(x, t) \Delta y(x, t) \cdot \Delta \delta y(x, t) dx dt. \end{aligned} \quad (3.13)$$

Since none of the energy terms are explicitly time-dependent, and the variations of y can be chosen arbitrarily in time, equation (3.13) is equivalent to

$$0 = \int_{\Omega} y_{tt}(x, t) \cdot \delta y(x) - \sigma \cdot \nabla \delta y(x) - \Delta y(x, t) \cdot \Delta \delta y(x) dx \quad (3.14)$$

where

$$\sigma(x, t) = \frac{\partial W(x, t)}{\partial F} \quad (3.15)$$

is the Piola-Kirchhoff stress.

In this paper, we are interested in the equilibrium states. To obtain them from the dynamic equations above, we introduce dissipation in the system.

Dissipation. We introduce linear dissipation by augmenting (3.14) with the following term on the right-hand side:

$$- \int_{\Omega} \beta F_t \cdot \nabla \delta y(x) dx. \quad (3.16)$$

It is easy to show that

$$\frac{d}{dt} (E_{\text{kin}} + E_{\text{strain}} + E_{\text{interfacial}}) = \beta \int_{\Omega} |F_t|^2 dx. \quad (3.17)$$

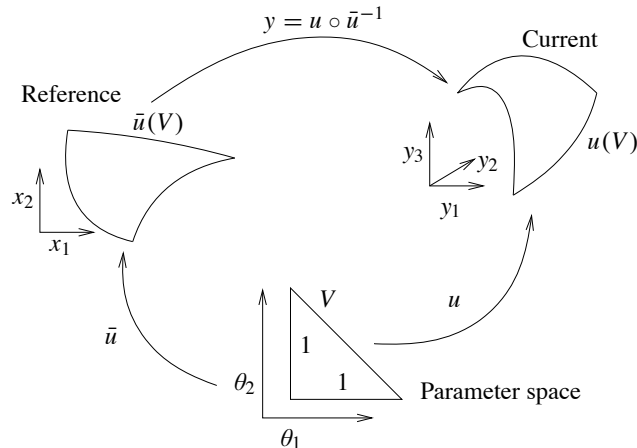


Figure 3.3: Mapping of unit triangle to deformed and undeformed configuration

The viscosity parameter β is of the order of 0.1, but it is increased when the simulation gets closer to the equilibrium configuration, in order to accelerate the loss of energy. Without this term, due to the fact that the governing equations as well as the numerical scheme are otherwise energy preserving, the system would oscillate indefinitely.

In summary, our model of thin films is given in weak form by

$$0 = \int_{\Omega} y_{tt}(x, t) \cdot \delta y(x) - \sigma \cdot \nabla \delta y(x) - \Delta y(x, t) \cdot \Delta \delta y(x) - \beta F_t \cdot \nabla \delta y(x) \, dx \quad (3.18)$$

for all $\delta y(x) : \Omega \rightarrow \mathbb{R}^3$ consistent with boundary conditions at each time t .

3.3 Numerical method

We seek to use the finite-element method to solve (3.18). This however requires care since this equation contains second derivatives of the displacement. In particular, our basis should have continuous first derivatives and we can not use the standard piecewise affine basis. We use subdivision surfaces following [22]. A discussion of the details is deferred till Section 3.4 after we describe the formulation.

We describe the reference and deformed configuration using a parametrization as shown in Figure 3.3. In other words, consider a smooth local one-to-one mapping from a set $V \subset \mathbb{R}^2$

$$\begin{aligned} \bar{u} : V &\rightarrow \Omega, \\ \bar{u} : \theta &\mapsto x = \bar{u}(\theta), \end{aligned} \quad (3.19)$$

which will later be induced by a triangulation of Ω , and a mapping

$$\begin{aligned} u: V \times \mathbb{R}^+ &\rightarrow \mathbb{R}^3, \\ u: (\theta, t) &\mapsto y = u(\theta, t), \end{aligned} \quad (3.20)$$

such that

$$y(x, t) = (u(\cdot, t) \circ \bar{u}^{-1}(\cdot))(x). \quad (3.21)$$

It follows that $F = \nabla y = \nabla u \cdot (\nabla \bar{u})^{-1}$. The second derivatives of y can be computed in a similar fashion by noting that

$$0 = \frac{\partial}{\partial x_i} \text{Id} = \frac{\partial}{\partial x_i} \nabla \bar{u} \nabla \bar{u}^{-1} = \nabla \bar{u}_{x_i} \nabla \bar{u}^{-1} + \nabla \bar{u} \nabla \bar{u}_{x_i}^{-1} \quad (3.22)$$

and using the chain rule. Further, the variation in y is related to the variation in u by

$$\delta y(x) = \delta u \circ \bar{u}^{-1}. \quad (3.23)$$

In the following we often continue to write Δy and $\Delta \delta y$ since the full expressions using u and \bar{u} are somewhat lengthy, but assume that they are written in terms of u and \bar{u} .

Now, assuming we have a non-overlapping set $\{V_q\}_{q=1}^m$ (where m will turn out to be the number of triangles in the base mesh) such that we have mappings u and \bar{u} as above on all V_q and

$$\bigcup_{q=1}^m \bar{u}(V_q) = \Omega, \quad (3.24)$$

equation (3.18) yields

$$\begin{aligned} 0 &= \sum_{q=1}^m \left[\int_{\bar{u}(V_q)} (u_{tt}(\cdot, t) \circ (\bar{u}(\cdot))^{-1})(x) \cdot (\delta u(\cdot) \circ (\bar{u}(\cdot))^{-1})(x) \, dx \right. \\ &\quad - \int_{\bar{u}(V_q)} \sigma(\nabla u \cdot (\nabla \bar{u})^{-1}) \cdot \nabla \delta u \cdot (\nabla \bar{u})^{-1} \, dx \\ &\quad - \int_{\bar{u}(V_q)} \Delta y \cdot \Delta \delta y \, dx \\ &\quad \left. - \int_{\bar{u}(V_q)} \beta \nabla u_t \cdot (\nabla \bar{u})^{-1} \cdot \nabla \delta u \cdot (\nabla \bar{u})^{-1} \, dx \right], \end{aligned} \quad (3.25)$$

where all the functions u and \bar{u} and their derivatives are evaluated at $\bar{u}^{-1}(x)$, as it is explicitly written in the first term. Now one can pull the integration back onto the parameter space so that

one has

$$\begin{aligned}
0 = \sum_{q=1}^m \left[\int_{V_q} u_{tt} \cdot \delta u |\nabla \bar{u}| d\theta \right. \\
- \int_{V_q} \sigma(\nabla u \cdot (\nabla \bar{u})^{-1}) \cdot \nabla \delta u \cdot (\nabla \bar{u})^{-1} |\nabla \bar{u}| d\theta \\
- \int_{V_q} \Delta y \cdot \Delta \delta y |\nabla \bar{u}| d\theta \\
\left. - \int_{V_q} \beta \nabla u_t \cdot (\nabla \bar{u})^{-1} \cdot \nabla \delta u \cdot (\nabla \bar{u})^{-1} |\nabla \bar{u}| d\theta \right]. \quad (3.26)
\end{aligned}$$

We discretize u, \bar{u} using the Loop subdivision surface basis functions $\{\varphi_i\}_{i=1}^n$ (in our case, since the basis functions are centered on triangle vertices, n is the number of vertices in the base mesh) so that,

$$\bar{u}(\theta) = \sum_{i=1}^n \bar{u}_i \varphi_i(\theta) \quad (3.27)$$

and

$$u(\theta, t) = \sum_{i=1}^n u_i(t) \varphi_i(\theta) \quad (3.28)$$

with coefficients u_i, \bar{u}_i . With this discretization, we follow the usual finite element approach and enforce equation (3.26) for the test function δu in the span of $\{\varphi_j\}_{j=1}^n$. In our formulation, we treat the \bar{u}_i associated with the reference configuration as fixed coefficients and the u_i associated with the deformed configurations as variables which we solve for. This yields an equation of the form

$$M\ddot{\mathbf{u}} = \mathbf{f}(\mathbf{u}, \dot{\mathbf{u}}) \quad (3.29)$$

with the mass matrix $M_{ij} = \sum_{q=1}^m \int_{V_q} \varphi_i \varphi_j |\nabla \bar{u}| d\theta$. We compute all integrals using a simple one-point approximation. We then lump the mass matrix in a row-sum manner and advance the remaining second-order ordinary differential equation in time using a second-order accurate explicit Newmark scheme.

3.4 Loop subdivision basis functions

In order to provide a meaningful discretization of the continuous model in equation (3.18), we have already noted that the approximating functions need to be in H^2 . A continuously differentiable discretization will provide such a setting.

We begin in one space dimension. Consider the discretization¹ shown in Figure 3.4. A simple linear finite element basis function associated with node 0 is shown as a dashed line. It is continuous

¹The discretization is shown to be regular, but that is not necessary.

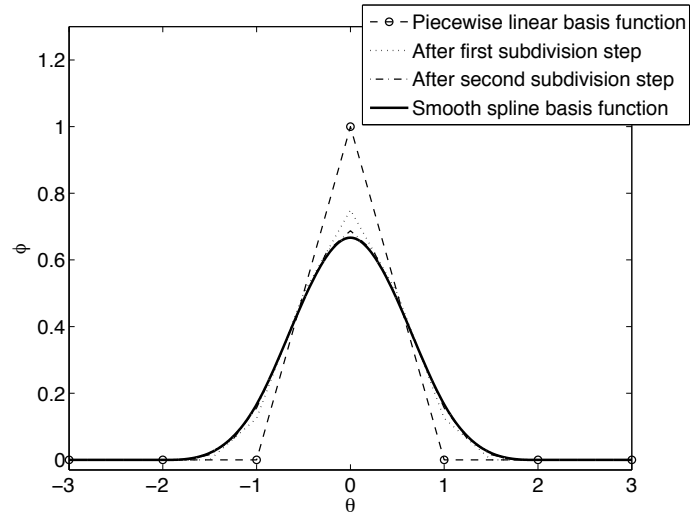


Figure 3.4: The piecewise linear basis function and the smooth spline basis function that it is replaced with. Also shown are the first two steps of subdivision. Note that they are still polygonal lines, but converge to the smooth spline. The nodes are on every integer parameter value.

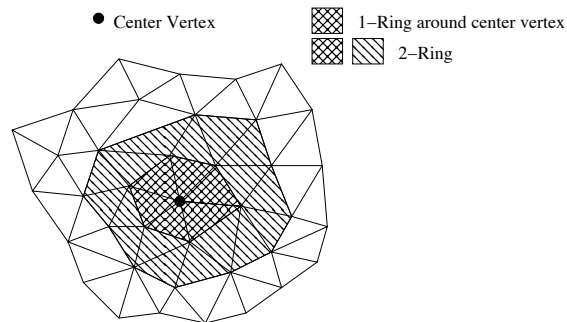


Figure 3.5: A triangulation with the support of the basis functions

but not continuously differentiable. Therefore, we would like to replace it with a C^1 (or smoother) basis function, as shown by the solid line, while retaining two properties: first, it has to have finite support, and second, it has to have one degree of freedom centered at the node. A cubic B-spline has exactly these properties, and the support is confined to four adjoining ‘elements’ centered around the middle node. In other words, we replace the dashed polygonal curve with the solid approximating spline curve using the same nodes.

To be precise, consider the two-dimensional polygonal curve connecting the n points $x_i^0 = (\theta^i, \phi^i)$. We can generate an approximating spline as follows (see for example, [76]). Generate a new set of $2n - 1$ points by subdivision:

$$x_{2i}^1 = \frac{1}{2}(x_i^0 + x_{i+1}^0) \quad (3.30)$$

and

$$x_{2i-1}^1 = \frac{1}{8}(x_{i-1}^0 + 6x_i^0 + x_{i+1}^0) \quad (3.31)$$

and connect them with a polygonal curve. The process is illustrated in Figure 3.4. Repeating this process leads, in the limit, to a C^2 cubic spline curve. The linearity of the process ensures that the limiting curve can be written as a linear combination of basis functions with the original vertex positions as weights. Starting with the polygonal curve generated by the linear basis functions gives us a new basis function with the properties described above. This algorithm has to be modified for boundary nodes, but this is easily accomplished in one dimension.

We now extend this idea to two space dimensions. We start with a given triangulation, as shown in Figure 3.5. As in one dimension, we seek to replace the piecewise linear basis functions with a C^1 basis function that is compactly supported and has one degree of freedom. The Loop subdivision basis functions [52] do so by replacing the polyhedral surface generated by the linear basis function with a C^1 surface. The basic idea is the quadrisection of triangles with a particular choice of weights for the new nodes. We refer the reader to Zorin and Schröder [76] for details. In our finite element context, the support of the chosen subdivision basis functions is the 2-ring of triangles around a given vertex, as shown in Figure 3.5. The particular basis functions depend on the topology (connectivity) of the triangulation.

Care has to be taken in fixing the boundary conditions, because of the extended support of the basis functions. One can either change the subdivision rules near the boundary to prescribe position and normal vectors to the surface at the boundary [17], or add a layer of ‘ghost’ vertices around the domain as suggested in [23], which is the approach chosen here.

Our simulation uses the routine described in [70] to efficiently evaluate the basis functions for a given triangle patch.

In order to achieve the setting in Section 3.3, we start with a triangulation of the computational domain. The mapping \bar{u} uses the vertex positions of that triangulation as coefficients. The deformed

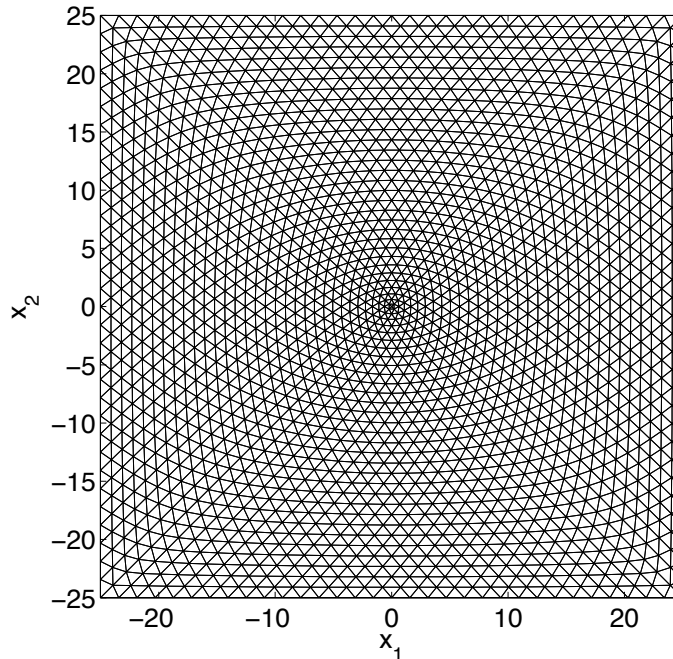


Figure 3.6: The base mesh with 4096 triangles

configuration then has variable coefficients in \mathbb{R}^3 , which comprise the degrees of freedom in our computation.

3.5 Simulations

In this section we present the results of various numerical experiments motivated by the tent-like deformations described in the introduction. All simulations use the energy parameters

$$a = 5.0, \quad b = 5.0, \quad c = 5.0, \quad \xi = 0.1, \quad \eta = 3.0, \quad \kappa = 1.0 \quad (3.32)$$

unless otherwise noted. The triangular base mesh used in the simulations is shown in Figure 3.6. It was created by repeated subdivision according to the Loop subdivision scheme of a mesh consisting of the four triangles formed by cutting the square along the diagonals. In figures displaying the surfaces, the color indicates which energy well can be attributed to the respective position. All simulations use clamped boundary conditions, i.e.:

$$y = \begin{pmatrix} x_1 \\ x_2 \\ 0 \end{pmatrix}, \quad (\nabla y)n = \begin{pmatrix} n_1 \\ n_2 \\ 0 \end{pmatrix} \quad \text{on } \partial\Omega. \quad (3.33)$$

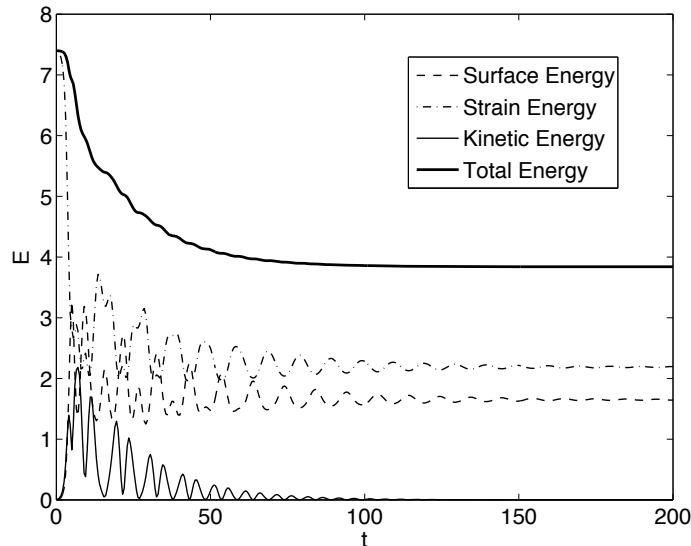


Figure 3.7: Time dependency of the energy in the system

We start the simulations with an initial condition corresponding to a flat surface subjected to a small push in the vertical dimension, and wait till it bounces around and evolves into a tent-shaped structure. A typical plot of how the various energies involved behave over time is shown in Figure 3.7.

3.5.1 Regular tent

Figures 3.8 and 3.9 show the shape and the details of the fully relaxed tent formed on a domain of size 50×50 domain non-dimensionalized units calculated using 16384 elements. Figure 3.8 shows a nice pyramidal shape with almost flat surfaces and rounded edges. Regions with deformation gradient close to the first well are colored blue, those close to the second are colored orange and the rest grey. The different variants are also labeled in Figure 3.8. Clearly the flat faces correspond to almost constant deformation gradient close to the wells. This is confirmed in Figure 3.9(a) which shows that the strain energy is concentrated at the boundary, ridges, and tip. This is also consistent with the fact that $C_{11} + C_{22}$, $C_{11} - C_{22}$, and C_{12} stay close to the values at the bottoms of the energy well except in these regions.

It is clear from Figures 3.9(b)–3.9(d) that the deformation is quite complex, involving the various components of the Cauchy-Green tensor. In particular, the deformation can *not* be described as a simple out-of-plan deformation (anti-plane shear) since this would force the Cauchy-Green tensor to be of the form

$$C = \begin{pmatrix} 1 + \alpha^2 & \alpha\beta \\ \alpha\beta & 1 + \beta^2 \end{pmatrix}. \quad (3.34)$$

It is also evident from Figures 3.9(b)–3.9(d) that the $C_{11} - C_{22}$ component of the Cauchy-Green

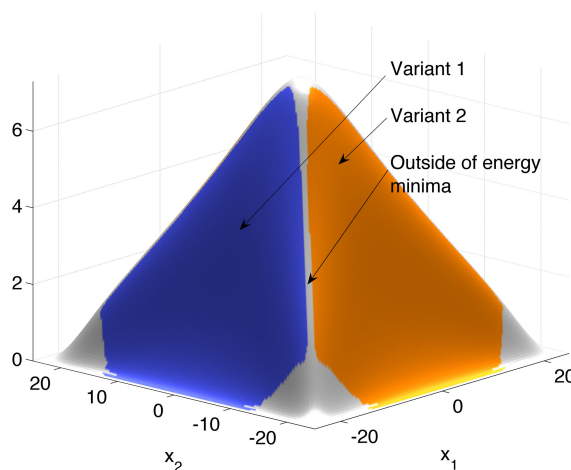


Figure 3.8: Shape of the fully relaxed regular tent. The numbering of the variants corresponds to Figure 3.2.

tensor transitions from ξ^2 to $-\xi^2$ across the ridges whereas the $C_{11} + C_{22}$ and C_{12} components remain essentially uniform. In other words, the Cauchy-Green tensor effectively traverses the energy surface along the straight line as it transitions from one well to another along a ridge. This is not surprising given that the energy grows quickly (quadratically) in the convex directions, $C_{11} + C_{22}$ and C_{12} . We shall elaborate on this with some analytic considerations in Section 3.6.

Figure 3.9(b) also reveals that the computed tent is not exactly symmetric despite the fact the energy and geometry are. Instead, the tip where the four ridges meet appears to split into two creating a narrow strip of one contiguous variant. This asymmetry was observed in a simulation with a carefully constructed symmetric mesh and a symmetric initial condition. We also find that the mirror image of the solution shown in Figure 3.9(b) is equally stable. The tip of this steady state solution shows features similar to the tents with a slightly rotated strain energy density like in Section 3.5.4. However, a symmetric initial condition generated by symmetrizing this solution—in order to create a symmetric initial condition with very low energy—leads to a relaxed state that is symmetric. This symmetric state has slightly lower total energy than the asymmetrical one (11.01488 non-dimensionalized units, versus 11.01512 for the asymmetrical tent).

We consider this breaking of symmetry real and not an artifact of numerical discretization, and believe that it constitutes a local minimum of the energy that has a significant domain of attraction.

Finally, observe from Figure 3.9(a) that the energy density is highest near the boundary, especially at the corners, and significantly higher than that at the ridges and the tip. Our clamped boundary conditions force the deformation gradient to be identity and thus $C_{11} + C_{22}$ to take the value 2 at the corners (as also seen in Figure 3.9(c)). This value is different from the value $C_{11} + C_{22} = 2 + \xi^2$ at the bottom of the wells and the energy grows quadratically in this direction.

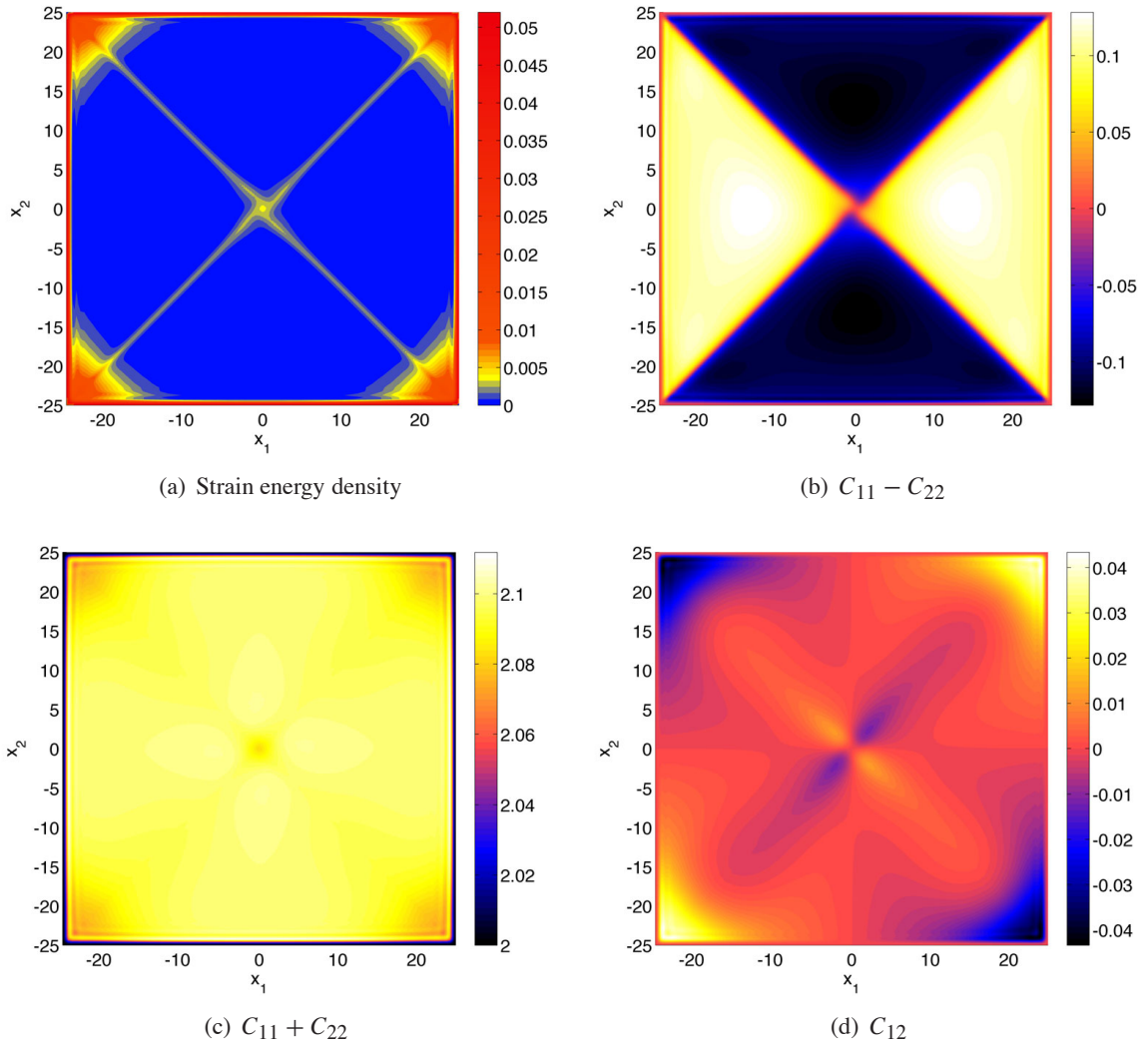


Figure 3.9: Energy and strain variables of the regular tent

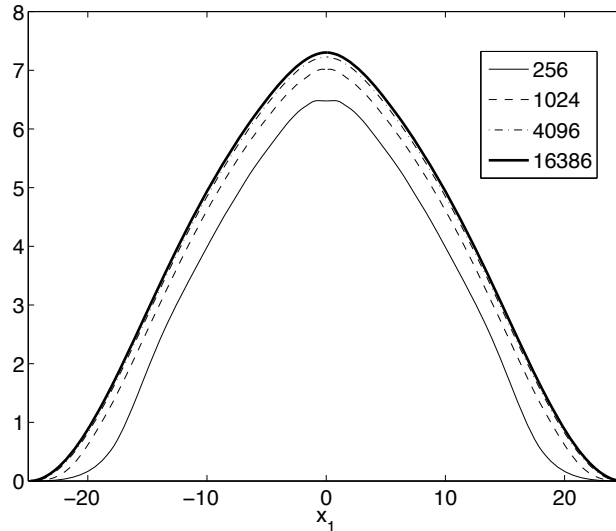


Figure 3.10: Cross section at $x_2 = 0$ of tents formed with different numbers of elements in the base mesh

3.5.2 Convergence

A comparison of the tents formed in a region of size 50×50 (non-dimensionalized units) with four different base meshes consisting of 256, 1025, 4096, and 16384 triangles is shown in Figure 3.10. Various quantitative details including L^2 norm of the height and energies are given in Table 3.1. We conclude that the 4096 element mesh provides a sufficient resolution for the following simulations and requires only a moderate amount of time to fully relax.

3.5.3 Physical size of the domain

Figures 3.11(a)–3.11(c) show the shapes of fully relaxed tents formed on domains with size 12×12 , 25×25 and 50×50 non-dimensionalized units. The same number of elements (4096) were used in each computation. Figure 3.11(d) shows the cross sections of the various surfaces at $y = 0$ for direct comparison.

When the domain size is extremely small, the interfacial energy dominates and the tent is very rounded (Figure 3.11(a)). Further, no area can be clearly identified as belonging to any variant. However, as the domain size increases, the tent becomes more pyramidal as the sides become flatter with the deformation gradient taking values in the energy wells. The size of the boundary layer in between areas of constant strain does not vary significantly with the domain size; instead the areas of constant strain close to one of the two minima in strain space become larger. Table 3.2 shows the declining average energy densities for different domain sizes.

Table 3.1: Comparison of base meshes of different resolution

Number of elements	256	1024	4096	16384
Absolute L^2 norm of surface height	30.0	35.1	37.3	38.1
L^2 norm of difference to next higher resolution	3.6	2.7	0.7	
Interfacial energy	3.8	4.7	5.2	5.6
Strain energy	28.4	15.1	8.6	5.4

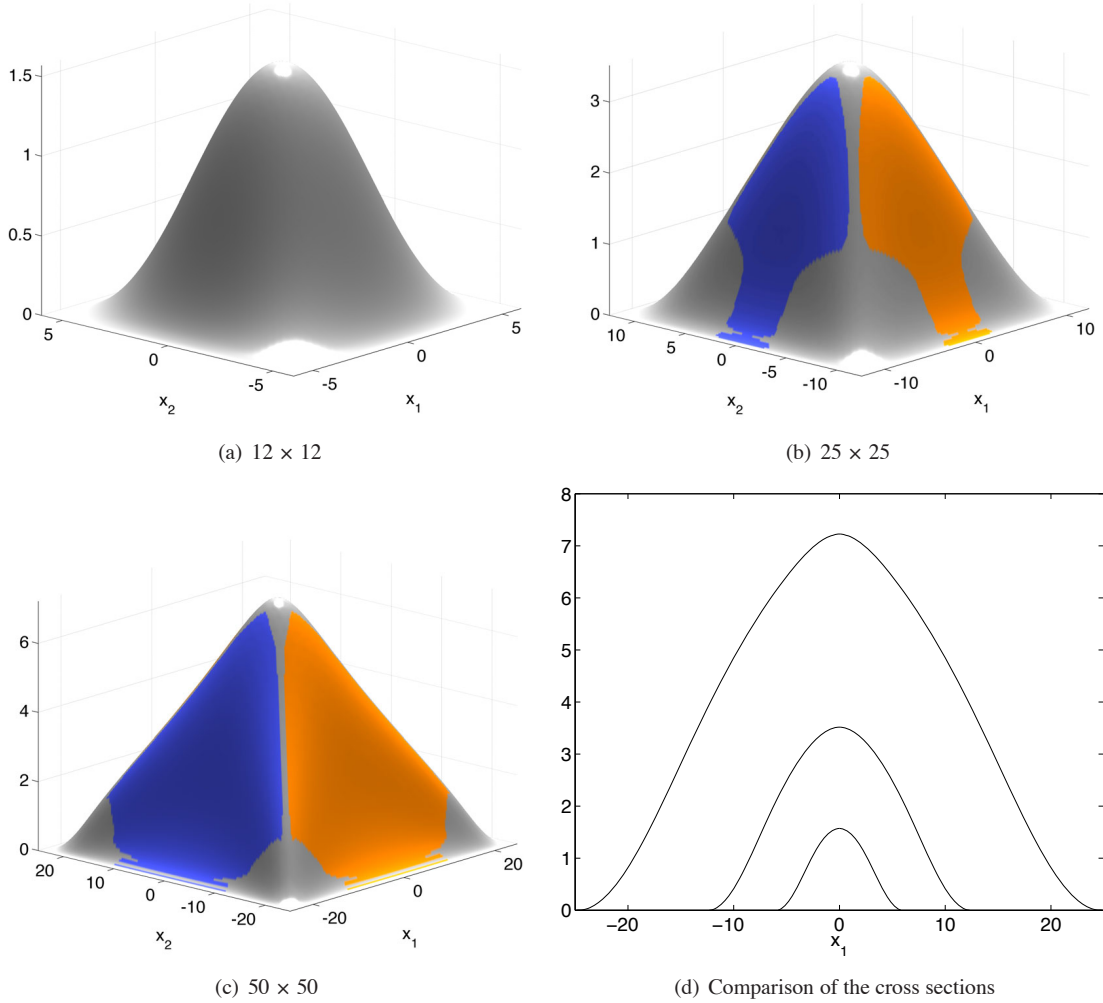


Figure 3.11: Influence of the physical size of the domain. (Color coding as in Figure 3.8)

Table 3.2: Average energy density comparison for different domain sizes

Domain size	12×12	25×25	50×50
Interfacial energy per domain area	$1.4 \cdot 10^{-2}$	$5.1 \cdot 10^{-3}$	$2.1 \cdot 10^{-3}$
Strain energy per domain area	$9.0 \cdot 10^{-3}$	$3.5 \cdot 10^{-3}$	$3.4 \cdot 10^{-3}$

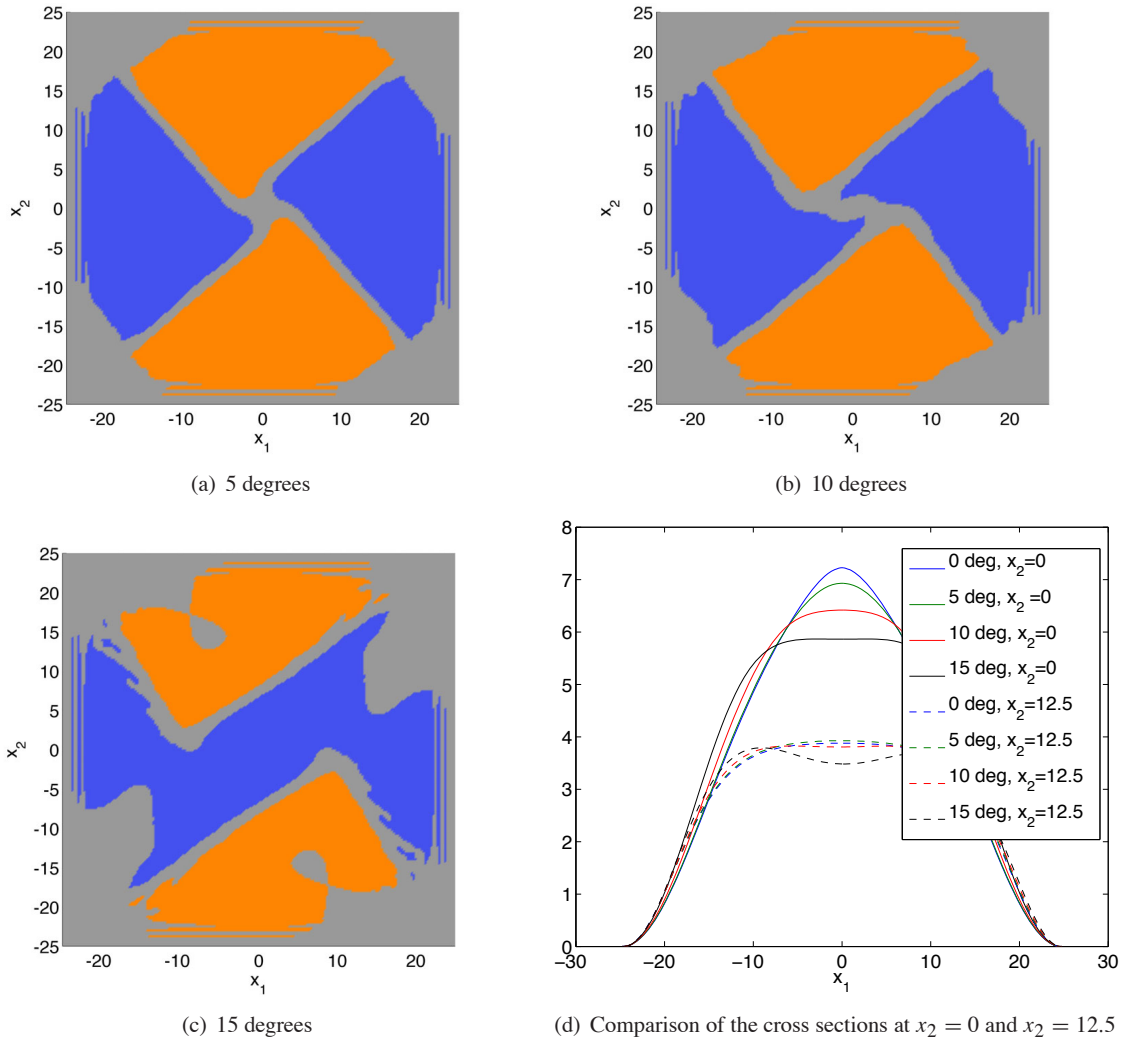


Figure 3.12: Shapes formed using a crystallographic axis which is rotated with respect to the physical domain. Shown are top views; colors indicate variants as in Figure 3.8.

3.5.4 Crystallographic orientation

The strain energy density (3.3), and in particular the position of the energy wells, embed information about the crystallography. In the examples above, the crystallography and the physical geometry of the domain were aligned in such a manner so as to form a nice tent. Specifically the domain was a square and the preferred interface (ridge) directions coincided with the diagonals of the domain. In practice, it may prove difficult to provide such an alignment and this section examines the consequences of any misalignment. We keep the orientation of the domain unchanged, but use the rotated energy density (3.7). The initial conditions and boundary conditions are as before; the domain size is 50×50 non-dimensionalized units discretized using 4096 elements.

Figure 3.12 shows the equilibrated tents for misalignments of 5° , 10° , and 15° . Figure 3.12(d)

Table 3.3: Comparison of the energies of the tents with various amounts of rotation of the crystallographic axes with respect to the domain

Rotation	0 degrees	5 degrees	10 degrees	15 degrees
Interfacial energy	5.2	5.2	5.4	5.8
Strain energy	8.6	8.7	8.9	9.3

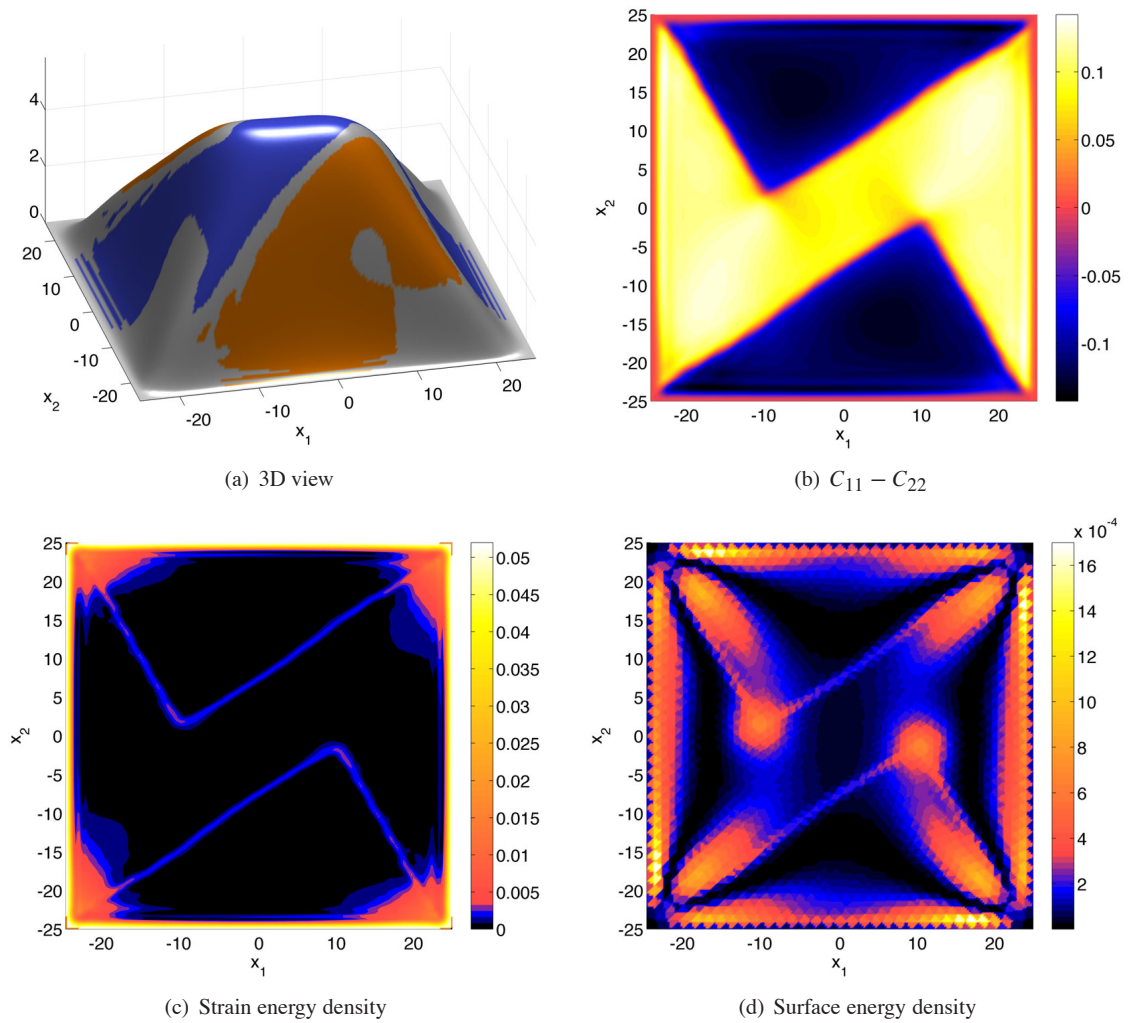


Figure 3.13: Detailed view of the tent formed with the crystallographic axis rotated 15 degrees with respect to the domain boundaries

shows the sections at $x_2 = 0$ and $x_2 = 12.5$ for various misalignments for comparison. A more detailed analysis of the tent shape formed with the 15 degree misalignment is shown in Figure 3.13.

It is clear that the shape significantly changes as the misalignment increases. Indeed, the shape becomes less of a square pyramid and more of an elongated mesa with a flat top. Further the height decreases dramatically: the height at the center falls 6%, 14%, and 22% with a misalignment of 5° , 10° , and 15° , respectively, relative to a perfectly oriented one. Indeed at 15° the center dips down.

In all these cases, one still has the four sectors of alternating variants. The four ridges that separate the variants follow closely the preferred crystallographic orientation. These, however, are no longer aligned with the squares of the square domain and consequently do not meet at the center of the domain. Instead, the four ridges create a square in the center whose size increases with misalignment. This square is subject to complex deformation as it tries to lie close to one of the energy wells. Table 3.3 confirms this showing increasing energy with misalignment.

These results indicate that for the parameters chosen here, a mismatch of less than 10 degrees in crystallographic orientation and physical domain orientation will somewhat, but not significantly affect the deformed shape. However, at 15 degrees, the outcome is quite different.

3.5.5 Rectangular domain

Figures 3.14(a) and 3.14(b) show the equilibrated tent formed on rectangular domains of aspect ratio 0.8 and 0.5, respectively. The crystallographic axis is aligned with the domain. The ridges separating the variants continue to follow their preferred orientation: so the resulting shape is an elongated roof-top. However, the ridge on top is rounded, with the curvature decreasing with increasing aspect ratio. This shape is determined by the competition between interfacial energy along the top ridge and the triple points where the top-ridge meets the two inter-variant ridges. The former scales as aspect ratio and the latter is independent of it. Therefore the interfacial energy dominates for longer domains, giving a rounded top, while the ‘triple-point energy’ dominates the more square domains, giving a less-rounded top.

3.6 The regular tent revisited

Let us return to the situation described in Section 3.5.1, and further examine the ridge and the tip. In order to do so, it is convenient to make a coordinate transform that rotates the coordinates by $\pi/4$ so that the ridge forms parallel to the coordinate axes. The energy is transformed accordingly and the energy wells are now located at

$$C = \begin{pmatrix} 1 + \frac{1}{2}\xi^2 & \pm\frac{1}{2}\xi^2 \\ \pm\frac{1}{2}\xi^2 & 1 + \frac{1}{2}\xi^2 \end{pmatrix} \quad (3.35)$$

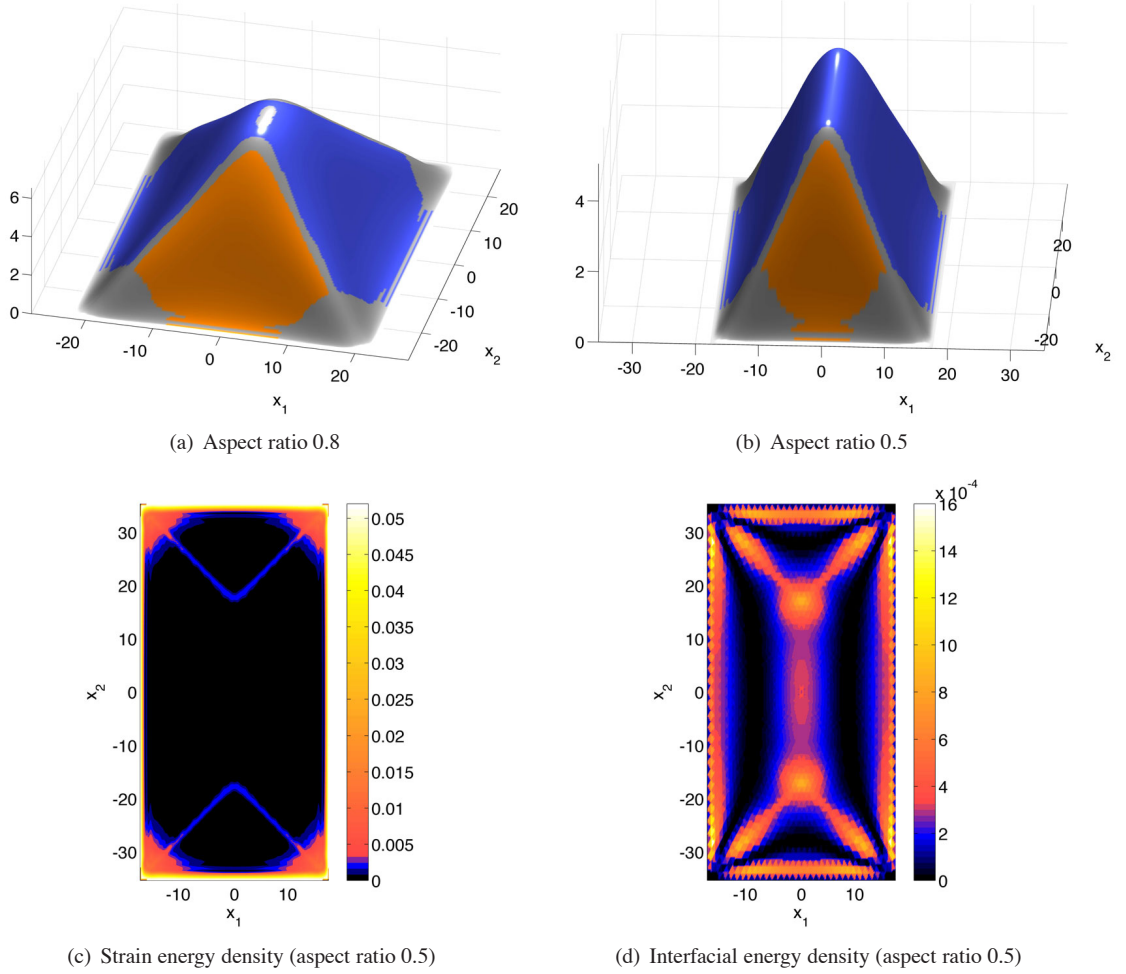


Figure 3.14: Tent shapes formed on a rectangular domain

with C_{12} the non-convex direction. We do not consider any boundary conditions.

Consider a ridge running along $x_2 = \text{constant}$. We anticipate that the deformation gradient to depend only on x_1 . So we look for a solution of the form

$$F_{\text{Ridge}} = \begin{pmatrix} \alpha(x_1) & 0 \\ \beta(x_1) & 1 \\ \gamma(x_1) & \frac{1}{\sqrt{2}}\xi \end{pmatrix}. \quad (3.36)$$

It is easy to verify that this satisfies the compatibility equation

$$\text{curl } F_{\text{Ridge}} = 0, \quad \text{or} \quad (F_{\text{Ridge}})_{i\alpha,\beta} = (F_{\text{Ridge}})_{i\beta,\alpha} \text{ where } i = 1\dots 3 \text{ and } \alpha, \beta = 1\dots 2, \quad (3.37)$$

which ensures that this is indeed a gradient. Plugging this into the equilibrium equation

$$\Delta^2 y + \text{Div} \sigma = 0, \quad (3.38)$$

noting that everything is independent of x_2 , and integrating once with respect to x_1 leads to second-order ordinary differential equations for α , β , and γ . These equations are

$$\alpha'' = (4a + c) \left(\alpha^2 + \beta^2 + \gamma^2 - 1 - \frac{\xi^2}{2} \right) \alpha, \quad (3.39)$$

$$\begin{aligned} \beta'' &= (4a + c) \left(\alpha^2 + \beta^2 + \gamma^2 - 1 - \frac{\xi^2}{2} \right) \beta \\ &\quad + 2b \Phi' \left(2\beta + \sqrt{2}\xi\gamma \right) \left(4 \left(\beta + \frac{\xi}{\sqrt{2}}\gamma \right)^2 - \xi^4 \right)^2 \\ &\quad + 16b \Phi \left(2\beta + \sqrt{2}\xi\gamma \right) \left(4 \left(\beta + \frac{\xi}{\sqrt{2}}\gamma \right)^2 - \xi^4 \right) \left(\beta + \frac{\xi}{\sqrt{2}}\gamma \right), \end{aligned} \quad (3.40)$$

$$\begin{aligned} \gamma'' &= (4a + c) \left(\alpha^2 + \beta^2 + \gamma^2 - 1 - \frac{\xi^2}{2} \right) \gamma \\ &\quad + b\xi\sqrt{2} \Phi' \left(2\beta + \sqrt{2}\xi\gamma \right) \left(4 \left(\beta + \frac{\xi}{\sqrt{2}}\gamma \right)^2 - \xi^4 \right)^2 \\ &\quad + 8\sqrt{2}b\xi \Phi \left(2\beta + \sqrt{2}\xi\gamma \right) \left(4 \left(\beta + \frac{\xi}{\sqrt{2}}\gamma \right)^2 - \xi^4 \right) \left(\beta + \frac{\xi}{\sqrt{2}}\gamma \right), \end{aligned} \quad (3.41)$$

where the prime denotes differentiation with respect to x_1 . If $(4a + c)$ is large, then we may replace the first equation with the constraint

$$\alpha^2 + \beta^2 + \gamma^2 = 1 + \frac{1}{2}\xi^2. \quad (3.42)$$

This in turn implies that

$$C_{11} = C_{22} = 1 + \frac{1}{2}\xi^2 \quad (3.43)$$

so that C traverses along the low-energy C_{12} direction across the ridge.

With the change of variables,

$$x = \beta - \frac{\sqrt{2}}{\xi}\gamma, \quad y = \beta + \frac{\xi}{\sqrt{2}}\gamma, \quad (3.44)$$

these equations simplify to

$$x'' = 0 \quad (3.45)$$

$$\begin{aligned} y'' &= b(2 + \xi^2) \Phi'(2y) \left((2y)^2 - \xi^4 \right)^2 + 8b(2 + \xi^2) \Phi(2y) \left((2y)^2 - \xi^4 \right) y \\ &= b \left(1 + \frac{\xi^2}{2} \right) \frac{\partial}{\partial y} \left(\Phi(2y) \left((2y)^2 - \xi^4 \right)^2 \right). \end{aligned} \quad (3.46)$$

Now assume for the moment that $\Phi = 1$. Recall that we introduced this function to increase the energy barrier between the wells. Then, the second of the equations above reduces to

$$y'' = b \left(1 + \frac{\xi^2}{2} \right) \frac{\partial}{\partial y} \left(\left((2y)^2 - \xi^4 \right)^2 \right) \quad (3.47)$$

which has a solution

$$y = \frac{\xi^2}{2} \tanh \left(-2\xi^2 \sqrt{b(2 + \xi^2)} x_1 \right) \quad (3.48)$$

that smoothly transitions from $-\xi^2/2$ to $\xi^2/2$ over a length-scale of $\left(2\xi^2 \sqrt{b(2 + \xi^2)} \right)^{-1}$. Thus, we have constructed a solution for which F_{Ridge} transitions between

$$\begin{pmatrix} 1 & 0 \\ 0 & 1 \\ \frac{1}{\sqrt{2}}\xi & \frac{1}{\sqrt{2}}\xi \end{pmatrix} \quad \text{and} \quad \begin{pmatrix} 1 & 0 \\ 0 & 1 \\ -\frac{1}{\sqrt{2}}\xi & \frac{1}{\sqrt{2}}\xi \end{pmatrix}. \quad (3.49)$$

while satisfying the constraint (3.43). Indeed, a simple calculation shows that $C_{12} = y$, so that C_{12} changes as a hyperbolic tangent as we go across the ridge according to (3.48). This shows that the width of a typical ridge is of the order $\left(2\xi^2 \sqrt{b(2 + \xi^2)} \right)^{-1}$. Finally, note that the x corresponds to a rotation, and thus its details depend on the exact boundary conditions.

If $\Phi \neq 1$, we are unable to find the profile explicitly, though the above results hold qualitatively. Further, as the barrier increases, the transition region is smaller.

In summary, these calculations show that one can traverse the ridge using the low-energy direction as suggested by our computations.

We now turn to the tip, and examine whether it can be formed by two crossing ridges. We look

for a solution where the deformation gradient is of the form

$$F_{\text{Tip}} = \begin{pmatrix} \alpha_1(x_1) & \alpha_2(x_2) \\ \beta_1(x_1) & \beta_2(x_2) \\ \gamma_1(x_1) & \gamma_2(x_2) \end{pmatrix}. \quad (3.50)$$

It is easy to verify that while it satisfies the compatibility equation, it can not satisfy the equilibrium equation (3.38). In other words, the deformation at the tip has to be more complicated than two crossing ridges.

3.7 Conclusions

The results demonstrate the feasibility of using subdivision surfaces to computationally study thin films undergoing martensitic phase transformations. Specifically, they provide a discretization which is able to naturally and accurately resolve the higher-order derivatives, especially in situations involving non-convex (multi-well) energies. Previously, subdivision surfaces have been used only in the context of thin shell structures that do not undergo phase transformations.

The work presented here also provides insights into tent-like deformations which are potentially of interest for microactuation. The computations demonstrate that this deformation can be quite complex even in the case where the crystallographic axis is perfectly aligned with the physical domain. In particular, the deformation involves inhomogeneous in-plane stretches in addition to out-of-plane motions and thus can not be described as an antiplane shear motion. The results also show an unexpected breaking of the symmetry at the tip. We provide analytic studies that confirm the computational results. Second, the numerical calculations show that the overall structure of the tent remains stable for small deviations but begins to deviate substantially beyond 10 degrees of misalignment. Thus we infer that manufacturing of actuators accurate to about 10 angular degrees should be sufficient to still achieve suitable results. Finally, we show how the shape changes when the released region is a rectangle instead of a square.

In this paper we studied the equilibrium states for tent-like structures in martensitic thin films. To examine the reverse transformation of the tent to the flat state, one has to introduce a temperature field and a temperature dependent energy, which is not trivial in view of the geometry of the deformed state. This is a matter for further investigation.

An interesting extension to the current simulation would be to allow for adaptive refinement of the discretization. This is especially beneficial in the current situation involving phase transforming materials since we have small regions of large gradients separating large regions of small gradients, and this partitioning is *a priori* unknown. As demonstrated in [39], subdivision surfaces lend themselves to a natural method for adaptive refinement.

Chapter 4

A sharp interface model for the evolution of martensitic phase boundaries

In this chapter, a model for the quasistatic evolution of a martensitic phase boundary is presented. We show the existence of solutions to this model in the sense of sets of finite perimeter. In the first section, a brief and somewhat heuristic introduction to the model and its difficulties is provided. The second section shows the mathematical results. In the third section, a pinned state of the phase boundary is examined numerically using the sharp interface model. The goal is to examine the pinning effects of inhomogeneities on the evolution of a martensitic phase boundary. Macroscopically, these phase transitions are commonly modeled using a rate-independent evolution law, which naturally includes a stick-slip behavior and thus leads to rate-independent hysteresis. Microscopically, however, one usually assumes that the evolution is governed by a linear relation between the thermodynamic driving force and the velocity of the phase boundary. The goal of this chapter and the following one is to provide some insight into the bridging between these two scales.

The model is introduced in a somewhat heuristic manner in the first section of this chapter. The exact model is then presented in Section 4.2, where the existence of a solution is proved. Section 4.3 then provides a numerical estimate for the pinning force that can arise from the elastic effects described by the sharp interface model.

4.1 Introduction to the model

The model we are using to describe the evolution of a martensitic phase boundary will consist of three basic assumptions. These are the nonconvex elastic energy density, a surface energy to penalize phase boundaries, and a kinetic relation between the thermodynamic driving force and the normal velocity of the phase boundary. In order to formulate the problem consistently, a finite time discretization scheme is then introduced, the convergence of which is proved in Section 4.2. In the

following, we will restrict ourselves to the case of two phases in an anti-plane shear model, to simplify the notation. The generalizations should be straightforward.

The elastic energy density. As described before, shape memory alloys are commonly modeled by a multiwell energy approach. Considering a material with two distinct phases, one can assume that the equilibrium configuration is given by the minimizer of an elastic energy, where for each material point the phase, and thus the transformation strain, can be individually chosen [48]. Assuming a linearly elastic material in anti-plane shear, this leads to an energy of the form

$$\min_E \min_u \int_{\Omega} \frac{1}{2} |\nabla u(x) - \xi_E(x)|^2 dx \quad (4.1)$$

with the deformation $u: \Omega \rightarrow \mathbb{R}$ defined on the domain of the body $\Omega \subset \mathbb{R}^n$, and the transformation strain $\xi_E(x)$. The transformation strain is assumed to admit discrete values, a different one for $x \in E$ and $x \in \Omega \setminus E$. The set E is the subdomain of Ω occupied by the first of the two phases. The results generalize in a straightforward manner to the linearly elastic case, but the notation is somewhat simplified in anti-plane shear. Additionally to the transformation strain stemming from the phase boundary, there can be regions in the body that do not transform, and exhibit an energy minimum at a third, different strain. Such precipitates are modeled by forcing $\xi_E(x)$ to be a specific value in certain fixed subdomains A_i independently of E . An example of such a domain is depicted in Figure 4.1.

As discussed, for example in [11], minimizers for nonconvex energies of this kind are not generally attained. One can however relax the notion of a minimizer to include objects like (gradient) Young measures as limits of minimizing sequences describing phase mixtures and microstructure. We are going to take a slightly different route, since it is the goal to study the evolution of phase boundaries. Our approach will lead to a gradient flow of the phase boundary with respect to the energy in the system.

Let us, for a moment, therefore, fix the phase distribution. Given such a phase distribution, and thus given the set occupied by phase one, denoted by E , one can write an elastic energy as an integral over the elastic energy density W as

$$\mathcal{F}_{\text{elastic}}(E) = \min_u \int_{\Omega} W(\nabla u, E) dx := \min_u \int_{\Omega} \frac{1}{2} |\nabla u(x) - \xi_E(x)|^2 dx. \quad (4.2)$$

The minimization naturally has to be carried out in a suitable function space endowed with appropriate boundary conditions. Assuming now smoothness of the phase boundary $\Gamma = \partial E$, one can compute the change of elastic energy in the system upon the evolution of Γ with any given normal

velocity v_n [2, 41], which yields

$$\frac{d}{dt} \mathcal{F}_{\text{elastic}} = \frac{d}{dt} \int_{\Omega} W(\nabla u, E) \, dx \quad (4.3)$$

$$= \int_{\Omega} \dot{W}(\nabla u, E) \, dx + \int_{\Gamma} \llbracket W(\nabla u, E) \rrbracket v_n \, dx_{\Gamma} \quad (4.4)$$

$$= \int_{\Omega} \frac{\partial W(\nabla u, E)}{\partial \nabla u} \nabla \dot{u} \, dx + \int_{\Gamma} \llbracket W \rrbracket v_n \, dx_{\Gamma} \quad (4.5)$$

$$= - \int_E \operatorname{div} \sigma \dot{u} \, dx - \int_{\Omega \setminus E} \operatorname{div} \sigma \dot{u} \, dx \quad (4.6)$$

$$- \int_{\Gamma} [\sigma \dot{u}] \cdot n \, dx_{\Gamma} - \int_{\Gamma} \llbracket W \rrbracket v_n \, dx_{\Gamma} \quad (4.7)$$

$$= \int_{\Gamma} \langle \sigma \rangle \llbracket \nabla u \rrbracket v_n \, dx_{\Gamma} - \int_{\Gamma} \llbracket W \rrbracket v_n \, dx_{\Gamma} \quad (4.8)$$

$$= - \int_{\Gamma} (\llbracket W \rrbracket - \langle \sigma \rangle \llbracket \nabla u \rrbracket) v_n \, dx_{\Gamma} \quad (4.9)$$

$$=: - \int_{\Gamma} f v_n \, dx_{\Gamma}. \quad (4.10)$$

Here we have used the identities

$$\frac{\partial W(\nabla u, E)}{\partial \nabla u} = \sigma \quad (4.11)$$

$$\llbracket \sigma \dot{u} \rrbracket \cdot n = (1/2) (\langle \dot{u} \rangle \llbracket \sigma \rrbracket + \llbracket \dot{u} \rrbracket \langle \sigma \rangle) \quad (4.12)$$

$$\llbracket \dot{u} \rrbracket = - \llbracket \nabla u \rrbracket v_n \quad (4.13)$$

$$\operatorname{div} \sigma = 0 \quad \text{within } E \text{ and } \Omega \setminus E \quad (4.14)$$

$$\llbracket \sigma \cdot n \rrbracket = 0 \quad \text{on the phase boundary.} \quad (4.15)$$

Further details can be found in [2]. This gives us a relation between the change in elastic energy in the system and the normal velocity of the phase boundary.

The surface energy. In a similar manner as seen in Chapter 3, one can add a surface term to the total energy of a sharp interface model. In this case we will simply penalize the total length of the phase boundary by a term

$$\mathcal{F}_{\text{surface}} = \gamma \int_{\Omega} |\nabla \chi_E| \, dx \quad (4.16)$$

with a coefficient γ . This is to be understood in the sense of sets of finite perimeter or functions of bounded variation [9, 33]. The term can be seen as an abbreviation of $\sup_{\|\phi\| < 1} \int_{\Omega} \chi_E \operatorname{div} \phi$ among all continuously differentiable test functions ϕ . Physically this term is commonly interpreted as an approximation of the energy due to a localized, atomistic mismatch at the surfaces of strain discontinuity. Mathematically it leads to a regularization of the problem, and in case it is finite for some given set E , it is equal to the length of the perimeter of E within the domain Ω . A set E for

which this term is finite is called a set of finite perimeter.

This surface energy leads, again upon evolution of the phase boundary Γ with a normal velocity v_n , to the well-known [40] curvature term

$$\frac{d}{dt} \mathcal{F}_{\text{surface}} = - \int_{\Gamma} \gamma \kappa v_n. \quad (4.17)$$

The kinetic relation and the free discontinuity problem. Bringing together (4.3) and (4.17), one can see that the change in total energy upon the evolution of the phase boundary can be written as

$$\frac{d}{dt} \mathcal{F} = - \int_{\Gamma} f v_n, \quad (4.18)$$

where f is the thermodynamic driving force (also called the chemical potential) in the system, consisting of a nonlocal term stemming from the elastic energy in the system and the curvature term, i.e. $f = \llbracket W \rrbracket - \langle \sigma \rangle \llbracket \nabla u \rrbracket - \gamma \kappa v_n$. In order to consider this as an evolution equation one has to make a kinetic assumption that relates the normal velocity of the phase boundary to the driving force. We regard our shape memory alloy as a dissipation-governed system and thus assume proportionality between f and v_n [4]. This leads us to the free discontinuity problem

$$f = v_n, \quad (4.19)$$

where we have, for simplicity, taken the proportionality constant—the mobility of the phase boundary—to be equal to one.

The mathematical difficulty of this problem lies in the fact that it is a free discontinuity evolution that is coupled to an elliptic partial differential equation. Similar difficulties arise in gradient flows in metric spaces [10], as well as in rate-independent processes [55]. There, one usually introduces an implicit time discretization scheme to approximate a solution to the problem. We will make a similar approach, even though we are neither dealing with a metric space nor is our problem rate-independent. The assumption of linear evolution leads here to an additional difficulty.

The finite time discretization scheme. For a fixed time-step h , and a set of finite perimeter E_0 , consider the following minimization problem. Find a set E , minimizing the energy

$$\mathcal{F}(E) = \mathcal{F}_{\text{elastic}}(E) + \mathcal{F}_{\text{surface}}(E) + \int_{E \Delta E_0} \text{dist}(x, \partial E_0) \, dx. \quad (4.20)$$

After proving that such a minimizer always exists, one can iteratively apply the minimization scheme and define an approximate solution as an in-time piecewise constant interpolation between the minimizers for each time step. The ‘distance’ term (an integral over the symmetric set difference of E and E_0 , denoted here by $E \Delta E_0$) in the energy is chosen such that its variation, for small h ,

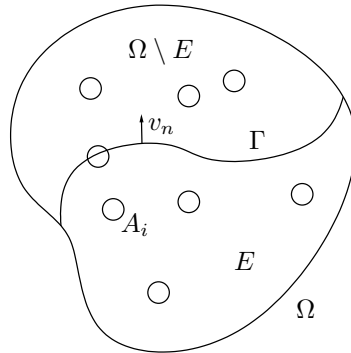


Figure 4.1: Domain occupied by a phase transforming elastic body

is approximately the normal velocity of the phase boundary. This is the approach taken in [8, 53] for the related problem of a curvature flow. The second task is then to show convergence of the approximate solutions, as $h \rightarrow 0$, to a suitable solution of the original problem.

Since the sequence of piecewise constant approximate solutions is a sequence of characteristic functions on the space-time domain $\Omega \times [0, T]$, it naturally converges weakly* in L^∞ . It is however necessary to establish *strong* convergence here so that the resulting limit is again a characteristic function and one can view the problem as a set evolution. In order to do this, it is necessary to bound the total variation of the sequence of solutions uniformly both in space and in time. The uniform bound in space will be obtained directly from the uniform bound on the perimeter of the solutions. In order to derive the uniform bound in time, a density estimate on minimizing sets of the time-step problem is used in [53]. This estimate requires the forcing on the phase boundary to be uniformly bounded in L^∞ . Stress concentrations in the elasticity case, however, prevent its direct use. In order to overcome this difficulty, we regularize the elastic energy density by mollifying the transformation strain. The size ε of the mollifier can then vanish in the right relation with the time-step h and one can still establish strong convergence of the solution. This is detailed in the following section, where we use many similar ideas as [53].

4.2 Statement and analysis of the model

4.2.1 The model

In this model for the evolution of a phase boundary, we consider an elastic body occupying a domain $\Omega \subset \mathbb{R}^n$ open, bounded, with C^2 boundary, as depicted in Figure 4.1. The material exhibits two phases, occupying E , and $\Omega \setminus E$, respectively. It is assumed to be linearly elastic in both regions, however with a different transformation strain. There can also be a non-transforming

region $A = \bigcup_i A_i$ in the body. The piecewise constant transformation strain is thus given as

$$\xi_E(x) = \begin{cases} \xi^+ & \text{for } x \in \Omega \setminus (E \cup A) \\ \xi^- & \text{for } x \in E \setminus A \\ \xi^A & \text{for } x \in A. \end{cases} \quad (4.21)$$

For an anti-plane shear displacement $u: \Omega \rightarrow \mathbb{R}$, we consider, as discussed before, the elastic energy

$$\mathcal{F}_{\text{elastic}} = \int_{\Omega} W := \int_{\Omega} \frac{1}{2} |\nabla u - \xi_E|^2. \quad (4.22)$$

Additionally we add a surface energy, proportional to the length of the phase boundary Γ ,

$$\mathcal{F}_{\text{surface}} = \gamma \int_{\Omega} |\nabla \chi_E|. \quad (4.23)$$

The goal is to prove the existence of a solution, in the form of an evolving set $E(t)$, according to the kinetic law

$$v_n = f, \quad (4.24)$$

for the nonlocal thermodynamic driving force f , wherever Γ is smooth enough.

To this end, one first has to prove some estimates on the involved energies and the deformation gradient.

4.2.2 Local estimates on the elastic energy

As mentioned in Section 4.1, the piecewise constant transformation strain can lead to stress concentrations for certain configurations of the phase boundary. In order to prove compactness of the time discrete solutions later, such stress concentrations must only occur in a very controlled manner. To this end, we regularize the transformation strain and will let the regularization tend to zero together with the time step in an appropriate way.

We first therefore define the mollified transformation strain

$$\xi_E^\varepsilon(x) = (\eta^\varepsilon * \xi_E)(x) = \int_{\Omega} \eta^\varepsilon(x-y) \xi_E(y) dy. \quad (4.25)$$

Also, set $H = \{u \in H^1(\Omega), \text{ together with boundary conditions}\}$ and denote its dual space by H' . The possible boundary conditions include part Dirichlet, part Neumann boundary data, as well as natural Neumann boundary conditions, together with a condition on the average of u in order to make the elliptic problem well-posed. The dual space to H is not identified with H , instead it is seen as the space pivoted around the space L^2 by the inclusion $H \subset L^2 \subset H'$. This construction

can, for example, be found in [32, 18]. Consider now the elastic energy

$$\mathcal{F}_{\text{elastic}}(E) = \min_{u \in H} \int_{\Omega} \frac{1}{2} |\nabla u - \xi_E|^2 \quad (4.26)$$

and also the mollified elastic energy

$$\mathcal{F}_{\text{elastic}}^{\varepsilon}(E) = \min_{u^{\varepsilon} \in H} \int_{\Omega} \frac{1}{2} |\nabla u^{\varepsilon} - \xi_E^{\varepsilon}|^2. \quad (4.27)$$

It is clear from the theory of elliptic equations that such a minimizer always exists, since the transformation strain is a function in L^2 . One can then derive the following *a priori* bounds.

Lemma 4.2.1. *There is a constant M independent of E and ε such that the following hold.*

- i.* $0 < \mathcal{F}_{\text{elastic}}(E) < M$ and $0 < \mathcal{F}_{\text{elastic}}^{\varepsilon}(E) < M$.
- ii.* For u, u^{ε} attaining the minimum in $\mathcal{F}_{\text{elastic}}(E)$ and $\mathcal{F}_{\text{elastic}}^{\varepsilon}(E)$, respectively, we find $\|\nabla u\|_{L^2} < M$ and $\|\nabla u^{\varepsilon}\|_{L^2} < M$.
- iii.* $\|\nabla u^{\varepsilon}\|_{L^{\infty}} < \frac{M}{\varepsilon^n}$.

Proof. *i.* Consider the test function $u = 0$ on Ω . Then $\int_{\Omega} |\xi_E|^2 < m(\Omega) \max(\xi^{\pm})^2$. The same holds for $\mathcal{F}_{\text{elastic}}^{\varepsilon}$.

ii. Since $\nabla \cdot \xi_E \in H^1$, we know that u solves the equation

$$\int_{\Omega} \nabla u \cdot \nabla u = \int_{\Omega} \xi_E \cdot \nabla u. \quad (4.28)$$

From there we deduce that

$$\|\nabla u\|_{L^2}^2 \leq \|\xi\|_{L^{\infty}} \|\nabla u\|_{L^1} \leq \sqrt{m(\Omega)} \|\xi\|_{L^{\infty}} \|\nabla u\|_{L^2} \quad (4.29)$$

and the same holds for u^{ε} .

iii. Note that u^{ε} , as a minimizer of the energy $\int_{\Omega} |\nabla u^{\varepsilon} - \xi_E^{\varepsilon}|^2$ is the unique solution of the equation

$$\Delta u^{\varepsilon} = \nabla \cdot \xi_E^{\varepsilon}, \quad u \in H. \quad (4.30)$$

We can therefore, by the representation theorem, write u as the convolution of the transformation strain with the Green's function for the problem, so that

$$\begin{aligned} u^{\varepsilon} &= G * \xi_E^{\varepsilon} \\ &= G * (\eta^{\varepsilon} * \xi_E) \\ &= \eta^{\varepsilon} * (G * \xi_E) \\ &= \eta^{\varepsilon} * u, \end{aligned} \quad (4.31)$$

where u is the minimizer in the unmollified elastic energy. From there one can calculate

$$\begin{aligned}
|\nabla u^\varepsilon(x)| &= |\nabla(\eta^\varepsilon * u)(x)| \\
&= \left| \int_{\Omega} \nabla_x \eta^\varepsilon(x-y)u(y)dy \right| \\
&\leq \|\nabla \eta^\varepsilon\|_{L^\infty} \|u\|_{L^1} \\
&\leq \|\nabla \eta^\varepsilon\|_{L^\infty} \|u\|_{L^2} \sqrt{m(\Omega)} \leq \frac{M}{\varepsilon^n},
\end{aligned} \tag{4.32}$$

which proves the statement¹. □

Next, we will prove an estimate of the change in mollified elastic energy if an area of a certain size changes from one transformation strain to the other. Such a proposition will make it possible to use the aforementioned density lemma for balls of small enough radius.

Proposition 4.2.2. *There exists a uniform constant M such that given two sets of finite perimeter E_1 and E_2 , we have*

$$|\mathcal{F}_{\text{elastic}}^\varepsilon(E_1) - \mathcal{F}_{\text{elastic}}^\varepsilon(E_2)| \leq \frac{M}{\varepsilon^n} \cdot m(E_1 \Delta E_2). \tag{4.33}$$

Proof. Assume that $\mathcal{F}_{\text{elastic}}^\varepsilon(E_1) \leq \mathcal{F}_{\text{elastic}}^\varepsilon(E_2)$. Let $A = E_1 \Delta E_2$ and ξ_A , supported on A , such that $\xi_{E_2}^\varepsilon = \xi_{E_1}^\varepsilon + \xi_A$. Consider the minimizer u_1^ε of the energy

$$\int_{\Omega} |\nabla u_1^\varepsilon - \xi_{E_1}^\varepsilon|^2 \tag{4.34}$$

and use it as a test function for the larger energy. This yields

$$\begin{aligned}
\mathcal{F}_{\text{elastic}}^\varepsilon(E_2) &= \min_u \int_{\Omega} \frac{1}{2} |\nabla u - \xi_{E_2}^\varepsilon|^2 \\
&\leq \int_{\Omega} \frac{1}{2} |\nabla u_1^\varepsilon - \xi_{E_1}^\varepsilon - \xi_A|^2 \\
&= \int_{\Omega} \frac{1}{2} |\nabla u_1^\varepsilon - \xi_{E_1}^\varepsilon|^2 + \int_{\Omega} \frac{1}{2} |\xi_A|^2 + \int_{\Omega} 2\xi_{E_1} \cdot \xi_A - \int_{\Omega} 2\nabla u_1 \cdot \xi_A \\
&\leq \mathcal{F}_{\text{elastic}}^\varepsilon(E_1) + \frac{1}{2} m(A) (\|\xi_A\|_{L^\infty}^2 + 2\|\xi_{E_1}\|_{L^\infty} \|\xi_A\|_{L^\infty}) \\
&\quad + m(A) \|\xi_A\|_{L^\infty} \|\nabla u_1^\varepsilon\|_{L^\infty} \\
&\leq \mathcal{F}_{\text{elastic}}^\varepsilon(E_1) + \frac{M}{\varepsilon^n} m(A).
\end{aligned} \tag{4.35}$$

□

¹In order for the Green's function to be regular enough to perform this calculation, the boundary of Ω has to be smooth. One can also refer to the theorems about higher regularity of solutions to elliptic equations, for example in [32], which require a C^2 boundary.

4.2.3 The implicit time discretization

We discretize equation (4.24) using an implicit finite time-step scheme. For $h > 0, \varepsilon > 0$, consider the energy function

$$\mathcal{F}^{h,\varepsilon}(E, E_0) = \min_{u^\varepsilon \in H} \int_{\Omega} |\nabla u^\varepsilon - \xi_E^\varepsilon|^2 + \int_{\Omega} |\nabla \chi_E| + \frac{1}{h} \int_{E \Delta E_0} \text{dist}(\cdot, \partial E_0). \quad (4.36)$$

We will call the first term the *elastic term*, the second term is the *perimeter term* and the third term is the *distance term*.

Theorem 4.2.3. *For a given set of finite perimeter E_0 , the set function $\mathcal{F}^{h,\varepsilon}(\cdot, E_0)$ admits a minimizer E . Furthermore, E has finite perimeter.*

Proof. The energy $\mathcal{F}^{h,\varepsilon}$ is non-negative, and thus is uniformly bounded from below. Consider therefore a minimizing sequence of sets $\{E_k\}_{k=1}^\infty$ for the energy $\mathcal{F}^{h,\varepsilon}$. The elastic energy term in $\mathcal{F}^{h,\varepsilon}$ is uniformly bounded according to Lemma 4.2.1. The third term, the distance term, is—for a fixed h —also uniformly bounded from both above and below. Therefore, one can find a (renumbered) subsequence such that $\int_{\Omega} |\nabla \chi_{E_k}|$, the perimeter of E_k is bounded uniformly in k . Thus, by Theorem 4.7 and 4.8 in [9] (SBV closedness and compactness), there exists a (renumbered) subsequence, and a set of bounded perimeter E , such that

$$\chi_{E_k} \rightarrow \chi_E \quad \text{in } L^1. \quad (4.37)$$

It remains to be shown that $\mathcal{F}^{h,\varepsilon}$ is lower semicontinuous with respect to this convergence. First, by Theorem 4.7 in [9], the perimeter term of $\mathcal{F}^{h,\varepsilon}$ is lower semicontinuous. The strong convergence in L^1 also immediately implies the continuity of the distance term. For the elastic term, note that the solution operator for the minimization problem of u^ε is continuous with respect to ξ_E^ε in H' . It is therefore clear that the minimizers and minima u_i^ε of $\int_{\Omega} |\nabla u_k^\varepsilon - \xi_{E_k}^\varepsilon|^2$ converge to a minimizer and minimum of $\int_{\Omega} |\nabla u_k^\varepsilon - \xi_E^\varepsilon|^2$. This establishes the lower semicontinuity of $\mathcal{F}^{h,\varepsilon}$. \square

Given an initial value $E(0) = E_0$, and setting $h = \frac{T}{N}$, $N \in \mathbb{N}$ we can now iteratively, up to $k = N$, define the *time-discrete solution* to be

$$E^{h,\varepsilon}(t) = \begin{cases} \operatorname{argmin} \mathcal{F}(\cdot, E^{h,\varepsilon}(t-h)) & \text{if } t = kh \\ E^{h,\varepsilon}((k-1)h) & \text{for } t \in ((k-1)h, kh). \end{cases} \quad (4.38)$$

This is the piecewise constant interpolation between the iterated minimizers of the time-step minimization problem. Furthermore, we define for a sequence $\{h_i\}_{i=1}^\infty$ such that $h \rightarrow 0$, the sequence of time-discrete solutions $\{E^{h_i,\varepsilon}(t)\}_{i=1}^\infty$.

4.2.4 Compactness of the time-discrete solution

We now show that the sequence of time-discrete solutions is strongly equicontinuous in h . This enables us to use the Arzela-Ascoli theorem to establish strong convergence of a subsequence.

For the rest of this section we will assume the scaling $\varepsilon = h^{1/n}$ and write $\mathcal{F}^h(E, E_0) := \mathcal{F}^{h, h^{1/n}}(E, E_0)$, as well as $E^h(t) := E^{h, h^{1/n}}(t)$. The constant C is independent of h , but may depend on n , Ω , T , and E_0 , and possibly change from line to line.

Compactness in space. The compactness in the spatial variables follows directly from the uniform bound on the perimeter of the transformed set E , which we presently prove.

Lemma 4.2.4. *Let $E^h(t)$ be the piecewise constant solution constructed above. Then*

$$\int_{\Omega} |\nabla \chi_{E^h(t)}| < C. \quad (4.39)$$

Proof. Let $C = \sup_{\varepsilon > 0} \mathcal{F}_{\text{elastic}}^{\varepsilon}(E_0) + \int_{\Omega} |\nabla \chi_{E_0}| < \infty$ by Lemma 4.2.1. Assume, by contradiction, that for some $t < T$, we have $\int_{\Omega} |\nabla \chi_{E^h(t)}| > C$. That means that there must exist a $k \leq N$, such that

$$\sup_{\varepsilon > 0} \mathcal{F}_{\text{elastic}}^{\varepsilon}(E^h(kh)) + \int_{\Omega} |\nabla \chi_{E^h(kh)}| > \sup_{\varepsilon > 0} \mathcal{F}_{\text{elastic}}^{\varepsilon}(E^h((k-1)h)) + \int_{\Omega} |\nabla \chi_{E^h((k-1)h)}|. \quad (4.40)$$

This means, however, that $E^h(kh)$ can not be a minimizer of the finite time-step problem. \square

Proposition 4.2.5 (Compactness in space). *The time-discrete solution $E^h(t)$ satisfies*

$$\int_0^T \int_{\Omega} |\chi_{E^h(t)}(x + se) - \chi_{E^h(t)}(x)| \, dx dt \longrightarrow 0 \quad (4.41)$$

as $s \rightarrow 0$, uniformly in h for each unit vector $e \in \mathbb{R}^n$.

Proof. Approximating χ_{E^h} by smooth functions, we establish

$$\int_{\Omega} |\chi_{E^h(t)}(x + se) - \chi_{E^h(t)}(x)| \, dx \leq s \int_{\Omega} |\nabla \chi_{E^h}|. \quad (4.42)$$

Integration in time together with Lemma 4.2.4 gives the assertion. \square

Compactness in time. We now seek to establish a uniform bound on the total variation of the transformed set $E(t)$ in time. The major difficulty here is the inability of the distance term in the energy \mathcal{F}^h to yield such a bound by itself. If one were to assume, for example, a rate-independent evolution model, the distance term would be replaced by a penalization of the area $E_0 \triangle E$ via a

term of the form

$$m(E_0 \triangle E). \quad (4.43)$$

Such an evolution law therefore automatically yields a uniform bound on the total variation of $E(t)$, which then leads to the necessary strong compactness.

In our case, however, since one can find a dense set E_{bad} in Ω with arbitrarily low elastic and surface energy, the situation is more complicated. For $E_0 = E_{\text{bad}}$, no matter what the set in the next time-step looks like, the distance term vanishes. This way, one can generate a sequence of faster and faster oscillating phases on a large part of the domain. Such a sequence will certainly not converge strongly. It is the goal now to exclude such bad sets *a priori* through some assertions on the geometric properties of sets that minimize the time-step energy \mathcal{F}^h .

Lemma 4.2.6 (\mathcal{L}^n -density of minimizing sets). *Let $f \in L^\infty(\Omega)$ and assume E minimizes the functional*

$$\mathcal{F}(E) = \mathcal{F}_{\text{elastic}}^\varepsilon(E) + \int_{\Omega} f \chi_E + \int_{\Omega} |\nabla \chi_E| \quad (4.44)$$

among all measurable subsets of Ω . Then the density estimate,

$$\theta \leq \int_{B_\rho(x)} \chi_E \leq 1 - \theta, \quad (4.45)$$

holds for all $x \in \partial E$ and for all $0 < \rho < \frac{\gamma_n}{2(\|f\|_{L^\infty} + \frac{M}{\varepsilon^n})\omega_n^{1/n}} := \rho_0$ such that $B_\rho(x) \subset \Omega$. The constant M is the constant from Proposition 4.2.2 and θ is given by $\theta = (\frac{1}{4})^n$.

The constant ω_n is the \mathcal{L}^1 measure of the unit sphere in \mathbb{R}^n ; the constant γ_n is given by $\gamma_n = n\omega_n^{1/n}$.

Proof. We only show the lower density bound; the upper bound can be proved by considering the set E^c . First we show that for $\rho < \rho_0$ and x as above the set $E \cap B_\rho(x)$ contains a part of the boundary of $B_\rho(x)$, i.e.,

$$\int_{\partial B_\rho(x)} \chi_E \, d\mathcal{H}^{n-1} > 0. \quad (4.46)$$

The excluded situation as well as the possible behavior are illustrated in Figure 4.2. If that does not hold for some $r \in (0, \rho)$, we conclude from the isoperimetric inequality $\int_{\mathbb{R}^n} |\nabla \chi_E| \geq \gamma_n \left(\int_{\mathbb{R}^n} \chi_E \right)^{\frac{n-1}{n}}$ that

$$\gamma_n \left| \int_{B_r(x)} \chi_E \right|^{\frac{n-1}{n}} \leq \int_{B_r(x)} |\nabla \chi_E|. \quad (4.47)$$

Further, the minimality of the set E requires

$$\int_{B_r(x)} |\nabla \chi_E| \leq \left(\|f\|_{L^\infty} + \frac{M}{\varepsilon^n} \right) \int_{B_r(x)} \chi_E = \left(\|f\|_{L^\infty} + \frac{M}{\varepsilon^n} \right) m(\chi_E \cap B_r(x)) \quad (4.48)$$

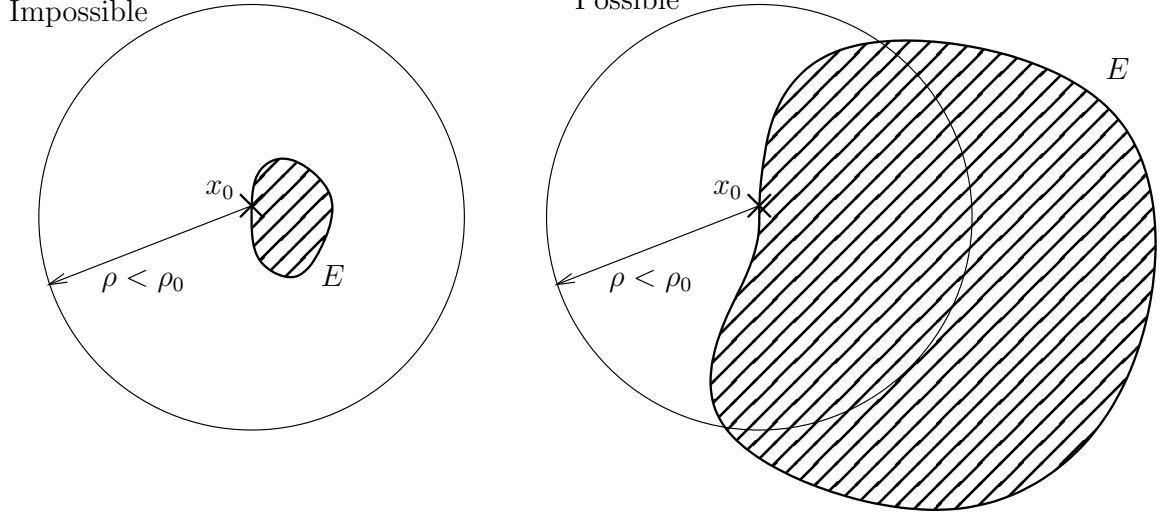


Figure 4.2: For a ball centered on the boundary of the set E with small enough radius, the set E actually has to intersect the boundary of the ball. The situation on the left is therefore excluded, a possible minimizing set is shown on the right for comparison.

by comparing the energies of the sets E and the set $E \setminus B_r(x)$. Therefore

$$\omega_n \rho^n \geq \int_{B_r(x)} \chi_E \geq \left(\frac{\gamma_n}{\|f\|_{L^\infty} + \frac{M}{\varepsilon^n}} \right)^n, \quad (4.49)$$

which contradicts the upper bound for ρ given above.

In the second step we define, for a fixed $\sigma \in (0, \frac{\rho}{2})$, the comparison set

$$E' = E \setminus \left(B_{\frac{\rho}{2} + \sigma}(x) \setminus B_{\frac{\rho}{2} - \sigma}(x) \right), \quad (4.50)$$

as shown in Figure 4.3. For the volume $V(\sigma) := m(E \cap (B_{\frac{\rho}{2} + \sigma}(x) \setminus B_{\frac{\rho}{2} - \sigma}(x)))$, using again the isoperimetric inequality and the minimality of E , we find

$$\gamma_n V(\sigma)^{\frac{n-1}{n}} - A^+\left(\frac{\rho}{2} - \sigma\right) - A^-\left(\frac{\rho}{2} + \sigma\right) \quad (4.51)$$

$$\leq A^-\left(\frac{\rho}{2} - \sigma\right) + A^+\left(\frac{\rho}{2} + \sigma\right) + \left(\|f\|_{L^\infty} + \frac{M}{\varepsilon^n} \right) V(\sigma). \quad (4.52)$$

Here $A^+(r), A^-(r)$ denote the sectional surfaces of E with the sphere $\partial B_r(x)$, defined by the outer and inner trace of χ_E on $\partial B_r(x)$, respectively. Taking the derivative of the volume of the set in the sense of measures shows that, for almost all σ ,

$$\frac{d}{d\sigma} V(\sigma) = A^+\left(\frac{\rho}{2} - \sigma\right) + A^-\left(\frac{\rho}{2} + \sigma\right) = A^-\left(\frac{\rho}{2} - \sigma\right) + A^+\left(\frac{\rho}{2} + \sigma\right). \quad (4.53)$$

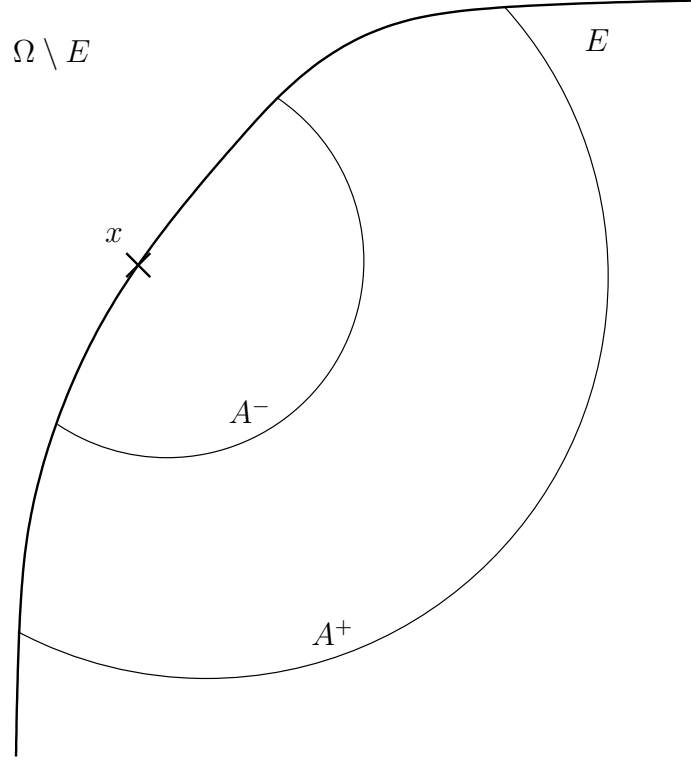


Figure 4.3: Illustration of the construction of the comparison set

Therefore we get the differential inequality,

$$\frac{d}{d\sigma} V(\sigma) \geq \frac{\gamma_n}{4} V(\sigma)^{\frac{n-1}{n}}, \quad (4.54)$$

where we used that due to the bound on ρ ,

$$V(\sigma) \leq \left(\frac{\gamma_n}{2(\|f\|_{L^\infty} + \frac{M}{\varepsilon^n})} \right)^n. \quad (4.55)$$

Integration of this equation yields

$$\int_{B_\rho(x)} \chi_E \geq \left(\frac{\gamma_n}{4n} \right)^n \rho^n, \quad (4.56)$$

which is the assertion with $\theta = \frac{1}{\omega_n} \left(\frac{\gamma_n}{4n} \right)^n = 1/4^n$. \square

Lemma 4.2.7 (Bound on the variation in time of $\chi_E^h(t)$). *There is a constant $C \in \mathbb{R}$, independent of h , such that the sets $E_k^h = E^h(kh)$, for $k \leq N$ satisfy*

$$\sum_{k=1}^N \int_{\Omega} |\chi_{E_k} - \chi_{E_{k-1}}| < C. \quad (4.57)$$

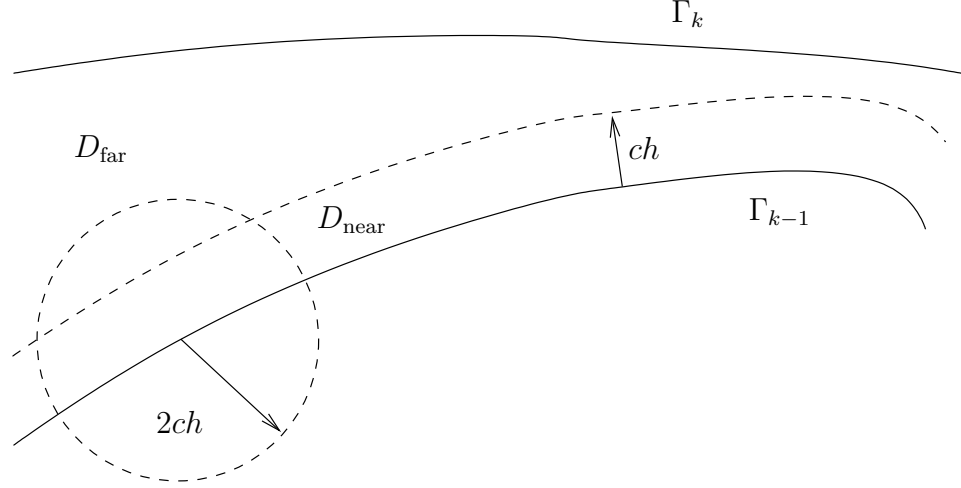


Figure 4.4: Illustration of Lemma 4.2.7

Proof. We will prove this relation for $E_k \setminus E_{k-1}$, the estimate for $E_{k-1} \setminus E_k$ follows by a similar procedure. The proof is illustrated in Figure 4.4.

First, we split the set

$$E_k \setminus E_{k-1} \subset \{x \in E_k \setminus E_{k-1} : \text{dist}(x, \partial E_{k-1}) > ch\} \cup \{x \in E_k \setminus E_{k-1} : \text{dist}(x, \partial E_{k-1}) \leq ch\} \quad (4.58)$$

$$=: D_{\text{far}} \cup D_{\text{near}}. \quad (4.59)$$

The constant c is chosen such that

$$c < \frac{\gamma_n}{2\omega_n^{1/n}} \frac{1}{\text{diam}(\Omega) + M}, \quad (4.60)$$

which means that the energy $\mathcal{F}^h(E, E_0)$ satisfies the conditions of the density estimate for balls of radius $2ch$.

For the first term in (4.59), we use the distance term in \mathcal{F} to obtain

$$|\{x \in E_k \setminus E_{k-1} : \text{dist}(x, \partial E_{k-1}) > ch\}| < \frac{1}{ch} \int_{E_k \Delta E_{k-1}} \text{dist}(x, \partial E_{k-1}) dx \quad (4.61)$$

$$\leq \frac{1}{c} \left(\int_{\Omega} |\nabla \chi_{E_{k-1}}| - \int_{\Omega} |\nabla \chi_{E_k}| + \mathcal{F}_{\text{elastic}}^{\varepsilon^{1/n}}(E_{k-1}) - \mathcal{F}_{\text{elastic}}^{\varepsilon^{1/n}}(E_k) \right). \quad (4.62)$$

The second set is estimated by means of the density lemma. We can cover it, up to a distance of $4ch$ to the boundary of Ω , with a family of balls $B \in \mathcal{B}$ with radius $\rho = 2ch$, all completely contained in Ω , with center $x \in \partial E_{k-1}$, such that the maximum number of balls containing one point is bounded by a constant $D(n)$. Employing the density lemma and an isoperimetric inequality

in the interior of a ball, we obtain

$$\int_B \chi_{E_k \setminus E_{k-1}} \leq \omega_n \rho^n \leq c\rho \int_B |\nabla \chi_{E_{k-1}}| \quad (4.63)$$

for each B . Summation over all $B \in \mathcal{B}$ and adding the boundary term yields

$$|\{x \in E_k \setminus E_{k-1} : \text{dist}(x, \partial E_{k-1}) \leq ch\}| \leq D(n)Cch \int_\Omega |\nabla \chi_{E_{k-1}}| + Ch. \quad (4.64)$$

From (4.62) and (4.64) we get

$$\begin{aligned} \sum_{k=1}^N \mathfrak{m}(E_k \setminus E_{k-1}) &\leq \sum_{k=1}^N \frac{1}{c} \left(\int_\Omega |\nabla \chi_{E_{k-1}}| - \int_\Omega |\nabla \chi_{E_k}| + \mathcal{F}_{\text{elastic}}^{\varepsilon^{1/n}}(E_{k-1}) - \mathcal{F}_{\text{elastic}}^{\varepsilon^{1/n}}(E_k) \right) \\ &\quad + \sum_{k=2}^N D(n)Cch \int_\Omega |\nabla \chi_{E_{k-1}}| + C + \mathfrak{m}(\Omega) \\ &< C. \end{aligned} \quad (4.65)$$

□

Proposition 4.2.8 (Compactness in time). *There exists $c > 0$, such that the discrete solution $E^h(t)$ satisfies*

$$\int_0^{T-\tau} \int_\Omega |\chi_{E^h(t+\tau)}(x) - \chi_{E^h(t)}(x)| \, dx dt < c\tau. \quad (4.66)$$

Proof. The left-hand side in the statement yields, in the total variation sense,

$$\begin{aligned} \int_0^{T-\tau} \int_\Omega |\chi_{E^h(t+\tau)}(x) - \chi_{E^h(t)}(x)| \, dx dt &\leq \int_0^{T-\tau} \int_\Omega \int_0^\tau |\partial_t \chi_{E^h(t+s)}| \, ds dx dt \\ &\leq \int_\Omega \int_0^\tau \sum_{k=1}^N |\chi_{E_k} - \chi_{E_{k-1}}| \, ds \\ &\leq C\tau. \end{aligned} \quad (4.67)$$

□

Convergence of the discrete solution The previous compactness considerations lead to the following:

Theorem 4.2.9 (Convergence). *The sequence $\chi_{E(t)}$ contains a converging subsequence with a limit function in*

$$L^1(\Omega \times [0, T]; \{0, 1\}). \quad (4.68)$$

Proof. Proposition 4.2.5 and Proposition 4.2.8 yield uniform equicontinuity in L^1 of the sequence. An application of the Arzela-Ascoli theorem yields strong convergence in L^1 , which proves the

result. □

4.2.5 Approximation of the original free discontinuity problem in the uniformly smooth case

For notational convenience we write the energy $\mathcal{F}^{h,\varepsilon}$ in this section as a function of the phase boundary Γ instead of the set E . The assumptions on regularity made below assert that the two can be used interchangeably. Consider again the minimizer for the energy in one step in the finite time discretization scheme

$$\mathcal{F}^{h,\varepsilon}(\Gamma) = \min_{u^\varepsilon \in H} \int_{\Omega} \frac{1}{2} |\nabla u^\varepsilon - \xi_E^\varepsilon|^2 + \int_{\Omega} |\nabla \chi_E| + \frac{1}{h} \int_{E \Delta E_0} \text{dist}(\cdot, \partial E_0), \quad (4.69)$$

where we assume the phase boundary $\Gamma = \partial E$ to be uniformly C^2 . In order to be a minimizer, it is necessary that the variation of this term with respect to a smooth perturbation of the phase boundary in the normal direction vanishes, i.e.

$$\text{variation}_{\Gamma} \mathcal{F}^{h,\varepsilon}(\Gamma) = 0. \quad (4.70)$$

We will now calculate the change of the three terms in the energy with respect to a small perturbation of Γ separately. To do this, we parametrize Γ as a curve $\Gamma = \{x \in \mathbb{R}^n, x = \gamma(t), t \in [0, 1]\}$. This curve is perturbed in the normal direction ν by a smooth function $\tilde{\gamma}$, such that the perturbed phase boundary $\tilde{\Gamma}$ is given by

$$\tilde{\Gamma} = \gamma(t) + s\tilde{\gamma}(t)\nu, \quad t \in [0, 1] \quad (4.71)$$

with magnitude of perturbation s . Now one can write the variation of $\mathcal{F}^{h,\varepsilon}$ in the direction of $\tilde{\gamma}$ as

$$\text{variation}_{\Gamma} \mathcal{F}^{h,\varepsilon}(\Gamma) = \left. \frac{d}{ds} \mathcal{F}^{h,\varepsilon}(\gamma + s\tilde{\gamma}\nu) \right|_{s=0}. \quad (4.72)$$

We will treat the three terms in the energy $\mathcal{F}^{h,\varepsilon}$ separately.

Elastic energy. First, consider the change of transformation strain under the perturbation described above. For the the new transformation strain we write $\tilde{\xi}_{E(s)}^\varepsilon$. We then can compute

$$\left. \frac{d}{ds} \tilde{\xi}_{E(s)}^\varepsilon \right|_{s=0} = \eta^\varepsilon * \llbracket \xi \rrbracket \tilde{\gamma} \delta_{\Gamma}, \quad (4.73)$$

which can be verified by multiplying with a smooth test function and integrating.

Since the inhomogeneity (the mollified transformation strain) in the elastic energy is smooth,

one can simply calculate its variation by partial differentiation. This yields

$$\frac{d}{ds} \int_{\Omega} \frac{1}{2} \left| \nabla u^\varepsilon - \tilde{\xi}_{E(s)}^\varepsilon \right|^2 \Big|_{s=0} = \int_{\Omega} \frac{1}{2} \frac{\partial}{\partial \nabla u} \left(\left| \nabla u^\varepsilon - \xi_{E(s)}^\varepsilon \right|^2 \right) \cdot \frac{\partial \nabla u}{\partial \xi_{E(s)}^\varepsilon} \frac{d\tilde{\xi}_{E(s)}^\varepsilon}{ds} \Big|_{s=0} \quad (4.74)$$

$$+ \int_{\Omega} \frac{1}{2} \frac{\partial}{\partial \xi_{E(s)}^\varepsilon} \left(\left| \nabla u^\varepsilon - \xi_{E(s)}^\varepsilon \right|^2 \right) \cdot \frac{d\tilde{\xi}_{E(s)}^\varepsilon}{ds} \Big|_{s=0}. \quad (4.75)$$

The first term vanishes, because u is assumed to minimize the energy for a given ξ_E^ε , therefore the variation with respect to ∇u is zero. For the second term we obtain

$$\text{variation}_{\Gamma} \mathcal{F}_{\text{elastic}}^\varepsilon = \int_{\Omega} (\nabla u - \tilde{\xi}_E^\varepsilon) \cdot (\eta^\varepsilon * \llbracket \xi \rrbracket \tilde{\gamma} \delta_{\Gamma}). \quad (4.76)$$

Surface energy. The variation of the surface energy with respect to the perturbation of the phase boundary yields the well-known surface energy term [40]

$$\text{variation}_{\Gamma} \int_{\Omega} |\nabla \chi_E| = \int_{\Gamma} \kappa \tilde{\gamma}. \quad (4.77)$$

Dissipation term. Since both the phase boundary Γ_0 of the previous time-step and the current phase boundary are assumed to be uniformly smooth, one can easily see that the variation of ‘distance’ term in the energy converges to the normal velocity, since

$$\frac{d}{ds} \frac{1}{h} \int_{E_0 \Delta E(s)} \text{dist}(\cdot, \partial E_0) \Big|_{s=0} = \frac{1}{h} \int_{\Gamma} \text{dist}(\cdot, \partial E_0) \tilde{\gamma} =: \int_{\Gamma} v_h \tilde{\gamma}. \quad (4.78)$$

The approximate normal velocity v_h converges, for uniformly smooth phase boundaries, to the normal velocity of the phase boundary, as $h \rightarrow 0$, since the distance to the set approximates the distance in the normal direction.

Convergence. Now, putting the three terms together, one can see that the minimizing set in one time-step satisfies

$$\int_{\Omega} (\nabla u - \tilde{\xi}_E^\varepsilon) \cdot (\eta^\varepsilon * \llbracket \xi \rrbracket \tilde{\gamma} \delta_{\Gamma}) + \int_{\Gamma} (\kappa + v_h) \tilde{\gamma} = 0. \quad (4.79)$$

Letting both ε and h go to zero, this yields (for smooth phase boundaries, and therefore piecewise smooth deformation), the original equation $v_n = f$, since

$$\int_{\Omega} (\nabla u - \tilde{\xi}_E^\varepsilon) \cdot (\eta^\varepsilon * \llbracket \xi \rrbracket \tilde{\gamma} \delta_{\Gamma}) \rightarrow \int_{\Gamma} \langle \nabla u - \xi_E \rangle \cdot \llbracket \xi \rrbracket = - \int_{\Gamma} (\llbracket W \rrbracket - \langle \sigma \rangle \llbracket \nabla u \rrbracket) \tilde{\gamma} \quad (4.80)$$

as $\varepsilon \rightarrow 0$.

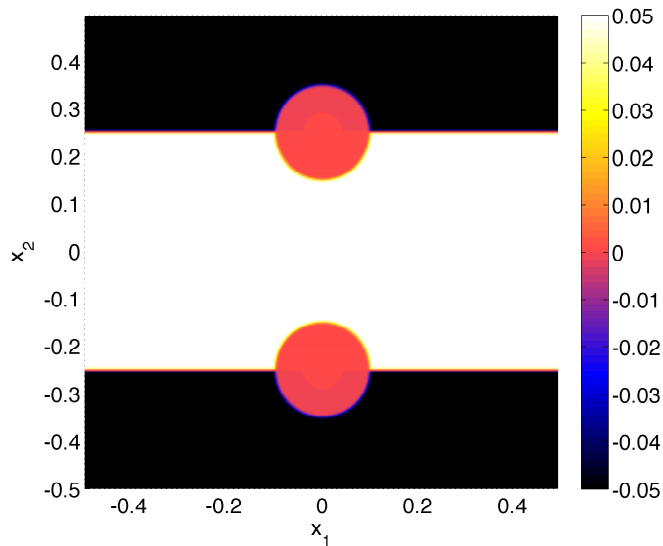


Figure 4.5: Initial configuration of the transformation strain

4.3 Numerical estimate of the critical depinning force

The particular choice of transformation strain $\xi_E(x)$ in Section 4.2, as illustrated in Figure 4.1, suggests that the interface should get pinned when traversing a domain that has inclusions of non-transforming material. Such precipitates of different structure do indeed exist in shape-memory alloys, however, the questions of whether they pose an obstacle to a propagating phase boundary and how strong such a pinning force would be are not trivial.

In an attempt to answer these questions a two-dimensional numerical simulation of the interface evolution in the model derived in this chapter has been developed in MATLAB. We choose the transformation strain to be $\xi^\pm = \pm(0, 0.05)^T$ and $\xi^A = 0$. On the domain Ω , one-periodic in both x_1 and x_2 , we place two inclusions at $x_1 = 0$ and $x_2 = \pm 0.25$. The inclusions occupy approximately three per cent of the area. For symmetry reasons it is clear that the situation depicted in Figure 4.5, where phase 1 is occupying the region $-0.25 \geq x_2 > 0.25$ is a stationary state if there is no force applied. Starting at this initial state, we evolve the interface according to a gradient flow with respect to the energy, under varying external applied forces, until either a steady state is reached or the interfaces escape from the inclusions.

The two phase boundaries in the simulation are described by cubic periodic B-splines, in the present case with 32 knots. According to the position of the phase boundary, the transformation strain $\xi_E(x)$ is generated on a 256×265 grid. As one can see in Figure 4.5, the phase boundary and also the boundaries of the inclusions are smoothed out slightly. A purely piecewise constant transformation strain would lead to artificial pinning of the interface. For each time-step, each of the nodes of the phase boundary-spline is varied slightly both up and down in the x_2 direction and

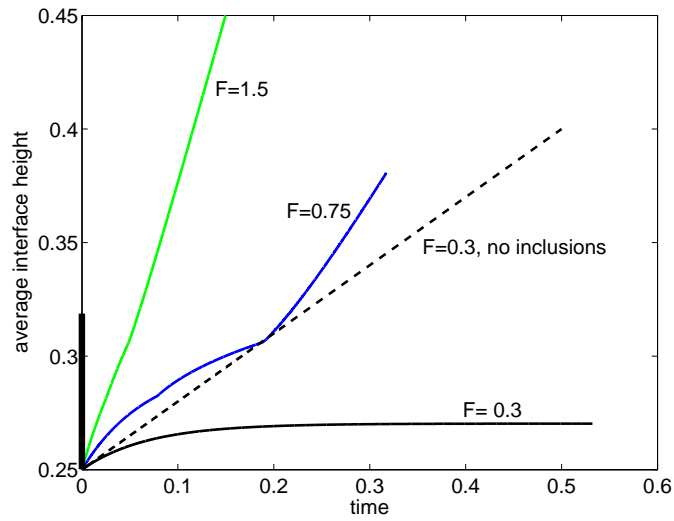
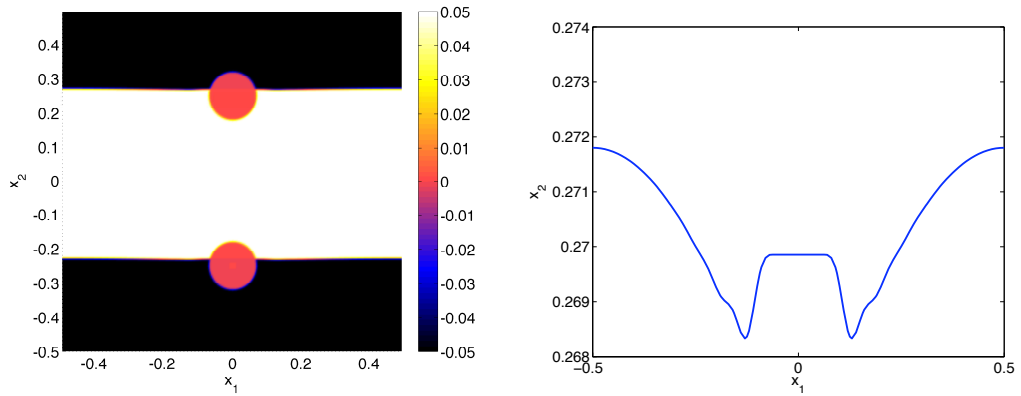


Figure 4.6: Evolution of the average height of the interfaces for different external loads. Shown is the evolution of the upper interface, starting at $x_2 = 0.25$; the other one, however, propagates exactly symmetrically. The amount the inclusion extends in the graph is illustrated by the black bar on the x_2 axis.



(a) Transformation strain corresponding to a stuck interface. The strong elastic forces keep the phase boundary nearly flat.

(b) One of the splines describing the interface in its stuck state

Figure 4.7: The stuck phase boundary

the energy change is recorded. The energies are calculated by solving the equilibrium equation for the displacement using Fourier transform. From there, one can calculate the driving force to be

$$\varphi = \frac{1}{2\Delta x_2}(E_{\text{down}} - E_{\text{up}}), \quad (4.81)$$

where Δx_2 is the amount the particular node has been varied and $E_{\text{up/down}}$ are the recorded energies, respectively. This generates a force for each node of the spline. To this force, we add a constant applied load F and evolve the nodes of the spline by a first-order explicit step in time. The part of the phase boundary that is inside the inclusions gets interpolated linearly, since no force acts on it. For this simulation, we do not consider the surface energy of the model, since we were only interested in the possibility of pinning through the configuration of the elastic material.

Figure 4.6 shows the evolution of the average height of phase boundaries for different applied loads. For $F = 1.5$ and $F = 0.75$ (non-dimensionalized units), the interface only gets slowed down slightly. For $F = 0.3$, we notice that the interface gets indeed stuck. For comparison, the evolution of the interface at $F = 0.3$ without any inclusions in the domain is also shown. The interface gets stuck in the configuration shown in Figure 4.7. The shape of the interface corresponds well with the driving force one would expect for an interface of such a shape. By starting the simulation with the two interfaces slightly displaced, it has also been verified that there is indeed an effect that pulls the interface back to the stuck state.

In order to give an estimate of the driving force necessary to release an interface from such an inclusion, one has to re-introduce physical units to the calculation. In this elastic case this is not hard. By merit of the scale invariance of linear elasticity the only relevant quantities are the volume fraction of the inclusions and the elastic modulus. If we assume an elastic modulus of 100 GPa, (in relation to the elastic modulus of the simulation, which was normalized to $1 \cdot 256^2$ non-dimensional units, due to the discretization) this leads to a critical pinning stress between 0.5 and 1 MPa. Compare to Figure 1.7.

4.4 Conclusions

In this chapter, a sharp interface model for the evolution of martensitic phase boundaries was presented. The existence of a solution that satisfies the kinetic relation $v_n = f$ in the smooth case was proved. This is, to our knowledge, the first dynamic sharp interface model for shape memory alloys, with full linearly elastic energy and a linear kinetic relation, that was shown to admit a solution. Furthermore, for a particular choice of inhomogeneity, the pinning of a martensite interface was demonstrated numerically. Despite the simplifying assumptions, the estimated critical stress is of the order of magnitude one would expect for such phase boundaries.

Chapter 5

Evolution in the shallow phase boundary approximation

In this chapter we consider the sharp interface model for the quasistatic evolution of a martensitic phase boundary under a series of simplifying assumptions. The phase boundary is treated as the graph of an evolving function, the elastic self energy stemming from the local misalignment of the phase boundary with respect to the stress-free flat configuration is linearized and the effect of precipitates is lumped together in a nonlinear local forcing term. The approximate model is derived in the first section. The second section shows results about the pinned and evolving states of the phase boundary. Some numerical results about the depinning transition are presented in Section 5.3.

5.1 Derivation of the approximate model

We study the model on a ‘strip,’ i.e., an $n - 1$ dimensional torus times the real line, $\Omega = T^{n-1} \times \mathbb{R}$ (see Figure 5.1). Consider again the elastic energy (4.2)

$$\mathcal{F}_{\text{elastic}} = \int_{\Omega} \frac{1}{2} |\nabla u - \xi_E|^2 dx \quad (5.1)$$

for an anti-plane shear deformation u defined on the strip as described above. The transformation strain ξ_E is again defined to be piecewise constant, and further assumed to have the following values

$$\xi_E(x) = \begin{cases} (0, 0, \dots, +1/2)^T & \text{for } x \in \Omega \setminus (E \cup A) \\ (0, 0, \dots, -1/2)^T & \text{for } x \in E \setminus A \\ (0, 0, \dots, 0)^T & \text{for } x \in A. \end{cases} \quad (5.2)$$

This specific choice of transformation strain has a jump discontinuity in the x_n direction. A different alignment is of course possible, however, the notation is greatly simplified if the normal of the discontinuity is aligned with a coordinate axis. Due to the linearity of the minimization problem for

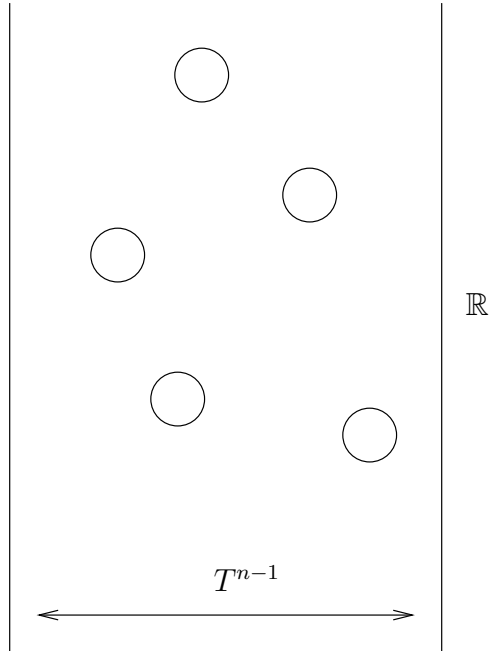


Figure 5.1: Phase boundary on a strip domain, with periodic boundary conditions in all dimensions except for one

u , one can decompose the deformation such that

$$u = u_1 + u_2, \quad (5.3)$$

solving respectively the equations

$$\Delta u_1 = \operatorname{div} \xi_1, \quad \nabla u_1 \rightarrow \xi_1 \text{ as } x_n \rightarrow \pm\infty \quad (5.4)$$

$$\Delta u_2 = \operatorname{div} \xi_2, \quad u_2 \text{ bounded as } x_n \rightarrow \pm\infty \quad (5.5)$$

$$(5.6)$$

for

$$\xi_1(x) = \begin{cases} (0, 0, \dots, +1/2)^T & \text{for } x \in \Omega \setminus E \\ (0, 0, \dots, -1/2)^T & \text{for } x \in E \end{cases} \quad (5.7)$$

and

$$\xi_2(x) = \begin{cases} -\xi_1(x) & \text{for } x \in A \\ (0, 0, \dots, 0)^T & \text{for } x \in \Omega \setminus A. \end{cases} \quad (5.8)$$

The elastic energy (4.2) can now be decomposed into the self energy of the interface Γ and the interaction of Γ with the stress field generated by the inclusions and the stress boundary conditions.

One obtains

$$\mathcal{F}_{\text{elastic}} = \int_{\Omega} \frac{1}{2} |\nabla u_1 + \nabla u_2 - \xi_1 - \xi_2|^2 dx \quad (5.9)$$

$$= \int_{\Omega} \frac{1}{2} |\nabla u_1 - \xi_1|^2 dx \quad (5.10)$$

$$+ \int_{\Omega} (\nabla u_1 - \xi_1, \nabla u_2 - \xi_2) dx \quad (5.11)$$

$$+ \int_{\Omega} \frac{1}{2} |\nabla u_2 - \xi_2|^2 dx. \quad (5.12)$$

The first integral (5.10) corresponds to the self energy of the martensitic phase boundary due to a possible misalignment of the normal of the phase boundary with respect to the jump in ξ_1 . This term vanishes for a flat phase boundary with normal $(0, 0, \dots, 1)^T$. The second and third term describe the interaction of the phase boundary with the inclusions. We will treat those two terms separately.

Approximation of the self-energy. We seek an approximation under the assumption that the phase boundary makes small deviations from a flat one with normal $(0, 0, \dots, 1)^T$. To this end, we will first assume that the phase boundary is the graph of a function g , i.e.,

$$\Gamma = \{(x_1, x_2, \dots, x_n) \text{ such that } x_n = g(x_1, \dots, x_{n-1})\}. \quad (5.13)$$

As described in [66], one can now write the solution to equation (5.4) as the convolution integral along the phase boundary of the Green's function and the inner product of the phase boundary normal and the jump in transformation strain, so that

$$u = G * [[\xi_E]] \cdot \nu dy_{\Gamma}. \quad (5.14)$$

The phase boundary normal ν is given by

$$\nu = \begin{pmatrix} -g_{,1} \\ -g_{,2} \\ \vdots \\ 1 \end{pmatrix} \cdot \frac{1}{\sqrt{g_{,1}^2 + g_{,2}^2 + \dots + 1}}, \quad (5.15)$$

the surface element of the integration however is

$$dy_{\Gamma} = \sqrt{g_{,1}^2 + g_{,2}^2 + \dots + 1}. \quad (5.16)$$

Therefore, one obtains

$$u_1 = \int_{T^n} G \begin{pmatrix} x_1 - y_1 \\ x_2 - y_2 \\ \vdots \\ x_n - g(y_1, y_2, \dots) \end{pmatrix} (\xi_2 - \xi_1) \cdot \begin{pmatrix} -g_{,1} \\ -g_{,2} \\ \vdots \\ 1 \end{pmatrix} dy. \quad (5.17)$$

We now make the assumption that the phase boundary is shallow, i.e.,

$$g(x') = g_0 + g_1(x') \quad (5.18)$$

where g_1 is a small deviation from the average, and that one can expand the integral in equation (5.17). This yields

$$u_1(x) = \int_{T^n} G \begin{pmatrix} x_1 - y_1 \\ x_2 - y_2 \\ \vdots \\ x_n - g_0 \end{pmatrix} dy \quad (5.19)$$

$$+ \int_{T^n} g_1(y_1, \dots, y_{n-1}) G_{x_n} \begin{pmatrix} x_1 - y_1 \\ x_2 - y_2 \\ \vdots \\ x_n - g_0 \end{pmatrix} dy \quad (5.20)$$

$$+ \text{higher order terms.} \quad (5.21)$$

The first term (5.19) just produces the deformation induced by a correctly aligned, perfectly flat phase boundary. This has zero elastic energy. The second term, however, is the elastic deformation of a dislocation line of magnitude g [49]. It is well known that the elastic energy of such a dislocation line is exactly the $H^{1/2}$ norm of the magnitude of the dislocation [37].

$$\mathcal{F} = \frac{1}{4} [g]_{H^{1/2}}^2 = \sum_{k=1}^{\infty} k \hat{g}(k). \quad (5.22)$$

This will be the elastic “self-energy” of the phase boundary for our model.

The interaction energy. We also simplify the driving force that originates from the interaction energy of the phase boundary with the inclusions. While this force in fact depends nonlocally on the function g describing the phase boundary, we will assume for simplicity that it can be modeled

by a function

$$\varphi: \Omega \rightarrow \mathbb{R}, \quad (5.23)$$

such that $\varphi(x_1, x_2, \dots, x_n) = \varphi(x_1, x_2, x_n + 1)$ and also $\int_{T^n \times [0,1]} \varphi = 0$. This means that there is a local periodic force distribution with vanishing average depending on the location of the phase boundary. Furthermore, we add a constant force F , from the application of a stress boundary condition, so that

$$f = \varphi + F. \quad (5.24)$$

Summary of the approximate model. Combining equations (5.22) and (5.24), and assuming a gradient flow in the L^2 norm of g with respect to the energy, we end up with the evolution equation for the phase boundary (after absorbing a factor of $1/2$ into the forcing f and renormalizing the mobility of the interface)

$$g_t = \delta_g \frac{1}{2} [g]_{H^{1/2}}^2 + f(x_1, \dots, x_{n-1}, g(x_1, \dots, x_{n-1})). \quad (5.25)$$

This equation may be compactly written by its Fourier transform,

$$\hat{g}_t(k) = -k\hat{g} + \hat{f}, \quad (5.26)$$

since the operator stemming from the $H^{1/2}$ norm term then becomes local. Note that the equation is still nonlinear, since the driving force f depends on g . In the next section we will study the stick-slip behavior of equation (5.26).

5.2 Stick-slip behavior

The main assertions in this section are similar to [28]. We extend their results from the line-tension energy to a nonlocal energy modeling elastic interaction.

Denote by x' the vector $(x_1, \dots, x_{n-1})^T$. We make, from now on, the following assumptions on the force distribution φ :

1. Definition: $\varphi: T^{n-1} \times \mathbb{R} \rightarrow \mathbb{R}$,
2. Periodicity: $\varphi(x', y) = \varphi(x', y + 1)$,
3. Vanishing average: $\int_{T^{n-1} \times [0,1]} \varphi(x', y) = 0$,
4. Smoothness: $\varphi \in C^1(T^{n-1} \times \mathbb{R})$,

and write $\varphi_g(x')$ for $\varphi(x', g(x'))$ as well as $f_g(x')$ for the term $\varphi(x', g(x')) + F$.

First we assert the existence of a stationary solution for zero external driving force.

Proposition 5.2.1. *The equation*

$$0 = k\hat{g}(k) + \hat{\varphi}_g \quad (5.27)$$

admits a solution.

Proof. Consider the sequence $\{\hat{g}_j(k)\}_{j=1}^\infty$, so that $\hat{g}_j(0) = c$ for some constant $c \in \mathbb{R}$ and all $j \geq 1$. The other Fourier coefficients in the sequence are determined by the iterative scheme

$$\hat{g}_{j+1}(k) = \frac{\hat{\varphi}_g(k)}{k}, \quad (5.28)$$

anchored by $\hat{g}_1(k) = 0$. By the boundedness of φ_g independent of g , we have

$$\|g_j\|_{H^1}^2 = \sum_{k=0}^{\infty} k^2 |\hat{g}_j(k)|^2 \quad (5.29)$$

$$= c + \sum_{k=1}^{\infty} k^2 \frac{|\hat{\varphi}_g(k)|^2}{k^2} \quad (5.30)$$

$$= c + \sum_{k=1}^{\infty} |\hat{\varphi}_g(k)|^2 \leq c + \max(\varphi)^2. \quad (5.31)$$

The sequence is thus bounded in H^1 , and one can extract a weakly converging subsequence. Denote the limit, depending on c , by g_c . For $k \geq 1$, g_c satisfies

$$k\hat{g}_c(k) = \hat{\varphi}_{g_c}(k). \quad (5.32)$$

Now, continuing as in [28], Proposition 4, denote by

$$G(c) := \frac{1}{2} [g_c]_{H^{1/2}}^2 - \int_{T^{n-1}} \int_0^{g_c(x')} \varphi(x', g) \, dg dx' \quad (5.33)$$

the energy depending on the fixed average c . Since f has zero average, we have $G(c+1) = G(c)$, furthermore, G is a Lipschitz function. Therefore, G admits a minimum for some $c_0 \in \mathbb{R}$. The function g_{c_0} solves

$$0 = \frac{\partial}{\partial c_0} G(c_0) = \hat{\varphi}_{g_{c_0}}(0). \quad (5.34)$$

This shows that g_{c_0} is a solution to 5.27. \square

The following theorem asserts the existence of a threshold force, up to which—but not above which—a stationary solution exists.

Theorem 5.2.2 (Existence of a threshold force). *There exists an $F^* \geq 0$ such that the equation*

$$0 = k\hat{g}(k) + \hat{\varphi}_g(k) + F = k\hat{g}(k) + \hat{f}_g(k) \quad (5.35)$$

has a solution for all $F \leq F^*$, while it has no solution for $F > F^*$.

Proof. Consider $\Phi = \{F \geq 0 \text{ such that (5.35) has a solution}\}$. Clearly, because of Proposition 5.2.1, $\Phi \neq \emptyset$. Also, if $F > \sup \varphi$, then (5.35) has no solution. Define, therefore, $F^* = \sup\{\Phi\} < \infty$. Two things remain to be shown in order to establish the result:

i) $F^* \in \Phi$.

ii) There is a solution to (5.35) for all $F < F^*$.

Proof of i): Consider a sequence $F_n \rightarrow F^*$ where corresponding solutions g_n to (5.35) exist. There has to be such a sequence, otherwise F^* could not be the supremum of Φ . Since $\{F_n\}$ is uniformly bounded, Proposition 5.2.1 asserts weak compactness of $\{g_n\}$ in H^1 . Therefore, there is a weakly converging subsequence whose limit satisfies

$$0 = k\hat{g}(k) + \hat{\varphi}_g(k) + F^*. \quad (5.36)$$

Proof of ii): Consider $0 < F < F^*$, and the solutions g^* and g_0 to the stationary equation with external driving force F^* and 0, respectively. By the periodicity of φ , and the continuity of the solutions we can assume $g^* > g_0$. These solutions are also super- and subsolutions to (5.35), respectively. Therefore, there exists a solution to (5.35). \square

The next proposition shows the existence of a solution to the quasistatic evolution problem and asserts its regularity.

Proposition 5.2.3 (Existence and regularity). *Given $T > 0$ and an initial condition $g_0 \in L^2(T^{n-1})$, there exists a unique solution $g(t)$ to the problem*

$$\hat{g}_t(t, k) = -k\hat{g}(t, k) + \hat{f}_{g(t)} \quad \text{on } T^{n-1} \times [0, T] \quad (5.37)$$

$$f_g = \varphi_g + F, \quad (5.38)$$

$$\hat{g}(0, k) = \hat{g}_0(k). \quad (5.39)$$

Furthermore, there exists a constant C depending only on c and f , such that

$$[g(t)]_{H^1} < C_1 e^{-t} \|g_0\|_{L^2} + C_2 \quad \text{for } t \in [c, T], \quad (5.40)$$

i.e., the H^1 semi-norm, which is the H^1 norm of $g - fg$ is uniformly bounded.

Proof. The existence follows directly from the fact that the linear operator in the equation generates a unique semigroup, since it is dissipative (it is, in fact the variation of an energy), and that the nonlinear forcing is Lipschitz.

To show the regularity of the $g(t)$, first note that the solution to (5.37) satisfies

$$\hat{g}(t, k) = e^{-kt} g_0 + \int_0^t e^{-k(t-s)} \hat{f}_{g(s,k)}(k) \, ds. \quad (5.41)$$

Assume now that $t > 1$. We have

$$[g(t, k)]_{H^{1/2}}^2 = \sum_{k=1}^{\infty} k |\hat{g}(t, k)|^2 \quad (5.42)$$

$$= \sum_{k=1}^{\infty} k \left| e^{-kt} \hat{g}_0(k) + \int_0^t e^{-k(t-s)} \hat{f}_{g(s,k)}(k) \, ds \right|^2 \quad (5.43)$$

$$\leq \sum_{k=1}^{\infty} k |e^{-kt} \hat{g}_0(k)|^2 + \sum_{k=1}^{\infty} k \left| \int_0^{t-1} e^{-k(t-s)} \hat{f}_{g(s,k)}(k) \, ds \right|^2 \quad (5.44)$$

$$+ \sum_{k=1}^{\infty} k \left| \int_{t-1}^t e^{-k(t-s)} \hat{f}_{g(s,k)}(k) \, ds \right|^2 \quad (5.45)$$

$$\leq C_1 e^{-t} \|g_0\|_{L^2} + C \quad (5.46)$$

$$+ \sum_{k=1}^{\infty} k \left| \sqrt{\int_{t-1}^t e^{-2k(t-s)} \, ds} \sqrt{\int_{t-1}^t |\hat{f}_{g(s,k)}(k)|^2 \, ds} \right|^2 \quad (5.47)$$

$$\leq C_1 e^{-t} \|g_0\|_{L^2} + C \quad (5.48)$$

$$+ C' \sum_{k=1}^{\infty} \int_{t-1}^t |\hat{f}_{g(s,k)}(k)|^2 \, ds \quad (5.49)$$

$$\leq C_1 e^{-t} \|g_0\|_{L^2} + C_2. \quad (5.50)$$

Here, we have used Hölder's inequality in the fifth line and the fact that $\int_{t-1}^t e^{-k(t-s)} \, ds = \frac{1-e^{-k}}{k}$ thereafter. Therefore, $[g(\tau)]_{H^{1/2}}$ is uniformly bounded in the sense of Proposition 5.2.3 for $1 + (t-1)/2 < \tau < t$. To gain higher regularity, first note that for τ as before, one has that $\|f_{g(\tau)}\|_{H^{1/2}}$ is also bounded uniformly, due to the smoothness of f as a function of g . This, however, means that

$$\sqrt{k} |\hat{f}_{g(\tau)}| < C. \quad (5.51)$$

For simplicity, we will drop the dependence of g_0 and t in the notation. Now, one can redo the

calculation as above, however with a different use of Hölder's inequality. This yields

$$[g(t, k)]_{H^{(1+\alpha)/2}}^2 = \sum_{k=1}^{\infty} k^{1+\alpha} |\hat{g}(t, k)|^2 \quad (5.52)$$

$$\leq C_1 e^{-t} \|g_0\|_{L^2} + C \quad (5.53)$$

$$+ \sum_{k=1}^{\infty} k^{1+\alpha} \left| \left(\int_{t-1}^t e^{-\frac{4}{3}k(t-s)} ds \right)^{3/4} \left(\int_{t-1}^t |\hat{f}_{g(s,k)}(k)|^4 ds \right)^{1/4} \right|^2 \quad (5.54)$$

$$\leq C_1 e^{-t} \|g_0\|_{L^2} + C \quad (5.55)$$

$$+ \sum_{k=1}^{\infty} k^{1+\alpha} k^{-1-1/2} k^{-1} \left| \left(\int_{t-1}^t |\sqrt{k} \hat{f}_{g(s,k)}(k)|^4 ds \right)^{1/4} \right|^2 \quad (5.56)$$

$$\leq C_1 e^{-t} \|g_0\|_{L^2} + C \quad (5.57)$$

$$+ \sum_{k=1}^{\infty} k^{1+\alpha} k^{-1-1/2} k^{-1} \left| \left(\int_{t-1}^t C^4 ds \right)^{1/4} \right|^2. \quad (5.58)$$

This converges, for example, for $\alpha = 1/4$, and we have

$$[g(t, k)]_{H^{5/8}} \leq C. \quad (5.59)$$

This process can be iterated, since now one has $k^{5/8} |\hat{f}_{g(\tau)}| < C$, until one reaches the desired regularity. If $t < 1$, then one can simply leave out the term with integration bounds 0 and $t - 1$ and obtain the same result. \square

The next theorem proves the existence of a space-time periodic solution to (5.37) above the critical force.

Theorem 5.2.4 (Existence of a space-time periodic solution). *For each $F > F^*$, there exists $0 < T(F) < \infty$ and a function $g_F(x, t)$ satisfying (5.37) such that*

$$g(x, t + T) = g(x, t) + 1. \quad (5.60)$$

Proof. Proposition 5.2.3 proves global existence of a solution. We will split the solution up into the evolution of the average and the evolution of the deviation of the average and use Schauder's fix point theorem to prove the existence of a solution satisfying (5.60).

Consider $g(x, t)$, the solution from Proposition 5.2.3, and define $p(t) = \int f_g(x, t) dx$ and $\xi(x, t) = g(x, t) - p(t)$. The functions p and ξ then satisfy

$$\dot{p} = \int f_g(x, t) dx, \quad (5.61)$$

$$\hat{\xi}_t(k) = -k\hat{g}(k) + \hat{f}_g(k) \quad \text{for } k \geq 1. \quad (5.62)$$

Consider the initial condition $\xi(x, 0) = \xi_0(x) \in L^2$, and $p(0) = 0$. Since $F > F^*$, no stationary solution exists. Therefore, there is $T(\xi_0) > 0$, such that $p(T(\xi_0)) = p(0) + 1$, and a constant τ , independent of ξ_0 , such that $T(\xi_0) > \tau$. This follows from the fact that $|\dot{p}| \leq \|f\|_{L^\infty}$. We also have $T(\xi_0) < \infty$, since otherwise one could find a stationary solution to the problem.

Now consider the nonlinear operator that advances the solution ξ in time, such that

$$\mathcal{T}(\xi_0) = \xi(\cdot, T(\xi_0)), \quad (5.63)$$

and we have

$$\hat{\xi}(T, k) = e^{-kT} \xi_0(k) + \int_0^T e^{-k(t-s)} \hat{f}_{g(s)}(k) ds \quad k \geq 1. \quad (5.64)$$

A simple calculation shows that $\|\xi(T)\|_{L^2} < e^{-\tau} \|\xi_0\|_{L^2} + C$, therefore, for $A = C/(1 - e^{-\tau})$, this operator maps the set $\|\xi_0\|_{L^2} < A$ onto itself. The regularity estimate shows that $\xi(T)$ is bounded in H^1 independent of ξ_0 . The operator \mathcal{T} is thus compact and an application of Schauder's fix point theorem yields the existence of a time-space periodic solution. \square

This space-time periodic solution is in fact unique, as shown by the following proposition.

Proposition 5.2.5 (Uniqueness of the space-time periodic solution). *The time-period T for solution to (5.37) satisfying*

$$g(x, t + T) = g(x, t) + 1 \quad (5.65)$$

is unique. Also, the solution itself is unique up to a time-shift so that, given two solutions g_1 and g_2 there exists t_0 such that $g_1(x, t) = g_2(x, t + t_0)$.

Proof. First, note that continuous solutions to equation (5.37) satisfy a comparison principle, i.e., if $g_1(\cdot, t_0) \leq g_2(\cdot, t_0)$ for some t_0 , then this relation has to hold for all times. To see this, note that if for some time t_1 , the relation would have to be violated, the two solutions would first have to touch at some point x_0 . At this point, the nonlinear forcing satisfies $f_{g_1}(x_0) = f_{g_2}(x_0)$. The linear non-local terms, however, in real space read

$$\int_{\mathbb{R}^{n-1}} \frac{g_{1,2}(x_0)}{|x_0 - y|^2} dy, \quad (5.66)$$

where the functions $g_{1,2}$ are periodically extended from T^{n-1} . Since, at this point in time, however, we still have $g_1(\cdot, t_0) \leq g_2(\cdot, t_0)$, it is clear that this relation also holds for the total force. The two solutions therefore can never cross each other. A strict version of the comparison principle also applies.

Assume now that there exist two space-time periodic solutions g_1 and g_2 , with time constants $0 < T_2 < T_1 < \infty$. Since the solutions are continuous and invariant under translations by an integer,

Number of Fourier coefficients	1024
Length over which the interface velocity is averaged	4
Initial upper bound for F^* in bisection	0.5
Initial lower bound for F^* in bisection	0
Threshold for accuracy of F^*	$2 \cdot 10^{-9}$
Coefficient of elastic force	0.1
Time step	$1 \cdot 10^{-3}$
Threshold for stuck interface	$1 \cdot 10^{-14}$

Table 5.1: Parameters used for the numerical examination of the depinning transition

one can find $N \in \mathbb{N}$ such that, for some time t_0 , one has $g_1(\cdot, t_0) \leq g_2(\cdot, t_0) + N$. But since $T_2 < T_1$ there exists a time T after which the two solutions would have passed each other, contradicting the comparison principle.

Now, consider a solution G_1 with the initial condition $g_1(\cdot, t_0)$ and a solution G_2 with initial condition $g_2(\cdot, t_0)$. There have to exist a time T , an integer N , and a point x_0 such that we have

$$G_1(x_0, T) = G_2(x_0, 0) + N \quad \text{and} \quad G_1(\cdot, T) \leq G_2(\cdot, 0) + N, \quad (5.67)$$

i.e., the solutions have to touch at some time. Evolving both solutions in time from there on, one can see that they touch again after one time period. This, however, again contradicts the comparison principle, unless $G_1(\cdot, T + t) = G_2(\cdot, t)$. \square

5.3 Numerical examination of the depinning transition

In [28] it is proved that the depinning transition of a parabolic system exhibits a power law behavior in the sense that, close to the critical driving force, the average velocity $\bar{v} = 1/T$ of the unique space-time periodic solution is given by

$$\bar{v} \approx C \cdot \sqrt{F - F^*}, \quad (5.68)$$

where C depends on the local forcing φ . In order to study this behavior in our nonlocal elasticity setting, a series of numerical simulations were conducted on a 2d periodic domain to examine the depinning behavior. The results show good agreement with a square-root power law behavior. It is important to note that the depinning behavior depends very sensitively on the discretization of the pinning force. In [28], the power law behavior is only proved if $\varphi \in C^2$. In fact, for a piecewise linear or piecewise constant approximation of the local pinning force, we do not see the same behavior.

Size of pinning sites	Critical applied force F^*
1/8	0.0204
1/16	0.0307
1/32	0.0150
1/64	0.0143
1/128	0.0119

Table 5.2: Dependence of the critical applied force on the size of the pinning sites

5.3.1 The numerical method

Starting with an initial configuration $g(0) = 0$ and a fixed applied load F , we numerically integrate equation (5.37) using an explicit first-order Euler scheme. The elastic force is calculated using Fourier transforms. The local pinning force is constructed using a cubic B-spline. Once the interface has traveled a certain length on average (and never got stuck on the way), the final time is recorded. This way, a relation between the average velocity \bar{v} and F is obtained. The interface is considered stuck if the L^2 norm of the driving force f drops below a certain threshold. This ‘inner loop’ is repeated with F chosen each time through a bisection algorithm, thus giving new upper and lower bounds for the critical F^* at each run. The program terminates after a certain accuracy for determining F^* has been reached. In Table 5.1 the standard parameters for the simulation can be found.

5.3.2 Simulations

Experiment 1: General depinning behavior. As a standard example, we use a local driving force $\varphi(x_1, x_2) = \frac{\partial}{\partial x_2} \Phi(x_1, x_2)$, where Φ is a potential that has smooth dips of a fixed depth and radius at random points. We approximate φ by a cubic C^2 spline curve. The exact force used in this simulation is depicted in Figure 5.2(a). The constants used for this simulation are shown in Table 5.1. The evolution of the interface through one period is shown in Figure 5.2(b), where one can see that the interface spends most of its time near the critical stuck state depicted in Figure 5.2(c). In Figure 5.2(d), the relation between the average velocity, compared to a square-root power law is shown. The fit over almost three decades is excellent and at the very high end of the applied force one can see that the velocity turns toward a linear dependence on the applied force, as expected. The slight deviation from the power-law at the very low end of the applied force that can be seen in this experiment as well as in the others stems from the fact that the accuracy to which the critical force is determined is not significantly above the additional applied force there.

Experiment 2: Comparison of the depinning behavior for different sizes of pinning sites

For this experiment, we use five different sizes pinning sites, yielding the force distribution as depicted in Figure 5.3. All other parameters are kept as in Experiment 1. The dependence of the critical external force F^* is shown in Table 5.2. The depinning behavior is shown in

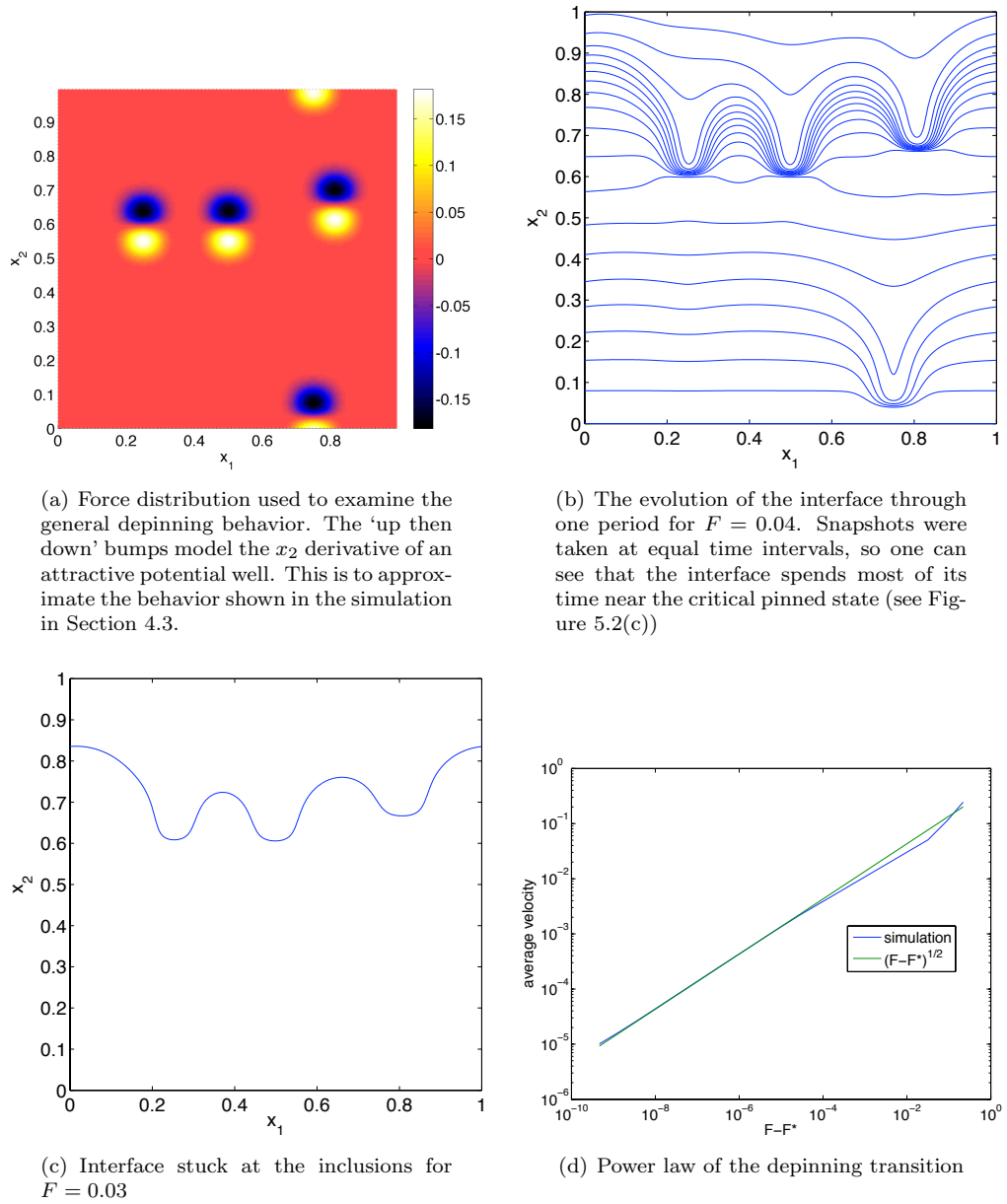


Figure 5.2: Experiment 1, the general depinning behavior

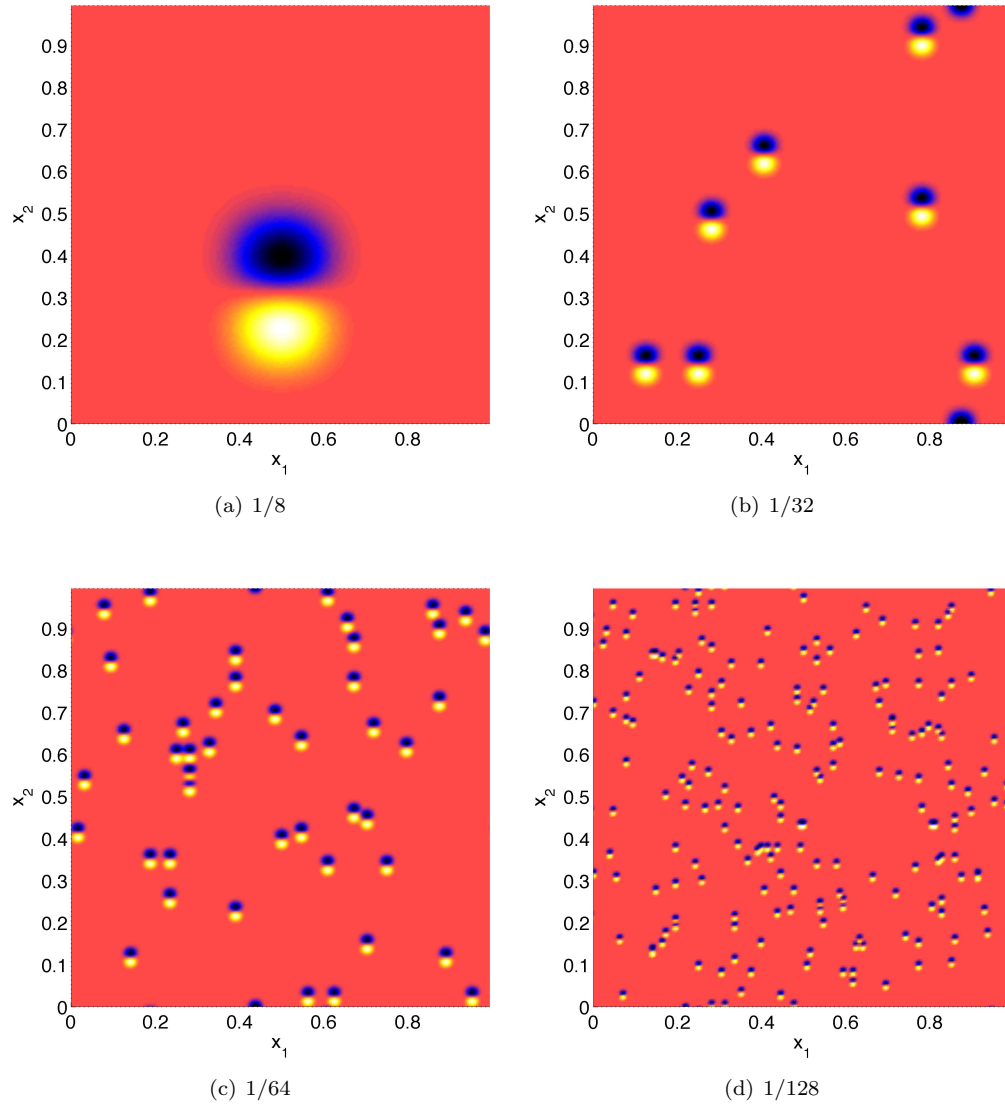


Figure 5.3: The local pinning forces used in Experiment 2. The maximum and minimum force are the same for all simulations, the grid on which the spline is discretized, however, is of the indicated size. Pinning sites are then distributed randomly with constant probability of occurrence. The pinning force for discretization size can be found in Figure 5.2(a), where also a relation between the color and the magnitude of the force is given.

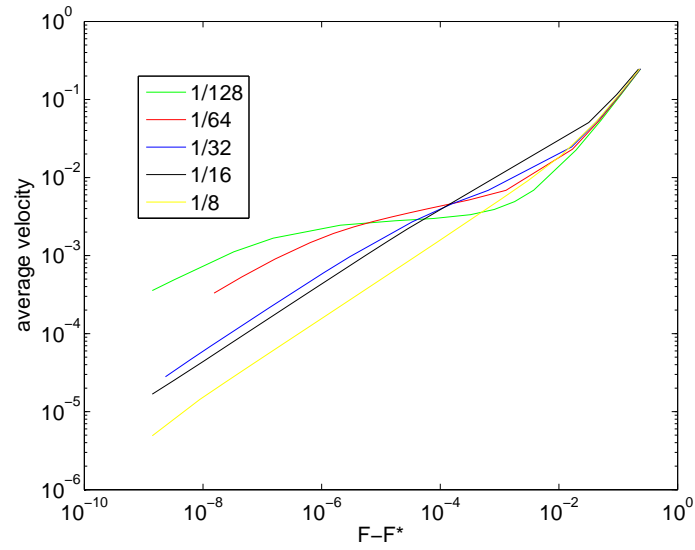
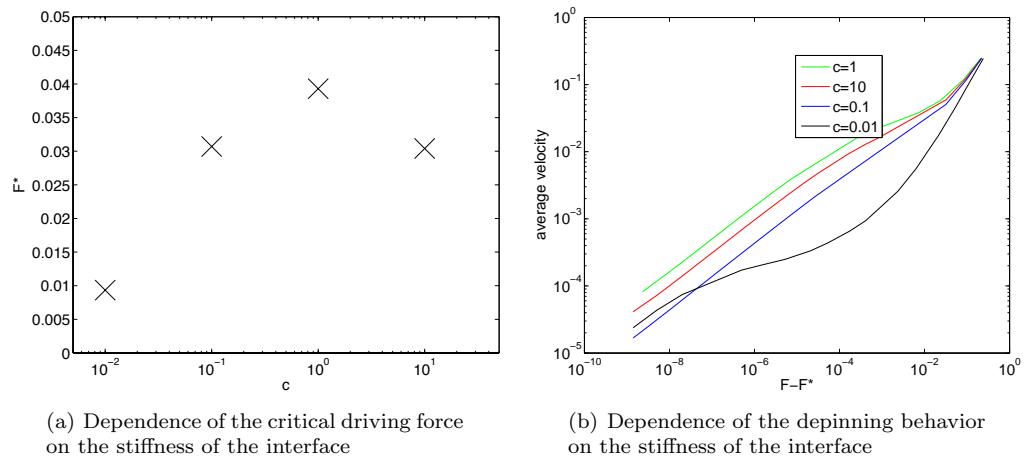


Figure 5.4: The depinning behavior for different sizes of pinning sites. One can see that the onset square root power law behavior is pushed towards lower applied forces for smaller (and therefore sharper) pinning sites.



(a) Dependence of the critical driving force on the stiffness of the interface

(b) Dependence of the depinning behavior on the stiffness of the interface

Figure 5.5: Experiment 3

Figure 5.4. For the simulations with smaller inclusion sizes, the depinning behavior seems to deviate slightly from a square-root power law. This is due to the fact that these smaller inclusions have sharper gradients so that the discretization error is larger.

Experiment 3: Comparison of F^* for interfaces of varying stiffness. The simulation was conducted with the same potential as in Figure 5.2(a), but the constant c of attenuation is varied. The other parameters are the same as in Experiment 1, except for the time step Δt , which had to be reduced to $2 \cdot 10^{-4}$ at $c = 10$ in order to keep the explicit time integration stable. Figure 5.5(a) shows the dependence of the critical driving force F^* on the stiffness of the interface for the given potential. In any case, the transition still follows the same power law, as seen in Figure 5.5(b).

5.4 Conclusions

We have studied a shallow phase boundary approximation of the model developed in Chapter 4. The existence of a threshold force and a time-space periodic solution evolving with an average velocity have been shown for this approximation. Furthermore, we see a clear square-root power-law depinning behavior in numerical experiments. This strongly suggests the conjecture that such a depinning behavior is in fact universal for a smooth local driving force in a periodic domain in the elastic case.

Chapter 6

Final remarks and future directions

Two main aspects of martensitic phase boundaries were studied in the present thesis. First, in a computational analysis, the details of thin films of shape memory alloys as they deform into tent-like structures were examined. We used subdivision surfaces, previously suggested for the study of shell structures, to accurately resolve the regions of high deformation gradient. It was shown that it is feasible to use such a generalized spline in order to build a conforming discretization for phase transformation models including higher-order gradient terms. The tent-like structures that were modeled in this simulation are of potential interest for use as actuators for micro electro-mechanical systems (MEMS). With some analytical calculations, we confirmed results of the complexity of the phase boundary structure at the tip of such tents. Further examinations include the effects of a misalignment of the crystal directions with the prescribed boundary conditions as well as non-square domains.

The results make it clear that a local adaptive refinement of the discretization would be an interesting extension of the work. Using the method of CHARMS as developed in [38], adaptive refinement becomes feasible for H^2 discretizations necessary for models including strain gradient terms.

The second aspect examined in this thesis is the evolution of martensitic phase boundaries in heterogeneous media and the emergence of rate-independent hystereses therefrom. First, a sharp interface model for phase boundary evolution was developed. The model included a full non-local elasticity term as well as a surface energy penalizing the length of the phase boundary. A proof of existence of a solution for such a model was presented. To our knowledge, this is the first sharp interface evolution model for martensitic phase transformations that takes the full nonlocal elastic forces into account for which the existence of a solution could be proved. In order to study the emergence of a stick-slip behavior by homogenizing a linear kinetic relation for the evolution of a phase boundary in the presence of non-transforming precipitates, a numerical simulation using the sharp interface model was developed. The results show the existence of a critical stress below which the interface remains pinned by an inclusion. Above the critical stress, the phase boundary is almost

unhampered by the precipitate.

The most natural extension of the existence result for the full sharp interface model is to the case of no surface energy. This regularizing term, however, is critical in our analysis, which uses many results from the theory of functions of bounded variation. Relying on the elastic forces alone for regularization would require lower bounds on the elastic energy depending on the shape of the interface. These lower bounds are unfortunately difficult to obtain, since there are many highly irregular interfaces with very small elastic energy. Of course, proving the existence of a stick-slip behavior is another point that remains to be examined. In order to do this, one would first need to show existence of solutions on an infinite, strip-like domain. Then, sharpened bounds on the perimeter could lead to the necessary compactness for the existence of time-space periodic solutions.

For an approximate model assuming an almost flat phase boundary, the existence of such a critical stress was proved rigorously in the present thesis. In this approximation, numerical simulations show a power law depinning behavior with a critical exponent of $1/2$. A proof for such a behavior is still missing, but could possibly be within reach through similar methods as in [28]. The extension of such methods to non-periodic random settings more commonly investigated by physicists is also an interesting direction.

Appendix A

Derivation of the thin film model

Our starting point is a one-director Cosserat model of thin films which was shown by Bhattacharya and James [15] to be the rigorous asymptotic (Γ) limit of a three-dimensional theory of martensitic phase transformation. Consider film with lateral extent $\Omega \subset \mathbb{R}^2$ and thickness h in the reference configuration. Let $y : \Omega \rightarrow \mathbb{R}^3$ describe the deformation of the mid-surface and $b : \Omega \rightarrow \mathbb{R}^3$ be the director that describes the deformation of the thickness. The energy (per unit thickness) of the film is given by

$$\int_{\Omega} \{ \kappa (|\nabla^2 y|^2 + 2|\nabla b|^2) + \varphi(\nabla y|b) \} dx \quad (\text{A.1})$$

where the first term (with co-efficient κ) describes the interfacial or exchange energy while the second is the stored energy. φ is the bulk or three-dimensional stored energy density and it is evaluated at the 3×3 matrix constructed as follows: the first two columns are the partial derivatives of y with respect to the planar co-ordinates while the third is the vector b .

If we impose natural boundary conditions on b , then it is minimized at uniform/constant fields. Thus, the problem above becomes one of minimizing

$$\int_{\Omega} \{ \kappa |\nabla^2 y|^2 + W(\nabla y) \} dx \quad (\text{A.2})$$

over all y subject to appropriate boundary conditions where

$$W(F) = \min_b \varphi(F|b) . \quad (\text{A.3})$$

If W_0 is some characteristic scale of energy density, then

$$\lambda = \sqrt{\frac{\kappa}{W_0}} \quad (\text{A.4})$$

is a characteristic length-scale. Indeed, if we choose W_0 to be the barrier-height between the wells normalized by the transformation strain, then λ determines the length-scale on which the equilibrium

solutions transition from one well to another. Therefore it is natural to write the problem in non-dimensional quantities using λ and W_0 :

$$x \mapsto \lambda x, \quad y \mapsto \lambda y, \quad \Omega \mapsto \lambda \Omega, \quad W \mapsto W_0 W . \quad (\text{A.5})$$

We obtain the form of the interfacial and strain energy used in Section 3.2.

Appendix B

Notational conventions

B.1 Basics

The set of natural numbers is denoted by \mathbb{N} , the set of real numbers by \mathbb{R} . The characteristic function of a set E is χ_E . The open ball around a point x with radius ρ is called $B(x, \rho)$. The distance function of a point to a set is denoted by $\text{dist}(x, E)$, which is defined as $\inf_{y \in E} d(x, y)$, where $d(\cdot, \cdot)$ is the underlying metric of the space; in our case this is always the Euclidean metric. In the sense of sets of finite perimeter we work with equivalence classes of sets, such that, for a set E within the domain $\Omega \subset \mathbb{R}^n$, we have $E = \{x \in \Omega \text{ such that } \rho^{-n} \text{m}(E \cap B(x, \rho)) > 0 \text{ for all } \rho > 0\}$. This ensures that the distance term is always well defined.

B.2 Functional analysis

If a function is called “integrable” it is assumed to be Lebesgue-integrable; the Lebesgue-measure of a set A is denoted by $\text{m}(A)$. The average integral of a function f is denoted by $\int_A f(x) dx = \frac{1}{\text{m}(A)} \int f(x) dx$. Sobolev spaces are denoted, as usual, by $W^{k,p}$, and the Hilbert space $H^k = W^{k,2}$. The dual space of a Banach space B is B' . Except for spaces for functions after Fourier transforms, these are assumed to be real function spaces. In the case of a Hilbert space, the scalar product of two vectors f and g is denoted by (f, g) , or, in the case of finite dimensional vector spaces, by $f \cdot g$. The Fourier transform of a function f is denoted by \hat{f} .

Partial derivatives of functions are often denoted by subscripts, i.e., $f_{x_1} = \frac{\partial f}{\partial x_1}$. For a one-dimensional function f , its derivative is denoted by f' .

We use the common notation $f_i \rightarrow f$ for strong convergence and $f_i \rightharpoonup f$ for weak convergence. Weak-star convergence is denoted by $f_i \overset{*}{\rightharpoonup} f$. The relevant vector space for the convergence is given in the text.

B.3 Elasticity

We commonly work on a crystallographic reference configuration $\Omega \subset \mathbb{R}^n$, where $n \in \{2, 3\}$. This reference configuration is mapped to a deformed, or current, configuration by the deformation y . In the full elasticity case, $y(x) \in \mathbb{R}^n$, for anti-plane shear we have $y(x) \in \mathbb{R}$. In full elasticity, the displacement u is given as $u = y - \text{Id}$, i.e., the difference between y and the identity mapping. In anti-plane shear, y and u are identical. The deformation gradient is ∇y . For an elastic energy density $W(\nabla y)$, the stress tensor is given as $\sigma_{ij} = \frac{\partial W(\nabla y)}{\partial (\nabla y)_{ij}}$. Sometimes these quantities are written in terms of the displacement gradient ∇u , which differs from the deformation gradient only by an identity matrix (again, in anti-plane shear, they are identical). The commonly seen divergence of the stress tensor, $\text{div } \sigma$, is assumed to be taken row-wise in the full elasticity case.

In the sharp interface models, we have $\Omega = E \cup (\Omega \setminus E) \cup \Gamma$. The phase boundary $\Gamma = \partial E \setminus \partial \Omega$ separates the two phases occupied by E and its complement. Given a quantity f , continuous on E and $\Omega \setminus E$, we denote its jump across the phase boundary, for a point $x \in \Gamma$, by $\llbracket f \rrbracket(x) = \lim_{\substack{y \rightarrow x \\ y \in E}} f(y) - \lim_{\substack{z \rightarrow x \\ z \in \Omega \setminus E}} f(z)$. The average of the same quantity on the phase boundary is given by $\langle f \rangle(x) = \frac{1}{2} \left(\lim_{\substack{y \rightarrow x \\ y \in E}} f(y) + \lim_{\substack{z \rightarrow x \\ z \in \Omega \setminus E}} f(z) \right)$.

Bibliography

- [1] R. Abeyaratne, C. Chu, and R. D. James. Kinetics of materials with wiggly energies: Theory and application to the evolution of twinning microstructures in a Cu-Al-Ni shape memory alloy. *Phil. Mag. A*, 73(2):457–498, 1996.
- [2] R. Abeyaratne and J. K. Knowles. On the driving traction acting on a surface of strain discontinuity in a continuum. *J. Mech. Phys. Solids*, 38(3):345–360, 1990.
- [3] R. Abeyaratne and J. K. Knowles. Implications of viscosity and strain-gradient effects for the kinetics of propagating phase boundaries in solids. *SIAM J. Appl. Math.*, 51(5):1205–1221, 1991.
- [4] R. Abeyaratne and J. K. Knowles. Kinetic relations and the propagation of phase boundaries in solids. *Arch. Rational Mech. Anal.*, 114(2):119–154, 1991.
- [5] R. Abeyaratne and J. K. Knowles. *Evolution of Phase Transitions: A Continuum Theory*. Cambridge University Press, 2006.
- [6] M. Achenbach and I. Müller. Creep and yield in martensitic transformations. *Ingenieur-Archiv*, 53(2):73–83, 1983.
- [7] M. Achenbach and I. Müller. Simulation of material behaviour of alloys with shape memory. *Archives of Mechanics*, 37(6):573–585, 1985.
- [8] F. Almgren, J. E. Taylor, and L. Wang. Curvature-driven flows: a variational approach. *SIAM J. Control Optim.*, 31(2):387–438, 1993.
- [9] L. Ambrosio, N. Fusco, and D. Pallara. *Functions of bounded variation and free discontinuity problems*. Oxford Mathematical Monographs. Oxford University Press, 2000.
- [10] L. Ambrosio, N. Gigli, and G. Savaré. *Gradient flows in metric spaces and in the space of probability measures*. Lectures in Mathematics ETH Zürich. Birkhäuser Verlag, 2005.
- [11] J. M. Ball and R. D. James. Fine phase mixtures as minimizers of energy. *Arch. Rational Mech. Anal.*, 100(1):13–52, 1987.

- [12] P. Bélik and M. Luskin. A computational model for the indentation and phase transformation of a martensitic thin film. *J. Mech. Phys. Solids*, 50(9):1789–1815, 2002.
- [13] K. Bhattacharya. Phase boundary propagation in a heterogeneous body. *R. Soc. Lond. Proc. Ser. A Math. Phys. Eng. Sci.*, 455(1982):757–766, 1999.
- [14] K. Bhattacharya. *Microstructure of Martensite: Why It Forms and How It Gives Rise to the Shape-Memory Effect*. Oxford University Press, 2003.
- [15] K. Bhattacharya and R. D. James. A theory of thin films of martensitic materials with applications to microactuators. *J. Mech. Phys. Solids*, 47(3):531–576, 1999.
- [16] K. Bhattacharya, R. D. James, and P. J. Swart. Relaxation in shape-memory alloys. i. mechanical model. *Acta Materialia*, 45(11):4547–4560, 1997.
- [17] H. Biermann, A. Levin, and D. Zorin. Piecewise Smooth Subdivision Surfaces with Normal Control. In Kurt Akeley, editor, *Siggraph 2000, Computer Graphics Proceedings*, pages 113–120. Addison Wesley Longman, 2000.
- [18] H. Brezis. *Analyse fonctionnelle*. Collection Mathématiques Appliquées pour la Maîtrise. Masson, 1983.
- [19] N. Bubner, J. Sokołowski, and J. Sprekels. Optimal boundary control problems for shape memory alloys under state constraints for stress and temperature. *Numer. Funct. Anal. Optim.*, 19(5-6):489–498, 1998.
- [20] Z. Chen and K.-H. Hoffmann. On a one-dimensional nonlinear thermoviscoelastic model for structural phase transitions in shape memory alloys. *J. Differential Equations*, 112(2):325–350, 1994.
- [21] I. V. Chenchiah and S. M. Sivakumar. A two variant thermomechanical model for shape memory alloys. *Mechanics Research Communications*, 26(3):301–307, 1999.
- [22] F. Cirak and M. Ortiz. Fully C^1 -conforming subdivision elements for finite deformation thin-shell analysis. *Int. J. Numer. Meth. Engng.*, 51:813–833, 2001.
- [23] F. Cirak, M. Ortiz, and P. Schröder. Subdivision Surfaces: A New Paradigm For Thin-Shell Finite-Element Analysis. *Int. J. Numer. Meth. Engng.*, 47(12):2039–2072, 2000.
- [24] B. Craciun and K. Bhattacharya. Homogenization of a Hamilton-Jacobi equation associated with the geometric motion of an interface. *Proc. Roy. Soc. Edinburgh Sect. A*, 133(4):773–805, 2003.

- [25] B. Craciun and K. Bhattacharya. Effective motion of a curvature-sensitive interface through a heterogeneous medium. *Interfaces Free Bound.*, 6(2):151–173, 2004.
- [26] J. Cui and R. D. James. A “tent” shape thermoelastic deformation on foil of CuAlNi single crystal. Manuscript.
- [27] C. M. Dafermos. Global smooth solutions to the initial-boundary value problem for the equations of one-dimensional nonlinear thermoviscoelasticity. *SIAM J. Math. Anal.*, 13(3):397–408, 1982.
- [28] N. Dirr and N. K. Yip. Pinning and de-pinning phenomena in front propagation in heterogeneous media. *Interfaces Free Bound.*, 8(1):79–109, 2006.
- [29] P. W. Dondl. Modeling and analysis of non-diffusive phase-transitions in crystals. Master’s thesis, Technische Universität München, 2002.
- [30] P. W. Dondl and J. Zimmer. Modeling and simulation of martensitic phase transitions with a triple point. *J. Mech. Phys. Solids*, 52(9):2057–2077, 2004.
- [31] J. L. Ericksen. On correlating two theories of twinning. *Arch. Ration. Mech. Anal.*, 153(4):261–289, 2000.
- [32] L. C. Evans. *Partial differential equations*, volume 19 of *Graduate Studies in Mathematics*. American Mathematical Society, 1998.
- [33] L. C. Evans and R. F. Gariepy. *Measure theory and fine properties of functions*. Studies in Advanced Mathematics. CRC Press, 1992.
- [34] G. Fadda, L. Truskinovsky, and G. Zanzotto. Unified landau description of the tetragonal, orthorhombic, and monoclinic phases of zirconia. *Phys. Rev. B*, 66(17):174107, 2002.
- [35] F. Falk. Model free energy, mechanics, and thermodynamics of shape memory alloys. *Acta Metallurgica*, 28(12):1773–1780, 1980.
- [36] H. Funakubo, editor. *Shape Memory Alloys (Precision Machinery and Robotics, Vol 1)*. CRC Press, 1987.
- [37] A. Garroni and S. Müller. Γ -limit of a phase-field model of dislocations. *SIAM J. Math. Anal.*, 36(6):1943–1964 (electronic), 2005.
- [38] E. Grinspun. *The Basis Refinement Method*. PhD thesis, California Institute of Technology, 2003.
- [39] E. Grinspun, P. Schröder, and P. Krysl. Natural Hierarchical Refinement for Finite Element Methods. *International Journal for Numerical Methods in Engineering*, 56(8):1109–1124, 2003.

- [40] M. E. Gurtin. *Thermomechanics of Evolving Phase Boundaries in the Plane*. Oxford University Press, 1993.
- [41] M. E. Gurtin. *Configurational forces as basic concepts of continuum physics*, volume 137 of *Applied Mathematical Sciences*. Springer-Verlag, 2000.
- [42] K.-H. Hoffmann and A. Żochowski. Analysis of the thermoelastic model of a plate with nonlinear shape memory alloy reinforcements. *Math. Methods Appl. Sci.*, 15(9):631–645, 1992.
- [43] M. Kardar. Nonequilibrium dynamics of interfaces and lines. *arXiv:cond-mat/9704172v1 [cond-mat.stat-mech]*, 1997.
- [44] D. Kinderlehrer and P. Pedregal. Weak convergence of integrands and the Young measure representation. *SIAM J. Math. Anal.*, 23(1):1–19, 1992.
- [45] P. Klouček. The computational modeling of nonequilibrium thermodynamics of the martensitic transformations. *Comput. Mech.*, 22(3):239–254, 1998.
- [46] P. Klouček and M. Luskin. The computation of the dynamics of the martensitic transformation. *Contin. Mech. Thermodyn.*, 6(3):209–240, 1994.
- [47] P. Klouček and M. Luskin. Computational modeling of the martensitic transformation with surface energy. *Math. Comput. Modelling*, 20(10-11):101–121, 1994.
- [48] R. V. Kohn. The relaxation of a double-well energy. *Contin. Mech. Thermodyn.*, 3(3):193–236, 1991.
- [49] M. Kosłowski, A. M. Cuitiño, and M. Ortiz. A phase-field theory of dislocation dynamics, strain hardening and hysteresis in ductile single crystals. *J. Mech. Phys. Solids*, 50(12):2597–2635, 2002.
- [50] P. Krulevitch, A. P. Lee, P. B. Ramsey, J. C. Trevino, J. Hamilton, and M. A. Northrup. Thin film shape memory alloy microactuators. *J MEMS*, 5(4):270–282, Dec 1996.
- [51] M. Kružík, A. Mielke, and T. Roubíček. Modelling of microstructure and its evolution in shape-memory-alloy single-crystals, in particular in CuAlNi. *Meccanica*, 40(4-6):389–418, 2005.
- [52] C. Loop. *Generalized B-spline surfaces of arbitrary topological type*. PhD thesis, University of Washington, 1992.
- [53] S. Luckhaus and T. Sturzenhecker. Implicit time discretization for the mean curvature flow equation. *Calc. Var. Partial Differential Equations*, 3(2):253–271, 1995.

- [54] M. Luskin. Computational modeling of microstructure. In *Proceedings of the International Congress of Mathematicians, Vol. III (Beijing, 2002)*, pages 707–716, Beijing, 2002. Higher Ed. Press.
- [55] A. Mielke. Evolution of rate-independent systems. In *Evolutionary equations. Vol. II*, Handb. Differ. Equ., pages 461–559. Elsevier/North-Holland, Amsterdam, 2005.
- [56] S. Müller. Variational models for microstructure and phase transitions. In *Calculus of variations and geometric evolution problems (Cetraro, 1996)*, volume 1713 of *Lecture Notes in Math.*, pages 85–210. Springer, 1999.
- [57] O. Narayan and D. S. Fisher. Threshold critical dynamics of driven interfaces in random media. *Phys. Rev. B*, 48(10):7030–7042, Sep 1993.
- [58] T. Nattermann, S. Stepanow, L.-H. Tang, and H. Leschorn. Dynamics of interface depinning in a disordered medium. *J. Phys. II France*, 2:1483–1488, 1992.
- [59] J. Ortin. Preisach modeling of hysteresis for a pseudoelastic Cu-Zn-Al single crystal. *Journal of Applied Physics*, 71(3):1454–1461, 1992.
- [60] K. Otsuka and C. M. Wayman, editors. *Shape Memory Materials*. Cambridge University Press, 2002.
- [61] I. Pawłowski and A. Żochowski. Nonlinear thermoelastic system with viscosity and nonlocality. In *Free boundary problems: theory and applications, I (Chiba, 1999)*, volume 13 of *GAKUTO Internat. Ser. Math. Sci. Appl.*, pages 251–265. Gakkōtoshō, Tokyo, 2000.
- [62] J. L. Pelegrina, M. Rodriguez de Rivera, V. Torra, and F. C. Lovey. Hysteresis in Cu-Zn-Al SMA: From high resolution studies to the time dependent modeling and simulation. *Acta Metallurgica et Materialia*, 43(3):993–999, 1995.
- [63] P. Purohit and K. Bhattacharya. Dynamics of strings made of phase-transforming materials. *J. Mech. Phys. Solids*, 51:393–424, 2003.
- [64] A. C. E. Reid and R. J. Gooding. Pattern Formation in a 2D Elastic Solid. *Physica A*, 239:1–10, 1997.
- [65] M. O. Rieger and J. Zimmer. Global existence for nonconvex thermoelasticity. *Adv. Math. Sci. Appl.*, 15(2):559–569, 2005.
- [66] P. Rosakis. Compact zones of shear transformation in an anisotropic solid. *J. Mech. Phys. Solids*, 40(6):1163–1195, 1992.

- [67] T. Roubíček. Dissipative evolution of microstructure in shape memory alloys. In Hans-Joachim Bungartz, Ronald H. W. Hoppe, and Zenger Christoph, editors, *Lectures on applied mathematics (Munich, 1999)*, pages 45–63. Springer, 1999.
- [68] A. Sadjadpour and K. Bhattacharya. A micromechanics inspired constitutive model for shape-memory alloys. *Smart Mater. Struct.*, 16(1):S51–S62, 2007.
- [69] J. Sprekels and S. M. Zheng. Global solutions to the equations of a Ginzburg-Landau theory for structural phase transitions in shape memory alloys. *Phys. D*, 39(1):59–76, 1989.
- [70] J. Stam. Evaluation of Loop Subdivision Surfaces. In *SIGGRAPH 1999 Course Notes CD-ROM*. ACM SIGGRAPH, 1999.
- [71] P. J. Swart and P. J. Holmes. Energy minimization and the formation of microstructure in dynamic anti-plane shear. *Arch. Rational Mech. Anal.*, 121(1):37–85, 1992.
- [72] L. Truskinovsky and G. Zanzotto. Elastic crystals with a triple point. *J. Mech. Phys. Solids*, 50(2):189–215, 2002.
- [73] J. Zimmer. *Mathematische Modellierung und Analyse von Formgedächtnislegierungen in mehreren Raumdimensionen*. PhD thesis, Technische Universität München, 2000.
- [74] J. Zimmer. Global existence for a nonlinear system in thermoviscoelasticity with nonconvex energy. *J. Math. Anal. Appl.*, 292(2):589–604, 2004.
- [75] J. Zimmer. Stored energy functions for phase transitions in crystals. *Arch. Ration. Mech. Anal.*, 172(2):191–212, 2004.
- [76] D. Zorin and P. Schröder, editors. *Subdivision for Modeling and Animation*. SIGGRAPH 1999 Course Notes CD-ROM, ACM SIGGRAPH, 1999.